TECHNISCHE UNIVERSITÄT MÜNCHEN

TUM School of Engineering and Design

Modeling and Simulation of Flexible Protective Structures by Coupling Particle and Finite Element Methods

Klaus Bernd Sautter

Vollständiger Abdruck der von der TUM School of Engineering and Design der Technischen Universität München zur Erlangung des akademischen Grades eines

Doktor der Ingenieurwissenschaften

genehmigten Dissertation.

Vorsitzende:

Priv.-Doz. Dr.-Ing. habil. Stefan Kollmannsberger

Prof. Dr.-Ing. Martin Mensinger

Prüfer der Dissertation:

1. Prof. Dr.-Ing. Kai-Uwe Bletzinger
2. Prof. Dr.-Ing. habil. Roland Wüchner
3. Prof. Dr.-Ing. habil. Fabian Duddeck

Die Dissertation wurde am 17.03.2022 bei der Technischen Universität München eingereicht und durch die TUM School of Engineering and Design am 23.10.2022 angenommen.

Schriftenreihe des Lehrstuhls für Statik
TU München

Band 54

Klaus Bernd Sautter

Modeling and Simulation of flexible protective structures by coupling Particle and Finite Element Methods

München 2022

Veröffentlicht durch

Kai-Uwe Bletzinger
Lehrstuhl für Statik
Technische Universität München
Arcisstr. 21
80333 München

Telefon: +49(0)89 289 22422
Telefax: +49(0)89 289 22421
E-Mail: kub@tum.de
Internet: www.bgu.tum.de/st/startseite/

ISBN: 978-3-943683-68-4

für meine Eltern

Kurzfassung

Gravitationsgetriebene Naturgefahren wie Steinschlag, Murenabgänge und Lawinen stellen eine ernst zu nehmende Gefahr dar und werden mit der aktuellen Entwicklung der Erderwärmung immer häufiger. Da sich diese Ereignisse oft nicht verhindern lassen, werden speziell entwickelte Schutzstrukturen an exponierten Stellen aufgebaut, um vor allem Infrastruktur und besiedelte Gebiete zu schützen. Durch die Komplexität dieser Naturgefahren und ihrer ausgeprägten Wechselwirkung mit den Schutzstrukturen sind vereinfachte Lastansätze oft nicht anwendbar. Um die Analyse der Auswirkung des Einschlags auf Schutzstrukturen zu ermöglichen, stellt diese Arbeit eine modulare, partitionierte Simulationsumgebung vor. Diese erlaubt die Kopplung verschiedener numerischer Methoden, indem sie eine passende und effiziente Schnittstelle bereitstellt. Dabei wird das Hauptaugenmerk auf die Simulation des Einschlags von Steinen in flexible Schutzstrukturen gelegt. Die Steine werden mittels der Diskrete-Elemente-Methode modelliert und simuliert. Anschließend kommt die Finite-Elemente-Methode zur Anwendung, um die passende Strukturantwort auf die Aufpralllasten zu berechnen.

Flexible Schutzstrukturen sind so konstruiert, dass sie große Verformungen erlauben. Dadurch entsteht ein langer Bremsweg, der die Dissipation großer Energien ermöglicht. Aus diesem Grund finden sich viele verschiedene und komplexe Komponenten in der Schutzstruktur wieder. Daraus ergeben sich besondere Herausforderungen an die Modellierung mittels der Finiten Elemente Methode. Um reale Szenarien zu simulieren, wird in dieser Arbeit die effiziente Modellierung von Strukturelementen, einschlagenden Objekten und die Integration von Geländedaten ausführlich diskutiert.

Als methodischer Kernpunkt dieser Arbeit dient die partitionierte Kopplung verschiedener Methoden. Das Hauptaugenmerk liegt hierbei auf der Kopplung der Diskrete-Elemente-Methode mit der Finite-Elemente-Methode und ist so modular entwickelt, dass beliebige Methoden zusammengebracht werden können. Exemplarisch wird das mit der Partikel Finite Elemente Methode und der Materialpunktmethode demonstriert. Für den generischen Einsatz beschreibt diese Arbeit verschiedene Kopplungsalgorithmen, vergleicht sie und erläutert den Implementierungsprozess. Dabei werden eine schwache Kopplung und eine starke Kopplung mittels Gauss-Seidel in Kombination mit einer Aitken Methode präsentiert.

Mit der Berechnung mehrerer großer Steinschlagschutzsysteme schließt diese Arbeit und zeigt durch die Validierung anhand von Feldversuchen in den Schweizer Bergen und Kanada ihr Potenzial. So erlaubt die modulare Kopplungsumgebung eine effiziente Analyse von Steineinschlägen in flexible Schutzstrukturen. Schlussendlich werden weitere Anwendungsmöglichkeiten mit verschiedenen Komplexitäten präsentiert, um die generische Einsetzbarkeit auf andere Gebiete der Impaktsimulationen aufzuzeigen.

Abstract

Gravity-driven natural hazards, such as rockfalls, debris flow, and avalanches, represent a severe danger and are becoming more frequent with the current development of global warming. Since these events often cannot be prevented, specially designed protective structures are being built in exposed locations, primarily to protect infrastructure and populated areas. Due to the complexity of these natural hazards and their pronounced interaction with protective structures, simplified load approaches are often not applicable. To enable the analysis of the impact on protective structures, this work presents a modular, partitioned simulation environment. It allows the coupling of different numerical methods by providing a suitable and efficient interface. The main focus is on the simulation of the impact of rocks on flexible protective structures. First, the rocks are modeled and simulated using the discrete element method. The finite element method is then applied to calculate the appropriate structural response to the impact loads.

Flexible protective structures are designed to allow large deformations. This results in a long braking distance, which allows for the dissipation of large energies. For this reason, many different and complex components are found in the protective structure, leading to particular challenges for modeling using the finite element method. In order to simulate real scenarios, the efficient modeling of structural elements, impacting objects, and the integration of terrain data is discussed in detail in this dissertation.

The partitioned coupling of different methods serves as the methodological core of this work. The main focus lies on the coupling of the discrete element method with the finite element method and is developed in such a modular way that arbitrary methods can be brought together. This is exemplified by the particle finite element method and the material point method. The dissertation describes different coupling algorithms, compares them, and explains the implementation process for generic use. Weak coupling and strong coupling using Gauss-Seidel in combination with an Aitken method are presented.

The computation of several large rockfall protection systems concludes this work and demonstrates its potential through validation using field tests in the Swiss and Canadian mountains. Thus, the modular coupling environment allows efficient rockfall analysis in flexible protection structures. Finally, further application possibilities with different complexities are presented to show the generic applicability to other fields of impact simulations.

Acknowledgements

I am very grateful for the support I have received from many sides over the past years, without which this work would not have been possible.
I would like to thank Prof. Dr.-Ing. Kai-Uwe Bletzinger not only for the many helpful technical comments and discussions but also for the opportunity to pursue my research at the Chair of Structural Analysis. He has created a learning and working environment that allows all employees to successfully pursue their respective interests together in peace. The always open door and the corresponding open ears of Prof. Dr.-Ing. habil. Roland Wüchner have kept me on the right track and sometimes pulled me back up when the goal once again seemed too distant and unattainable. The collaborations he initiated and his commitment to the staff were essential for the success of this work, and I am very grateful for that.
I would also like to thank all my colleagues at the chair for their excellent cooperation over the past years. The working atmosphere has motivated me every day and ensured that I have almost regarded the chair as my second home. Although the entire team is responsible for this atmosphere, I would like to highlight a few. My special thanks go to Dr.-Ing. Winterstein, who got me involved in the department during my Master's studies and has always been a mentor to me. Philipp Bucher also deserves a big thank you. His programming skills, interesting thought processes, and tireless helpfulness provided the impetus for this work and kept it on the right track. Inseparably, I would like to mention Tobias Teschemacher. He was always eager to help and sacrificed a lot of his time for his colleagues.
I would also like to thank my teaching assistant colleagues Veronika Singer, Dr.-Ing. Ann-Kathrin Goldbach, and Martin Fußeder for their great cooperation. Furthermore, I would like to mention Máté Péntek, Manuel Messmer, Shahrokh Shayegan, and Ihar Antanou, who made my time at the department very pleasant. Thanks also go to Peter Wilson in Australia, who was a good friend, helpful learning partner, and always a role model for me.
However, the cooperation was not only limited internally to TUM. I have received a lot of support from Geobrugg in Switzerland. This cooperation was incredibly fruitful, and I am glad that it continued through the Master's thesis to the end of my doctorate. Three people, in particular, deserve special mention here: Nadine Feiger, Helene Lanter, and Dr.-Ing. Corinna Wendeler. They supported me tirelessly in both the theoretical part of this thesis and the practical part, co-wrote and proofread papers, and always had an open ear. Many thanks for that.
Finally, I would like to thank my family and partner for their support along the way. I owe a lot of my strength and motivation to them.

Klaus Bernd Sautter
Technical University of Munich
March 2022

Contents

Abbreviations

BVP	Boundary Value Problem
CAD	Computer-Aided Design
COR	Coefficient of Restitution
CPU	Central Processing Unit
CTI	Swiss Federal Commission for Innovation and Technology
DEM	Discrete Element Method
FE	Finite Element
FEM	Finite Element Method
FSI	Fluid-Structure Interaction
H.O.T.	Higher Order Terms
HM+D	Hertz Mindlin Spring Dashpot Model
IBVP	Initial Boundary Value Problem
LS+D	Linear Spring Dashpot Model
MPC	Multi Point Constraint
MPM	Material Point Method
PFEM	Particle Finite Element Method
PLS(B)	Plastic Dissipation Model
SAEFL	Swiss Agency for Environment, Forests and Landscape
SPH	Smoothed-Particle Hydrodynamics
TF	Tension-Field

CHAPTER 1

Introduction

Gravity-driven natural hazards such as rockfall, avalanches, or mudflows pose an extreme danger to people and infrastructure. The current developments in global warming are leading to increasingly frequent natural disasters. This trend can also be observed in the number of scientific publications. Figure 1.1* shows the number of publications since 1975 that deal with the keyword "natural hazard".

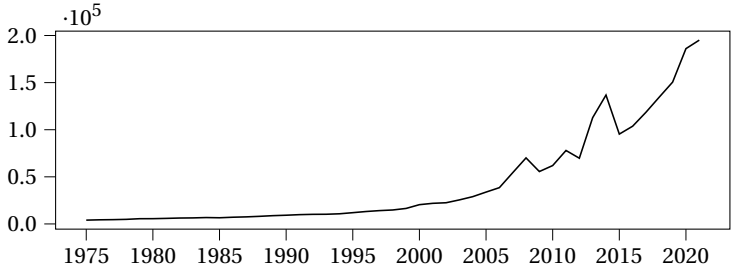

Figure 1.1: Increasing number of scientific publications over time containing the keyword "natural hazard".

Especially in mountainous areas settlements and roads have to be protected. If no preventive measures can be taken, suitable protective structures must be installed. Due to the high energies that gravity-driven natural hazards usually bring, flexible protection structures are preferred over rigid structures. Flexibility is achieved using nets and cables, which allows large deformations of the protective structure. As a result, impacting objects experience a longer braking distance, resulting in slower braking accelerations. Like other extreme load cases such as wind [129, 131], avalanches [76, 77], and mudflows [125, 127], where load cause and structural response are in strong interaction, simple load approaches are typically not sufficient or work only for limited applications [134]. To support

* The data is obtained from https://app.dimensions.ai/

the engineer in the design process, a combination of experiments and numerical simulations is recommended. Simulations do not claim to replace experiments entirely but should be used as an additional tool to support the design process and supplement costly and complex experiments. They show their strength, especially in the preliminary design and the investigation of construction details. Changes such as cable positions and different mesh types can be investigated efficiently without performing new tests for each change. The experiments should be equal partners besides the simulations and serve the final validation of designs. Furthermore, in the course of this work, it will be found that material parameters of the simulation often have to be tuned with the help of experimental data. For this purpose, this dissertation develops a suitable simulation environment to analyze the interaction of protective structures and impacting objects numerically.

With [90, 91] the first investigations of numerical rockfall simulations can be found. It is learned that underwater anti-submarine nets inspired the design idea of the protective nets. They deal with experiments and first steps towards a numerical tool for analyzing rockfalls. [90, 91]'s work is performed in the software `ECRANS`. Shortly after that, [56]'s work is developed, whereby the numerical modeling of unique ring elements is advanced. Further experiments also take place, leading to the calibration of simulation results. In [56, 124] the foundation for the simulation software `FARO` is laid and eventually further developed. Thus, one of the first well-functioning numerical tools for the analysis of rockfalls is created with `FARO`. It uses the Finite Element Method (FEM) [122] to model the structure while the impacting object is thereby modeled as a perfect sphere with an elastic boundary layer for realistic load transfer. There are also references to modeling arbitrarily shaped, non-spherical objects, but this idea is not explored further and is not implemented either. Many publications in this field, such as [20, 43, 83, 116, 117] are produced based on the `ABAQUS` software from this time on. Some of them [43] develop new element formulations in `ABAQUS` and drive its popularity. The development of new simulation tools does not diminish, and programs that rely entirely on the Discrete Element Method (DEM) [32] emerge as a result. The impacting objects are modeled as discrete particles, while the protective structure itself is composed of many small particles, which exchange specific forces among themselves and thus act like springs. Following this, `PFC` from [10] and `GENEROCK` from [30] are worth mentioning. Moreover, the `YADE` [70, 113] software is frequently used and keeps appearing in recent publications, such as [39, 95]. It also uses pure DEM to model the impacting objects and the protection structures [14, 42].
Building on the developments of [56, 124], many publications deal with the simulation and modeling of rockfall protection systems. [43] develops the so-called chain-link element, which allows a high-resolution modeling of the nets and their internal contact nodes. [125] takes up this element formulation to simulate mudflow protection nets via FSI and thus builds on the work of [127]. However, the question arises whether the detailed modeling of all possible motion freedoms of the meshes makes sense. The exact modeling often results in overhead, especially if the global structural behavior is of interest. To reduce the complexity of structural modeling, [117] introduces a hybrid modeling approach. Here, the interesting and exposed locations in the Finite Element (FE) mesh are mod-

eled at high resolution, while edge regions are modeled coarsely. Works such as [37, 83, 100] also address the issue of appropriate structural modeling and use shells and isotropic plate models. [20, 58] deal in detail with the so-called "bullet effect". In this context, analytical equations are derived based on energy terms to analyze the perforation of protective nets. This is accompanied by numerical simulation in ABAQUS, where the rocks are modeled as polyhedra and the chain-link elements of [43] are used.

In order to extend the previous work and introduce a new, efficient approach to analyze the interaction of impacting objects and flexible protective structures, this work presents the partitioned coupling of different numerical methods. It brings together different numerical methods by partitioning the actual physics. This results in the advantage that all simulation participants can be investigated and implemented separately. Furthermore, the coupling method is formulated generically so that different methods can be combined. In extreme cases, even without direct access to the individual computer codes. This is called the coupling of black box codes. Usually, black box coupling is not advisable because detailed knowledge about all simulation participants is desired. Therefore, no black box solvers are used in this work, and detailed investigation and further development in all simulation parts are performed. Although the presented coupling algorithm is kept generic to bring together different numerical methods, this work focuses on the coupling of DEM and FEM to simulate the impact of rocks into flexible protective structures.
Besides the advantages of the individual treatment of the simulation participants, the division of the physics creates challenges. It results in the additional task of treating the common interface correctly. For this purpose, this dissertation explains the appropriate interface equations and presents various coupling algorithms. As described in [45], there are several ways to simulate partitioned systems. Many publications, such as [73, 74, 129, 130, 131] already deal with this topic in Fluid-Structure Interaction (FSI). Furthermore, a distinction is made between weak and strong coupling algorithms, with higher complexities in each case. While for many cases, the weak coupling is sufficient, which exchanges data once and subsequently advances in time, strong coupling methods have to be used if the data like initial velocities or masses of the simulation participants differ strongly from each other. Additionally, the time step size also plays a crucial role. In the course of this work, the ideas of the mentioned publications are taken up, and a Dirichlet-Neumann [110] coupling algorithm is designed, which allows the strong coupling for the case of DEM-FEM. It employs a fixed-point iteration in conjunction with an Aitken relaxation [1]. The effects of these two weak and strong coupling algorithms on various smaller systems are eventually investigated to simulate real protective structures. Finally, further validations and benchmark tests are calculated to test the presented coupling algorithms.
Further developments not only take place on the global coupling level but also relate to the individual components. Thus, in contrast to [124], this work does not only use spherical modeling of the impacting objects, but clusters [68] of discrete spheres. This feature allows the approximation of arbitrarily shaped rocks. Especially for rockfalls with high rotational velocities and non-regular shapes, the use of perfect spherical shapes quickly reaches its limits. The advantage over polyhedral geometries, where the impacting object is discretized with sur-

face elements, is shown in more effective and inexpensive contact algorithms [80, 112] and is discussed in detail throughout this dissertation. Moreover, it differs from developments such as [10] with PFC and [30] with GENEROCK in that not the same method (DEM) is used to model the rocks and the structure. The coupling method of this work allows using the best suitable methods for the respective simulation participants. As a result, the DEM and the FEM can be efficiently brought together. While the structure modeling through the FEM represents a clear advantage, the use of DEM for modeling the structure can be found among others also in [9, 40, 119].
New approaches are also provided in the field of FEM. It is used to calculate the appropriate structural response to the DEM contact forces by efficiently solving dynamic structural problems. Various element formulations and material laws suitably represent the complex constructions of flexible protection structures in a numerical model. The formulations of particular interest are described in detail in this dissertation, and alternative modeling options are discussed. Plastic, hyper-elastic, and elastic material laws are used, and unique element formulations can represent, among others, sliding cable nodes [13] and wrinkling surface structures [86]. Since the structure is resolved globally, micro-level formulations are deliberately avoided. For this reason, strain-rate dependent material laws are not used, which would instead find their application in the impact on rigid structures. Geometrically non-linear finite element formulations are used to simulate the large deformations of the flexible protection structures.

In order to subject the coupling method to the final test, field experiments of large rockfall protection structures are simulated towards the end of the thesis. Close cooperation with the Swiss company Geobrugg has led to the analysis of several experiments. Therefore, based on these data, various studies on the appropriate modeling of the impacting objects and the structure can be performed. Different real protective structures are simulated, and good agreements with the experimental results are found. The agreement of the simulation with the experiments inspires confidence in the presented coupling methodology.

Conducive to a complete simulation environment, the inclusion of terrain data into the numerical model is also discussed. Considering the surrounding terrain, its influence can be included in the simulation. This opens up a wide range of new application possibilities. For example, possible impact positions and impact velocities can be determined in this way. Furthermore, the inclusion of terrain data allows an optimization of the position of the protective structure and the calculation of possible worst-case scenarios.

The implementation of the presented coupling methodology and all required components is performed in the open-source multi-physics software Kratos [33, 34, 47]. It is mainly written in C++ [115] and provides a Python [72] interface. Thus, regarding the aforementioned earlier code developments, this work joins a long line of innovative developments in the field of numerical simulations of rockfalls.

Listing of the chapter contents

For better orientation within this work, the content is structured in bullet points below.

Chapter 2 introduces the flexible protection structures that are the subject of this thesis.

Chapter 3 gives a detailed discussion about the background theory of the applied methods.

- Section 3.1 discusses the structural mechanics fundamentals.
- Section 3.2 introduces the necessary FEM equations and discusses all applied element formulations and material laws.
- Section 3.3 gives an introduction on the DEM solution procedure and discusses important aspects of the method.

Chapter 4 describes the partitioned coupling scheme. It discusses the interface equations, efficient data handling and transfer, and coupling algorithms. Various validation cases and benchmark tests follow to test the coupling and show its performance.

Chapter 5 presents two different real-scale experiments and shows the application of the proposed coupling scheme. This chapter also includes a discussion of the appropriate modeling of both the impacting object and the structure itself.

Chapter 6 then discusses the inclusion of terrain data in the coupled simulation and points out its advantages and possible application cases.

Chapter 7 shows the possibility to apply the results of this work to other applications. The car wheel impact on a racetrack protection net and a human head impact on an inflated cushion introduce new application cases for the DEM-FEM coupling. Additionally, two other particle methods are employed in a coupled simulation to show the generic application of the herein demonstrated coupling method.

Chapter 8 introduces the software environment and clarifies which developments have arisen as a direct result of this dissertation.

Chapter 9 concludes by summarizing this work and identifies further potential areas of research.

CHAPTER 2

Flexible Protection Structures

Flexible protective structures represent exceptional designs. Every detail is designed to allow as much deformation as possible and to absorb the maximum energy. Unlike rigid structures, such as concrete walls, this creates challenges not only for the actual construction but also for creating an adequate FE model. The unique designs and modes of action of flexible protective structures are discussed below to lay the foundation for later discussions concerning numerical models.

Especially in mountainous areas, rockfalls, debris flows, and avalanches repeatedly cause the destruction of infrastructure and heavily populated areas [41, 64, 109, 126, 135]. Since these events often cannot be prevented, protective structures are installed at exposed locations. There are many different types of protection structures against natural disasters. Flexible nets, as shown in Figures 2.1 and 2.2a, are used to allow large deformations and thus extend the braking distance. The extended braking distance reduces braking acceleration and allows for a smooth load transfer which reduces peak loads and maximum stresses. In the case of rigid barriers, much higher maximum transient loads occur because almost

Figure 2.1: Ring net with debris.

no deformation of the structure can take place, and thereby the impacting medium

(rocks, avalanches, mudflows) is abruptly decelerated. Rigid protection structures as shown in Figure 2.2b are therefore rather rarely employed.

(a) Flexible mud flow barrier in Switzerland.

(b) Rigid mud flow barrier in Switzerland.

Figure 2.2: Comparison of a flexible and a rigid mud flow barrier in Switzerland. The flexible structure has been added approximately 200m downstream of the rigid barrier.

Flexible protective structures can be further divided into two subcategories. A distinction is made between active and passive measures. Figure 2.3 demonstrates the two main categories of flexible protection structures:

- Active measures are actively preventing rock detachment. A well known example is the near-surface net construction in Figure 2.3a. The calculation of active measures is not part of this dissertation since it is a quasi-static load for which equivalent load models can be developed. The challenge is to determine the exact endangered areas in order to protect them appropriately.
- Passive measures do not prevent the rockfall but protect vulnerable areas, such as infrastructure and populated areas, from its action. They can be further classified in self-cleaning and non-self-cleaning [103]. See Figure 2.3c and Figure 2.3b, respectively.

The construction types in Figures 2.3c, 2.3d are called Attenuator barriers and can be assigned to passive measures. A numerical simulation follows in section 5.2.1. Instead of catching and arresting the impacting rock, they act as a curtain and guide it to a safe zone. The safe zone can subsequently be easily cleaned, and the construction normally does not need to be replaced after impact. Attenuator barriers have been employed for several decades [100] and have been extensively tested in the field [3, 52, 60, 132].
In general, maximizing the braking distance and maximizing the energy that can be absorbed, is the goal of the designs. Various elements found in the design of

(a) Banya railway rockfall protection, active.

(b) Monserrate walking path, passive.

(c) Kaikoura State Highway, passive.

(d) Attenuator experiment after impact. Photograph of the experiment discussed in section 5.2.1.

Figure 2.3: Comparison of active and passive rockfall protection, adapted from [103]. All photographs are property of Geobrugg (https://www.geobrugg.com).

the flexible protective structures help absorb as much energy as possible. Concerning the FE modeling of the protective structures, it is convenient to discuss each element.

Cable Net

The core of the flexible protection structures is the net itself. As can be seen in Figure 2.3, it usually consists of rings that are connected or a mesh fence-like net. These are often combined, as in Figure 2.3b, to create a primary structure and a secondary net that retains smaller debris. This type of design takes advantage of the properties of the steel wires within these nets while saving material. [90, 91] mention that these rings were originally used in underwater anti-submarine structures. The appropriate FE modeling is discussed in section 3.2.7.4.

Cables and Sliding Nodes

One effective way of transferring loads is to avoid compression forces in the system. By avoiding buckling problems, smaller cross-sectional areas can be selected. Flexible protective structures primarily use cables to tie the structure to the rock. The construction of cables allows an increased equivalent Young's Modulus and thus advantages in load transfer.

[75] expresses it appropriately: *"Cable structures such as suspension bridges, ropeways, and suspension roofs are chosen when large spans are bridged with as little material as possible. [...] In contrast to compression members, very high material strengths can be fully utilized in tension members. Since thin wires can be produced with at least four times the strength of thick sectional steel, wire cables are particularly suitable for tension members."* *

In order to allow the largest possible deformations, sliding edge cables are also installed at the edges of the protective nets. These can be seen in Figure 2.3. They run along the edges and allow the nets to slide along them, which is only restricted by friction. This detail requires increased modeling effort and is described in section 3.2.7.3.

Structural Energy Dissipation Members

The impact energy can be immense in some cases and must be efficiently removed and absorbed. Energy absorption elements play an important role in this process. They are installed between the ropes and the anchorages in the rock and absorb energy via friction and plasticity. Figure 2.4 shows two different variants of these braking elements. Solid steel cross-sections are bent when the protective structure is loaded, consuming energy in the process. In order to include these elements in the numerical simulation, a plastic material law is used and explained in section 3.2.6.4.

* Freely translated from [75] p. 4.

(a) Ring elements. (b) Metal sheets.

Figure 2.4: Photographs of the energy dissipation elements, taken in Walenstadt, Switzerland.

Anchors and Supports

Additional freedom of movement is brought into the system by suitable support conditions. Figure 2.5 shows typical connection details to the rock or, as seen here, into the ground. Clamped supports are not used, as they would create additional constraints. The support conditions in Figure 2.5 do not transmit moments, and the connecting posts can rotate freely around the support.

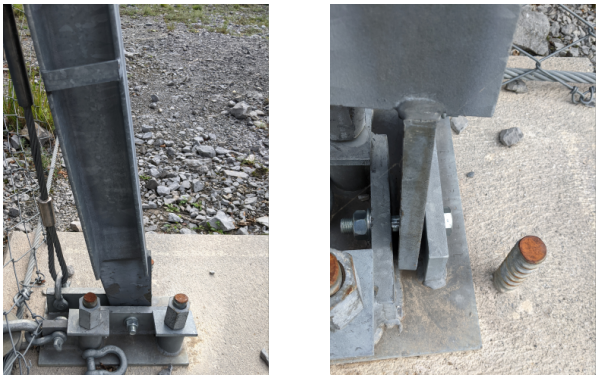

(a) Side view. (b) Front view.

Figure 2.5: The columns are not clamped at the foundation and thus do not transfer moments. As the columns are connected to the rest of the structure only at the top, truss elements are sufficient to model the respective load carrying behavior.

CHAPTER 3

Theoretical Background

In order to lay the foundations for the presented coupling methodology, the underlying theories of the FEM and the DEM are explained in this chapter. Even though the coupling methodology can be applied to different particle methods, this chapter is limited to the detailed description of the DEM, as this is the basis for the rockfall simulations. The detailed description of the FEM is preceded by a discussion of the general equations of structural mechanics. This allows the detailed explanation of the required structural elements, such as trusses, cables, beams, and surface elements. The notation will be close to the writing from [6, 61].

3.1 Structural Mechanics

The path to the strong form of the structural equilibrium is explained below to better explain the derivation of the required structure elements. In the beginning, the kinematic equations are established, which are used in the following to describe the reference geometry and the current geometry. This is followed by the derivation of the strong equilibrium form, which is derived from the momentum balance. Unfortunately, although the strong form can be found in several textbooks, the derivation, starting from the momentum balance, is often neglected.

3.1.1 Kinematics

The displacement field $\mathbf{u}$ is used to track the deformation of an arbitrary position $\mathbf{X}$ in the undeformed reference geometry. With the help of the following mapping, the position vector $\mathbf{x}$ in the current geometry can be expressed, depending on the time t.

$$\mathbf{x}(t) = \mathbf{X} + \mathbf{u}(t) . \tag{3.1}$$

It turns out to be advantageous to represent the position vectors in different bases. Especially the global Cartesian coordinate system $\mathbf{e}_i$ and the co- and contravariant bases in the current configuration $\mathbf{g}_i$, $\mathbf{g}^i$ and the reference configuration $\mathbf{G}_i$,$\mathbf{G}^i$ are attractive. Following equation 3.2, the respective base vectors are obtained with the help of the derivative of the position vectors with respect to the co- and contravariant curvilinear coordinates ξ_i, ξ^i.

$$\begin{aligned} \mathbf{x} = x^i \mathbf{e}_i = \xi_i \mathbf{g}^i = \xi^i \mathbf{g}_i \qquad &\longrightarrow \mathbf{g}_i = \frac{\partial \mathbf{x}}{\partial \xi^i}. \\ \mathbf{X} = X^i \mathbf{e}_i = \xi_i \mathbf{G}^i = \xi^i \mathbf{G}_i \qquad &\longrightarrow \mathbf{G}_i = \frac{\partial \mathbf{X}}{\partial \xi^i}. \end{aligned} \tag{3.2}$$

The appropriate transformation of covariant and contravariant bases using the respective metrics is given in Table 3.1 below.

	Deformed	Reference
Covariant Base Vectors	$\mathbf{g}_i = g_{ij}\mathbf{g}^j$	$\mathbf{G}_i = G_{ij}\mathbf{G}^j$
Contravariant Base Vectors	$\mathbf{g}^i = g^{ij}\mathbf{g}_j$	$\mathbf{G}^i = G^{ij}\mathbf{G}_j$
Covariant Metric	$g_{ij} = \mathbf{g}_i \cdot \mathbf{g}_j$	$G_{ij} = \mathbf{G}_i \cdot \mathbf{G}_j$
Contravariant Metric	$g^{ij} = \mathbf{g}^i \cdot \mathbf{g}^j$	$G^{ij} = \mathbf{G}^i \cdot \mathbf{G}^j$

Table 3.1: Co- and contravariant base vectors and metrics.

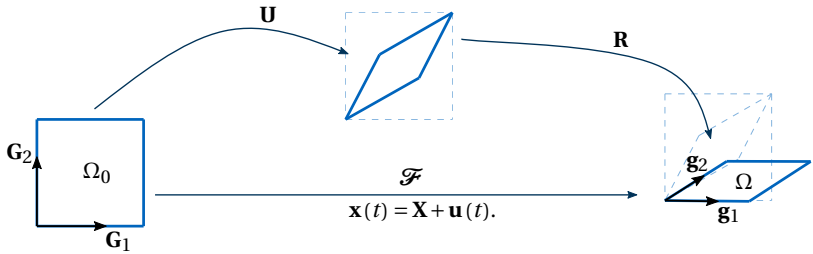

Figure 3.1: Polar Decomposition as described in equation 3.3, adapted from [6].

Additional tensors are used to simplify the element formulations and material descriptions. Figure 3.1 visualizes that any reference domain Ω_0 can be transformed into the current geometry Ω using the deformation gradient $\mathscr{F}$. One possibility is to perform the complete deformation in two steps. Here the right stretch tensor $\mathbf{U}$ describes the stretch, and thus a local shape change and the rotation tensor $\mathbf{R}$ rotates the geometry afterward. The division of the deformation gradient into $\mathbf{U}$ and $\mathbf{R}$ is called polar decomposition [61].

$$\mathscr{F} = \frac{\partial \mathbf{x}}{\partial \mathbf{X}} = \mathbb{I} + \frac{\partial \mathbf{u}}{\partial \mathbf{X}} = \mathbf{g}_i \otimes \mathbf{G}^i = \mathbf{RU}. \tag{3.3}$$

For some of the material formulations that follow later in this work, it is helpful to work with the eigenvalues $\lambda_i^{\#}$ of $\mathbf{U}$. The right Cauchy-Green tensor $\mathbf{C}$ is then calculated, by exploiting the orthonormality of $\mathbf{R}^*$ and doing a spectral decomposition with the help of the eigenvectors $\mathbf{n}_i^{\#}$,

$$\mathbf{C} = \boldsymbol{\mathcal{F}}^T \boldsymbol{\mathcal{F}} = \mathbf{U}^T \mathbf{U} = \left(\lambda_i^{\#}\right)^2 \mathbf{n}_i^{\#} \otimes \mathbf{n}_i^{\#} = C_{ij} \mathbf{G}^i \otimes \mathbf{G}^j. \tag{3.4}$$

The eigenvalues $\lambda_i^{\#}$ of $\mathbf{U}$ describe the principal stretches [6] and can be calculated by solving the associated eigenvalue problem[†]. Instead of the deformation gradient or principal stretches, various strain measures are also suitable for element and material formulation. Especially the geometrically non-linear strain measures, Green-Lagrange $\mathbf{E}$ and Euler-Almansi $\mathbf{e}$ are used.

$$\mathbf{E} = \frac{1}{2}\left(\boldsymbol{\mathcal{F}}^T \boldsymbol{\mathcal{F}} - \mathbb{I}\right) = \frac{1}{2}\left(\mathbf{C} - \mathbb{I}\right) = \frac{1}{2}\left(g_{ij} - G_{ij}\right) \mathbf{G}^i \otimes \mathbf{G}^j. \tag{3.5}$$

$$\mathbf{e} = \frac{1}{2}\left(\mathbb{I} - \boldsymbol{\mathcal{F}}^{-T} \boldsymbol{\mathcal{F}}^{-1}\right) = \frac{1}{2}\left(g_{ij} - G_{ij}\right) \mathbf{g}^i \otimes \mathbf{g}^j. \tag{3.6}$$

Remark: Coaxial Tensors

Following [6]: $\mathbf{E}$, $\mathbf{U}$, $\mathbf{C}$ are coaxial tensors. The eigenvectors, they share, represent the principal stretch directions in the reference configuration.

3.1.2 Momentum Balance

In order to derive the strong form of the structural equilibrium, it is convenient to start at the linear (translational) momentum $\mathbf{L}$. Then, the relation between mass and velocity can be described by integrating the current mass density ρ and the velocity vector field $\dot{\mathbf{u}}$ over the current domain Ω.

$$\mathbf{L} = \int_\Omega \rho \dot{\mathbf{u}} d\Omega. \tag{3.7}$$

With reference to Newton's Second law of motion, the force vector $\mathbf{F}$ can be calculated by the material time derivative $(\dot{\bullet}) = \frac{D(\bullet)}{Dt}$ of $\mathbf{L}$. With the help of Reynolds' Transport Theorem and the mass continuity expression [61] the material time derivative is derived by expressing the balance of linear momentum, where the Nabla operator ∇ calculates the divergence of a tensor $\nabla \cdot (\bullet)$[‡] and J is the determinant[§] $det(\bullet)$ of the deformation gradient $\boldsymbol{\mathcal{F}}$,

$$\dot{\mathbf{L}} = \frac{D}{Dt} \int_\Omega \rho \dot{\mathbf{u}} d\Omega = \int_\Omega \frac{D\left(\rho \dot{\mathbf{u}}\right)}{Dt} + \rho \dot{\mathbf{u}} \left(\nabla \cdot \dot{\mathbf{u}}\right) d\Omega \tag{3.8}$$

[*] $\mathbf{R}^T \mathbf{R} = \mathbb{I}$.

[†] See Appendix B.

[‡] Divergence of a vector field: $\nabla \cdot \mathbf{u} = \frac{\partial u_i}{\partial x_i}$.

[§] $J = det(\boldsymbol{\mathcal{F}})$, also called *Volume Ratio* $J = v/V$. The ratio between the current (deformed) volume v and the reference (undeformed) volume V.

$$\dot{\mathbf{L}} = \int_\Omega \rho\ddot{\mathbf{u}} + \dot{\mathbf{u}}\underbrace{\left(\dot{\rho} + \rho\nabla\cdot\dot{\mathbf{u}}\right)}_{0}{}^{*} d\Omega = \int_\Omega \rho\ddot{\mathbf{u}} d\Omega = \mathbf{F} \tag{3.9}$$

Following [61], the resulting forces $\mathbf{F}$ are the sum of the integrated Cauchy traction vector $\mathbf{t}$ and the body forces $\mathbf{b}$, $\ddot{\mathbf{u}}$ is the acceleration vector field,

$$\mathbf{F} = \int_{\Gamma_\sigma} \mathbf{t} d\Gamma_\sigma + \int_\Omega \mathbf{b} d\Omega = \int_\Omega \rho\ddot{\mathbf{u}} d\Omega. \tag{3.10}$$

Finally the linear momentum balance in equation 3.10 is transformed with the help of Cauchy's stress theorem[†] and the divergence theorem[‡] to Cauchy's first equation of motion [61] using the Cauchy stress tensor $\boldsymbol{\sigma}$,

$$\int_\Omega \nabla\cdot\boldsymbol{\sigma} + \mathbf{b} - \rho\ddot{\mathbf{u}} d\Omega = \mathbf{0}. \tag{3.11}$$

As equation 3.11 holds for an arbitrary domain it can be expressed in its local form - removing the domain integral,

$$\nabla\cdot\boldsymbol{\sigma} + \mathbf{b} - \rho\ddot{\mathbf{u}} = \mathbf{0}, \tag{3.12}$$

resulting in the conservation of momentum [8].

In combination with suitable boundary conditions on the Neumann boundary Γ_σ and the Dirichlet Boundary Γ_u, equation 3.12 describes the strong form of the Initial Boundary Value Problem (IBVP)[§]:

$$\begin{aligned} \Gamma_u: &\quad \mathbf{u} = \mathbf{u}_{\text{pre}}, \\ \Gamma_\sigma: &\quad \mathbf{t} = \mathbf{t}_{\text{pre}}, \\ &\mathbf{u}(t=0) = \mathbf{u}_0, \\ &\dot{\mathbf{u}}(t=0) = \dot{\mathbf{u}}_0, \end{aligned} \tag{3.13}$$

Prescribed values are denoted by $(\bullet)_{\text{pre}}$, while initial values are indicated by $(\bullet)_0$.

---

[*] Mass continuity [61]: $\rho_0 = \rho J$, $\dot{J} = J\nabla\cdot\dot{\mathbf{u}} \longrightarrow \dot{\rho_0} = 0 = J\left(\dot{\rho} + \rho\nabla\cdot\dot{\mathbf{u}}\right)$.

[†] Cauchy's stress theorem [61]: $\mathbf{t} = \boldsymbol{\sigma}\mathbf{n}$, with the normal vector $\mathbf{n}$.

[‡] Divergence theorem [61]: $\int_{\Gamma_\sigma} \mathbf{t} d\Gamma_\sigma = \int_{\Gamma_\sigma} \boldsymbol{\sigma}\mathbf{n} d\Gamma_\sigma = \int_\Omega \nabla\cdot\boldsymbol{\sigma} d\Omega$.

[§] For static cases (time independent) the IBVP reduces to the Boundary Value Problem (BVP) [61].

3.2 Finite Element Method (FEM)

The following chapter introduces the different material laws and structural elements used to simulate the flexible protective structures. The derivation of unique materials and elements is discussed to simplify the independent implementation. In order to meet the requirements of the large deformations of the protection structures, completely geometrically non-linear or co-rotating element formulations are applied. The theoretical background necessary to move from the previous chapter to the final formulations is explained. Afterwards, the principle of virtual work and the derivation of different system matrices like the stiffness matrix, the mass matrix, and the damping matrix is discussed. This is followed by an introduction to possible solution procedures for the structure.

3.2.1 Principle of Virtual Work

To solve the IBVP the FEM is applied using variational principles. Instead of directly solving equation 3.12*, it is integrated over Ω and multiplied with an arbitrary test function,

$$\int_{\Omega} \left(\nabla \cdot \boldsymbol{\sigma} + \mathbf{b} - \rho \ddot{\mathbf{u}}\right) \cdot \delta \mathbf{u} d\Omega = 0. \tag{3.14}$$

This approach is also known as the Galerkin approach [114] and minimizes weighted residuals. To arrive at the principle of virtual work† the arbitrary test functions are chosen to be the virtual displacement field $\delta\mathbf{u}$, which have to vanish on Γ_u. Applying integration by parts‡ and using the gradient of a tensor $\nabla \otimes (\bullet)$, equation 3.14 transforms to the weak form of the IBVP,

$$\int_{\Omega} \boldsymbol{\sigma} : (\nabla \otimes \delta \mathbf{u}) + \rho \ddot{\mathbf{u}} \cdot \delta \mathbf{u} - \mathbf{b} \cdot \delta \mathbf{u} d\Omega - \int_{\Gamma_\sigma} \boldsymbol{\sigma} \delta \mathbf{u} \cdot \mathbf{n} d\Gamma_\sigma = 0. \tag{3.15}$$

Rearranging equation 3.15 and using the virtual Euler-Almansi strain $\delta\mathbf{e}$§ the virtual work δW is derived,

$$\delta W = \underbrace{\int_{\Omega} \boldsymbol{\sigma} : \delta \mathbf{e} d\Omega}_{\delta W_{\text{int}}} + \underbrace{\int_{\Omega} \rho \ddot{\mathbf{u}} \cdot \delta \mathbf{u} d\Omega}_{\delta W_{\text{kin}}} - \underbrace{\left(\int_{\Omega} \mathbf{b} \cdot \delta \mathbf{u} d\Omega + \int_{\Gamma_\sigma} \mathbf{t}_{\text{pre}} \cdot \delta \mathbf{u} d\Gamma_\sigma \right)}_{\delta W_{\text{ext}}} = 0, \tag{3.16}$$

including the virtual internal work δW_{int}, the virtual external work δW_{ext}, as well as the virtual kinetic work δW_{kin}.

---

* An analytical solution for the strong form is only possible in very few cases.

† Also known as the *principle of virtual displacements.*

‡ Integration by parts [61]: $\int_{\Omega} (\nabla \cdot \boldsymbol{\sigma}) \cdot \delta \mathbf{u} d\Omega = -\int_{\Omega} \boldsymbol{\sigma} : (\nabla \otimes \delta \mathbf{u}) d\Omega + \int_{\Gamma_\sigma} \boldsymbol{\sigma} \delta \mathbf{u} \cdot \mathbf{n} d\Gamma_\sigma$.

§ The transformation with the help of the Lie derivative is presented in Appendix A.

While equation 3.16 describes the virtual work in the spatial description, it is beneficial to express δW_{int} in the material description for the following element formulations. It allows the element derivation in a constant frame of reference*, which simplifies many otherwise cumbersome derivations. Relating to the material description the energy conjugated Second Piola-Kirchhoff stress $\mathbf{S}$ and the Green-Lagrange strain $\mathbf{E}$ are needed and transformed accordingly by the Piola transformation†, including the pull-back operation $\boldsymbol{\chi}^{-1}(\bullet)^{\sharp}$ of a contravariant second order tensor [61],

$$\mathbf{S} = J\boldsymbol{\chi}^{-1}(\boldsymbol{\sigma})^{\sharp} = J\boldsymbol{\mathcal{F}}^{-1}\boldsymbol{\sigma}\boldsymbol{\mathcal{F}}^{-T}, \tag{3.17}$$

and respectively the pull-back operation $\boldsymbol{\chi}^{-1}(\bullet)^{\flat}$ of a covariant second order tensor [61],

$$\mathbf{E} = \boldsymbol{\chi}^{-1}(\mathbf{e})^{\flat} = \boldsymbol{\mathcal{F}}^{T}\mathbf{e}\boldsymbol{\mathcal{F}}. \tag{3.18}$$

The equations 3.17 and 3.18 are finally used to express δW_{int} in the material description, integrating over the reference domain Ω_0,

$$\begin{aligned} \delta W_{\text{int}} = \int_{\Omega} \boldsymbol{\sigma} : \delta\mathbf{e}\, d\Omega = \int_{\Omega_0} \boldsymbol{\sigma} : \boldsymbol{\mathcal{F}}^{-T}\delta\mathbf{E}\boldsymbol{\mathcal{F}}^{-1} \overbrace{Jd\Omega_0}^{d\Omega = Jd\Omega_0}, \\ \delta W_{\text{int}} = \int_{\Omega_0} \mathbf{S} : \delta\mathbf{E}\, d\Omega_0. \end{aligned} \tag{3.19}$$

A similar, but more straight-forward operation is needed to transform δW_{kin} with the help of the mass continuity condition [61],

$$\rho_0 = J\rho, d\Omega = Jd\Omega_0 \longrightarrow \delta W_{\text{kin}} = \int_{\Omega} \rho\ddot{\mathbf{u}} \cdot \delta\mathbf{u}\, d\Omega = \int_{\Omega_0} \rho_0\ddot{\mathbf{u}} \cdot \delta\mathbf{u}\, d\Omega_0. \tag{3.20}$$

3.2.2 Discretization in Space

To numerically solve the structural problem, δW must be transformed from a continuous description into a discrete one. To realize this transformation shape functions $\mathbf{N}$ are applied to describe approximated vector fields $(\bullet)^h$ by an interpolation of the discrete nodal element values. This approach can be used to approximate any vector field but is here given exemplarily for $\mathbf{u}$ interpolating the discrete nodal values $\hat{\mathbf{u}}$,

$$\mathbf{u} \approx \mathbf{u}^h = \mathbf{N}\hat{\mathbf{u}}. \tag{3.21}$$

* With objective material tensors, such as $\mathbf{E}$, $\mathbf{U}$, $\mathbf{C}$.

† The *Piola Transformation* is used to transform stress tensors which (in contrast to strains) include a transformation of the integration domain [61]: $J\boldsymbol{\chi}^{-1}(\bullet)^{\sharp}$.

The usage of **N** also allows to express the approximated base vectors in equations 3.2 in a discrete form,

$$\begin{aligned} \mathbf{g}_i^h &= \frac{\partial \mathbf{x}^h}{\partial \xi^i} = \frac{\partial \mathbf{N}}{\partial \xi^i}\hat{\mathbf{x}}, \\ \mathbf{G}_i^h &= \frac{\partial \mathbf{X}^h}{\partial \xi^i} = \frac{\partial \mathbf{N}}{\partial \xi^i}\hat{\mathbf{X}}, \end{aligned} \tag{3.22}$$

which subsequently enables the derivation of strains and also stresses in the discrete form, following equations 3.5 and 3.6.

Finally equation 3.16 is written in a semi-discrete ,

$$\mathbf{M}\ddot{\hat{\mathbf{u}}} + \hat{\mathbf{F}}_{\text{int}}(\hat{\mathbf{u}}) = \hat{\mathbf{F}}_{\text{ext}}, \tag{3.23}$$

with the help of the mass matrix **M**, the external $\hat{\mathbf{F}}_{\text{ext}}$ and internal forces $\hat{\mathbf{F}}_{\text{int}}$, as well as the discrete nodal displacements and accelerations $\hat{\mathbf{u}}$, $\ddot{\hat{\mathbf{u}}}$.

As described in [8, 62], linear viscous damping forces are introduced, extending equation 3.23 to,

$$\mathbf{M}\ddot{\hat{\mathbf{u}}} + \mathbf{D}\dot{\hat{\mathbf{u}}} + \hat{\mathbf{F}}_{\text{int}}(\hat{\mathbf{u}}) = \hat{\mathbf{F}}_{\text{ext}}, \tag{3.24}$$

employing the damping matrix **D** and the discrete nodal velocities $\dot{\hat{\mathbf{u}}}$. The system matrices in equation 3.24 are composed of the respective elemental matrices, which are described in the following.

Remark: Damping Forces

By comparing equations 3.16 to 3.24, it is evident that the latter possesses a term which is lacking in the former equation. The new term represents the Rayleigh damping, which will be explained in more detail shortly. The Rayleigh damping is defined in terms of a linear combination of the mass and the stiffness terms. From a theoretical point of view, the Rayleigh damping terms can be included in a modified equation of motion and, therefore, be consistently accounted for in the derivation of equation 3.16. As mentioned in [62], section *Elastodynamics and Structural Dynamics*, in addition to the inclusion of the inertial proportional term of the Rayleigh damping in the equation of motion, the respective material law needs to be *"modified to account for the stiffness proportional effects"*. Doing so would consistently include the Rayleigh damping terms in the strong and weak forms of the problem. This theoretical framework serves as an explanation for the additional Rayleigh damping terms. However, following the common approach of treating Rayleigh damping in the literature, in the present work the Rayleigh damping terms are introduced at the discrete level without the modification of the stress tensors.

Internal Forces and Tangent Stiffness Matrix

Remark: Proceeding Notation

In order to keep the notation comprehensible, no further distinction is made between approximated and exact material tensors in the following. The material tensors in the calculation of the element matrices and vectors are now to be regarded in their discrete form and thus approximated. The subscripts r, s define nodal degrees of freedom.

The vector of internal element forces $\hat{\mathbf{F}}_{\text{int}}$ can be derived directly from the virtual internal work from equation 3.19. In addition to the stresses resulting from deformations, pre-stresses $\mathbf{S}_0$ are considered.

$$F_{\text{int},r} = \int_{\Omega_0} (\mathbf{S} + \mathbf{S}_0) : \frac{\partial \mathbf{E}}{\partial \hat{u}_r} d\Omega_0. \tag{3.25}$$

Remark: Pre-Stress Application

Appendix H discusses the appropriate choice of the pre-stress $\mathbf{S}_0$ with respect to the practical implementation in the construction process.

Different methods can be used to solve equation 3.24. Most popular is the Newton-Raphson method for solving non-linear equations. However, it requires the first derivative of the internal forces. This results in a matrix, which is called the stiffness matrix $\mathbf{K}$.*

$$K_{rs} = \int_{\Omega_0} \frac{\partial (\mathbf{S} + \mathbf{S}_0)}{\partial \hat{u}_s} : \frac{\partial \mathbf{E}}{\partial \hat{u}_r} + (\mathbf{S} + \mathbf{S}_0) : \frac{\partial^2 \mathbf{E}}{\partial \hat{u}_r \partial \hat{u}_s} d\Omega_0. \tag{3.26}$$

Equation 3.26 can be broken down further by introducing the strain-energy functional Ψ for hyper-elasticity to express $\mathbf{S}$ and the material tangent modulus $\mathbb{C}$,

$$\mathbf{S} = \frac{\partial \Psi}{\partial \mathbf{E}}, \qquad \mathbb{C} = \frac{\partial \mathbf{S}}{\partial \mathbf{E}} = \frac{\partial^2 \Psi}{\partial \mathbf{E} \partial \mathbf{E}}, \tag{3.27}$$

Finally, the stiffness matrix entries can be expressed as,

$$K_{rs} = \int_{\Omega_0} \mathbb{C} : \frac{\partial \mathbf{E}}{\partial \hat{u}_s} : \frac{\partial \mathbf{E}}{\partial \hat{u}_r} + (\mathbf{S} + \mathbf{S}_0) : \frac{\partial^2 \mathbf{E}}{\partial \hat{u}_r \partial \hat{u}_s} d\Omega_0. \tag{3.28}$$

To evaluate equation 3.28, Ψ must be derived for the respective material laws. In section 3.2.6 this is discussed for some selected material laws.

* $\mathbf{K} = \mathbf{K}^T$ holds for conservative force fields $\mathbf{F}_{\text{int}}$. A conservative force field can be written as the gradient of a scalar-valued potential energy function Π_{int}: $F_{\text{int},r} = \frac{\partial \Pi_{\text{int}}}{\partial \hat{u}_r}$. Because its curls must be zero, the following holds: $\frac{\partial F_{\text{int},r}}{\partial \hat{u}_s} - \frac{\partial F_{int,s}}{\partial \hat{u}_r} = 0 = Krs - Ksr$.

Mass Matrix

The following required structural tensor from equation 3.24 is the mass matrix **M**. It scales the accelerations and thus accounts for the inertial forces in the system. The discrete version of equation 3.20 leads to **M**,

$$\int_{\Omega_0} \rho_0 \ddot{\mathbf{u}}^h \cdot \delta\mathbf{u}^h d\Omega_0 = \delta\hat{\mathbf{u}}^T \int_{\Omega_0} \rho_0 \mathbf{N}^T \mathbf{N} d\Omega_0 \ddot{\hat{\mathbf{u}}} d\Omega_0. \tag{3.29}$$

$$\mathbf{M} = \int_{\Omega_0} \rho_0 \mathbf{N}^T \mathbf{N} d\Omega_0. \tag{3.30}$$

In case of an explicit time integration scheme, **M** is normally diagonalized, resulting in a lumped mass matrix $\mathbf{M}_l$. Different approaches are available to derive $\mathbf{M}_l$:

- Sum up all entries in each row to the diagonal entry: $M_{l,rr} = \sum_s M_{rs}$.
- Directly lump the mass to the nodes depending on the respective nodal influence.*

Damping Matrix

Following [8, 62], the structural damping is modeled as a linear viscous damping force: $\hat{\mathbf{F}}_d = \mathbf{D}\dot{\hat{\mathbf{u}}}$. In contrast to **M** and **K** no specific material parameters (like Young's Modulus E, Poisson's Ratio ν or the density ρ_0) are available to define the properties of **D**. Assuming that the damping is proportional to the stiffness and the mass, the Rayleigh damping [2] is used to model **D**,

$$\mathbf{D} = \alpha_d \mathbf{M} + \beta_d \mathbf{K}. \tag{3.31}$$

The two coefficients α_d and β_d must be calculated by solving a system of equations [2, 25], including the circular eigenfrequencies $\omega_{i,j}$ and user-defined damping ratios $\zeta_{i,j}$,

$$\frac{1}{2}\begin{bmatrix} \frac{1}{\omega_i} & \omega_i \\ \frac{1}{\omega_j} & \omega_j \end{bmatrix} \begin{bmatrix} \alpha_d \\ \beta_d \end{bmatrix} = \begin{bmatrix} \zeta_i \\ \zeta_j \end{bmatrix}. \tag{3.32}$$

While α_d scales the mass it can be interpreted as an external damping caused by the surroundings and heavily influences lower eigenfrequencies. In contrast to the external damping, β_d scales the stiffness and represents the internal damping caused by the deformation of the structure.

Remark: Rayleigh Damping

While this approach shines through its simplicity, the user must be aware that this is only an approximation of the true (very complicated) damping behavior.

* E.g. for a triangle: 1/3 of the total element mass to each element node.

3.2.3 Solution Strategies - Discretization in Time

The impact of rocks into flexible protection systems is a dynamic process that cannot be calculated with purely static analysis. The inertias of the structure and the impacting objects strongly influence the structural behavior. To meet these requirements, suitable time integrators must be chosen to solve the IBVP in equation 3.24. With the element matrices presented in section 3.2.2 the IBVP can be solved with a variety of different approaches, of which the two methods used in this thesis are shortly introduced in the following.

Explicit Time Integration

The explicit time integration makes use of the diagonal lumped mass matrix $\mathbf{M}_l$ and thus avoids the time-consuming solution of a system of equations. The solution of equation 3.24,

$$\hat{\ddot{\mathbf{u}}} = \mathbf{M}_l^{-1}\left(\hat{\mathbf{F}}_{\text{ext}} - \hat{\mathbf{F}}_{\text{int}} - \mathbf{D}\hat{\dot{\mathbf{u}}}\right), \tag{3.33}$$

is simplified to straight-forward scalar operations*. Different schemes are available to progress in time, which differ in their accuracy and complexity. While the forward Euler method [114] is first order accurate, the central difference scheme [8] is second order accurate. More accurate explicit time integration schemes are available [67] for the price of an increased complexity.
Within this work the central difference scheme will be applied for which a detailed algorithm can be found in [8] and is shortly introduced in Appendix E.1.
To ensure a stable solution and as result prevent an "unbounded growth of the solution" [8] the choice of a suitable time step Δt is paramount. With respect to [8], Δt is restricted to the time a sound wave needs to travel through the smallest element in the domain and can be derived from the maximal circular eigenfrequency† for rate-independent materials,

$$\Delta t \leq \frac{2}{\omega_{max}}. \tag{3.34}$$

Implicit Time Integration

In contrast to the explicit time integration, the implicit time integration solves the system of equations 3.24 with a Newton-type solution scheme to a given user defined tolerance. While this approach normally allows for a unconditionally stable solution even with large time steps Δt, it requires an iterative solution procedure. The most general method, used within this work for implicit time integration, is the Generalized-α Method [26]. It proceeds in time by calculating the solution values, like $\hat{\mathbf{u}}$, $\hat{\dot{\mathbf{u}}}$, $\hat{\ddot{\mathbf{u}}}$ with respect to 3 parameters $\alpha_m, \alpha_f, \beta_m$. Depending on the choice of these parameters the method is unconditionally stable and can result in a Newmark, Bossak, or even in an explicit time integration. While [26] presents a detailed derivation of the method, Appendix E.2 shortly introduces the basic equations.

* $M^{-1}_{l,rs} = 0$ for $r \neq s$, $\quad M^{-1}_{l,rr} = 1/M_{l,rr}$.
† E.g. for a truss element [124]: $\Delta t \leq l\sqrt{\rho/E}$

3.2.4 Transformation of Reference Coordinate System

Most of the material laws introduced in section 3.2.6 refer to physical parameters like the Young's Modulus E [66], which have normalized units as well as predefined orthogonal material axis for orthotropic material laws. As these quantities relate to a local Cartesian coordinate system, the strains $\mathbf{E}$ and stresses $\mathbf{S}$ must be transformed to a local Cartesian coordinate system $\bar{\mathbf{G}}_i$*, too and are denoted by $(\bar{\bullet})$.

Remark: 1D and 2D Stress States

Since only one and two-dimensional finite elements (without thickness changes) are used in this work, the derivation of three-dimensional strain and stress tensors is omitted at this point. This procedure allows a simplified representation of the material tensors and the derivation of the local reference coordinate systems.

1D

For one-dimensional elements (with no thickness changes), only the first basis vector is interesting. It points along the element axis and is normalized.

$$\bar{\mathbf{G}}_1 = \frac{\mathbf{G}_1}{|\mathbf{G}_1|}. \tag{3.35}$$

2D

For two-dimensional elements the out-of-plane vector $\bar{\mathbf{G}}_3$ is calculated from the cross-product of the two in-plane vectors $\mathbf{G}_1, \mathbf{G}_2$ and then normalized. The first base vector $\bar{\mathbf{G}}_1$ keeps its direction but is also normalized. Then a new second basis vector $\bar{\mathbf{G}}_2$ is calculated so that it is orthogonal to $\bar{\mathbf{G}}_1$ and $\bar{\mathbf{G}}_3$, lies in the element plane, and has a unit length. Thus a new local reference coordinate system is created in which now physical parameters can be used. If an orthotropic material is used, the direction of one of the principal material axes must generally be specified. For example, $\bar{\mathbf{G}}_1$ can be given, projected onto the structural surface, and then an orthonormal coordinate system can be created based on it.

$$\bar{\mathbf{G}}_3 = \frac{\mathbf{G}_1 \times \mathbf{G}_2}{|\mathbf{G}_1 \times \mathbf{G}_2|}, \quad \bar{\mathbf{G}}_1 = \frac{\mathbf{G}_1}{|\mathbf{G}_1|}, \quad \bar{\mathbf{G}}_2 = \frac{\bar{\mathbf{G}}_3 \times \bar{\mathbf{G}}_1}{|\bar{\mathbf{G}}_3 \times \bar{\mathbf{G}}_1|}. \tag{3.36}$$

* Orthonormality: $\bar{\mathbf{G}}_i = \bar{\mathbf{G}}^i$.

Strains and Stresses

Finally, following [61], $\bar{\mathbf{G}}_i$ is used to transform the strains and stresses and to express them in the new local Cartesian coordinate system, [*],

$$\bar{E}_{ij} = E_{kl}\left(\bar{\mathbf{G}}_i \cdot \mathbf{G}^k\right)\left(\mathbf{G}^l \cdot \bar{\mathbf{G}}_j\right) = \bar{E}^{ij\dagger}. \tag{3.37}$$

$$\bar{S}^{ij} = S^{kl}\left(\bar{\mathbf{G}}^i \cdot \mathbf{G}_k\right)\left(\mathbf{G}_l \cdot \bar{\mathbf{G}}^j\right) = \bar{S}_{ij}. \tag{3.38}$$

3.2.5 Voigt Notation

Following [8] the stresses, strains, and tangent material moduli are expressed in Voigt notation ($\tilde{\bullet}$) to utilize their symmetry and only the plane stress state which is of interest for this work.

$$\begin{aligned} \tilde{\mathbf{E}} &= \begin{bmatrix} \bar{E}_{11} & \bar{E}_{22} & 2\bar{E}_{12} \end{bmatrix}^T, \\ \tilde{\mathbf{S}} &= \begin{bmatrix} \bar{S}^{11} & \bar{S}^{22} & \bar{S}^{12} \end{bmatrix}^T, \\ \tilde{\mathbb{C}} &= \begin{bmatrix} \bar{\mathbb{C}}_{1111} & \bar{\mathbb{C}}_{1122} & \bar{\mathbb{C}}_{1112} \\ \bar{\mathbb{C}}_{2211} & \bar{\mathbb{C}}_{2222} & \bar{\mathbb{C}}_{2212} \\ \bar{\mathbb{C}}_{1211} & \bar{\mathbb{C}}_{1222} & \bar{\mathbb{C}}_{1212} \end{bmatrix}. \end{aligned} \tag{3.39}$$

Remark: Voigt Tensors

In this work $\tilde{\mathbf{E}}$ and $\tilde{\mathbf{S}}$, and $\tilde{\mathbb{C}}$ contain the strain, stress, and constitutive[a] components in the local Cartesian coordinate system, which is introduced in subsection 3.2.4.

[a] $\mathbb{C} = \mathbb{C}^{ijkl}\mathbf{G}_i \otimes \mathbf{G}_j \otimes \mathbf{G}_k \otimes \mathbf{G}_l = \bar{\mathbb{C}}_{ijkl}\bar{\mathbf{G}}^i \otimes \bar{\mathbf{G}}^j \otimes \bar{\mathbf{G}}^k \otimes \bar{\mathbf{G}}^l$.

The Voigt notation allows to replace the double contraction in δW_{int} with a single contraction,

$$\delta W_{\text{int}} = \int_{\Omega_0} \mathbf{S} : \delta\mathbf{E} d\Omega_0 = \int_{\Omega_0} \tilde{\mathbf{S}} \cdot \delta\tilde{\mathbf{E}} d\Omega_0, \tag{3.40}$$

and subsequently simplifies the expressions for $\hat{\mathbf{F}}_{\text{int}}$ in equation 3.25 and $\mathbf{K}$ in equation 3.28. See [8, 131] for a derivation of equation 3.39 with the help of static condensation and its three-dimensional stress state form.

[*] $\mathbf{E} = E_{ij}\mathbf{G}^i \otimes \mathbf{G}^j = \bar{E}_{ij}\bar{\mathbf{G}}^i \otimes \bar{\mathbf{G}}^j$.

[†] Holds for an orthonormal base, like $\bar{\mathbf{G}}_i$.

3.2.6 Constitutive Laws

This section introduces and discusses the primary constitutive laws for the simulations presented. These are linear-elastic isotropic and orthotropic constitutive laws for two-dimensional stress states and non-linear and plastic constitutive laws for one-dimensional stress states. The simulations of real-world experiments presented later in this dissertation work with surface elements for the protection meshes and cable, bar, and beam elements for the remaining components of the protection structure. As it will be shown, the strain of the surface elements does not exceed the value of 4.7% since they can often deflect due to their considerable flexibility. Therefore, the low value of 4.7% justifies linear elastic constitutive laws for the surface elements. On the other hand, the cables can yield, and the non-linear constitutive laws allow larger elongation in this case. In addition, a discussion of the appropriate modeling of the compressive slack behavior of the surface elements and the cables follows. Many of the structural elements to be modeled cannot support compressive forces. Modeling this behavior is especially challenging for a two-dimensional stress state.

As mentioned previously, the following constitutive laws are limited to one-dimensional and two-dimensional plane stress states.

3.2.6.1 Elasticity

An elastic constitutive law which can represent finite strains can be described by a Helmholtz free-energy function. Following [61], this function for homogeneous materials is only dependent on the deformation gradient $\boldsymbol{\mathcal{F}}$ and is named strain-energy function. The strain-energy function is subsequently denoted by Ψ. The stresses and tangent material moduli are derived from Ψ. As a basis for the following constitutive laws, the second Piola-Kirchhoff stress $\mathbf{S}$ and the associated tangent material modulus $\mathbb{C}$ are derived as follows,

$$\mathbf{S} = \frac{\partial \Psi}{\partial \mathbf{E}}, \quad \mathbb{C} = \frac{\partial \mathbf{S}}{\partial \mathbf{E}} = \frac{\partial^2 \Psi}{\partial \mathbf{E} \partial \mathbf{E}}. \tag{3.41}$$

St. Venant-Kirchhoff - Plane Stress

The most common isotropic elastic constitutive law is used for preliminary studies and can be advantageous for simplifying structural behavior. It is used, among other things, for the experiment simulation in section 5.1.1. Equation 3.42 expresses the strain-energy function with the help of the trace operator $\mathrm{tr}(\bullet)$ and the two necessary Lamé parameters Υ, Ξ.

$$\begin{aligned} \Psi_{\mathrm{SV}} &= \frac{1}{2}\Xi \mathrm{tr}\,(\mathbf{E})^2 + \Upsilon \mathrm{tr}\left(\mathbf{E}^2\right), \\ \Xi = \frac{E\nu}{(1+\nu)(1-2\nu)}, &\qquad \Upsilon = \frac{E}{2(1+\nu)}. \end{aligned} \tag{3.42}$$

The tangent material modulus for the plane-stress scenario in Voigt notation $\tilde{\mathbb{C}}_{\mathrm{SV}}$ is derived in [131]. The linear elastic behavior allows the expression of $\tilde{\mathbf{S}}$ as a matrix-vector product,

$$\tilde{\mathbb{C}}_{\mathrm{SV}} = \frac{E}{1-\nu^2}\begin{bmatrix} 1 & \nu & 0 \\ \nu & 1 & 0 \\ 0 & 0 & \frac{1-\nu}{2} \end{bmatrix}, \qquad \tilde{\mathbf{S}} = \tilde{\mathbb{C}}_{\mathrm{SV}}\tilde{\mathbf{E}}. \tag{3.43}$$

Especially in large compressive strain regimes the St. Venant-Kirchhoff material law shows considerable flaws and develops artificial instabilities and undesired softening behavior. A detailed discussion of this behavior and its origin is presented in [105].

Münsch and Reinhardt - Plane Stress

Many of the protection mesh structures show an anisotropic deformation behavior in experiments. Two independent orthotropic* directions are tested in these tensile tests, and the results are documented. To use the tensile test data, an orthotropic constitutive law is introduced to model the stiffnesses of the two directions. Figure 3.2 depicts the two test directions. They are projected onto the structural surface before the simulation of rockfall protection meshes and thus represent the principal directions of the material behavior.

Figure 3.2: Orientation of $\bar{\mathbf{G}}_i$ in the wire mesh. Photograph taken in Walenstadt, Switzerland. The respective Young's Moduli for each direction are obtained from tensile tests.

The linear elastic behavior allows the expression of $\tilde{\mathbf{S}}$ as a matrix-vector product of the tangent material modulus $\tilde{\mathbb{C}}_{\mathrm{MR}}$ and the strains $\tilde{\mathbf{E}}$ [131].

* A subset of anisotropic constitutive laws.

$$\tilde{\mathbb{C}}_{\mathrm{MR}} = \frac{1}{1-\nu_{\mathrm{xy}}\nu_{\mathrm{yx}}} \begin{bmatrix} E_x & \nu_{\mathrm{xy}}E_x & 0 \\ \nu_{\mathrm{yx}}E_y & E_y & 0 \\ 0 & 0 & \left(1-\nu_{\mathrm{xy}}\nu_{\mathrm{yx}}\right)G \end{bmatrix}, \qquad \frac{\nu_{\mathrm{xy}}}{E_y} = \frac{\nu_{\mathrm{yx}}}{E_x}, \qquad \tilde{\mathbf{S}} = \tilde{\mathbb{C}}_{\mathrm{MR}}\tilde{\mathbf{E}}. \tag{3.44}$$

The Shear Modulus G, Young's Moduli E_x, E_y, as well as the Poisson's ratios ν_{xy}, ν_{yx} must be defined in the local Cartesian coordinate system and can be obtained from experiments.

3.2.6.2 Tension-Field (TF) Theory

Similar to real membrane structures, the protection mesh structures are not capable of carrying in-plane compression forces. A solution to model this behavior for one-dimensional structures, like cables, is straightforward as described in section 3.2.7.2. For the two-dimensional plane-stress state a more sophisticated but fundamentally similar approach is necessary. Following the derivation in [86, 87] the Tension-Field (TF) assumes zero-bending stiffness in the membrane. This assumption results in a sudden out-of plane deformation of the membrane if compression stresses develop. To model the incapability of the membrane structure to withstand compression stresses the TF transforms $\tilde{\mathbb{C}}$ with respect to the principal stresses. This results in a new material modulus $\tilde{\mathbb{C}}'$, which is rotated to ignore compression forces. The new stress can be determined via a matrix-vector product with the current strains for linear elastic material laws.
The result is a compression-free stress state $\tilde{\mathbf{S}}'$.

(a) Ring mesh. (b) Wire mesh.

Figure 3.3: The flexible protection structures can not carry in-plane compression stresses and rather escape out-of plane if compressed.

The transformation of $\tilde{\mathbb{C}}$ is independent of the constitutive law and can be applied to both constitutive laws introduced in the previous section 3.2.6.1.

Algorithm 1 Modify stresses and strains for wrinkled membranes, following [86, 87]

Solve for principal stresses $\lambda^{\#}$ ▷ Eq. 3.45
Calculate principal strains $\tilde{\mathbf{E}}(\lambda^{\#})$
if $min(\lambda^{\#}) > 0$ **then**
    Membrane state: *taut*
    $\tilde{\mathbb{C}}' = \tilde{\mathbb{C}}$
    $\tilde{\mathbf{S}}' = \tilde{\mathbf{S}}$
else if $max(\tilde{\mathbf{E}}(\lambda^{\#})) \leq 0$ **then**
    Membrane state: *slack*
    $\tilde{\mathbb{C}}' = \mathbf{0}$
    $\tilde{\mathbf{S}}' = \mathbf{0}$
else if $max(\tilde{\mathbf{E}}(\lambda^{\#})) > 0$ and $min(\lambda^{\#}) \leq 0$ **then**
    Membrane state: *wrinkle*
    Use $\mathbf{n}^{\#}$ of min $(\lambda^{\#})$ to derive $\mathbf{n}_w$ ▷ Eq. 3.46
    Calculate $\tilde{\mathbb{C}}'$ ▷ Eq. 3.47
    $\tilde{\mathbf{S}}' = \tilde{\mathbb{C}}'\tilde{\mathbf{E}}$ for linear elasticity.
else
    Calculation failed.

The necessary principal stresses can be obtained by solving the associated eigenvalue problem*,

$$\left(\mathbf{S} - \mathbb{I}\lambda^{\#}\right)\mathbf{n}^{\#} = \mathbf{0}, \tag{3.45}$$

containing the eigenvalues $\lambda^{\#}$, the principal stresses, and the corresponding eigenvectors $\mathbf{n}^{\#}$.
In case algorithm 1 detects a wrinkling membrane state, based on the principal stresses and strains, the wrinkling direction vector $\mathbf{n}_w$ needs to be calculated,

$$\mathbf{n}_w = \begin{bmatrix} \mathbf{n}^{\#}(min(\lambda^{\#}))_0 \, \mathbf{n}^{\#}(min(\lambda^{\#}))_0 \\ \mathbf{n}^{\#}(min(\lambda^{\#}))_1 \, \mathbf{n}^{\#}(min(\lambda^{\#}))_1 \\ 2\mathbf{n}^{\#}(min(\lambda^{\#}))_0 \, \mathbf{n}^{\#}(min(\lambda^{\#}))_1 \end{bmatrix}. \tag{3.46}$$

Finally the modified constitutive matrix $\tilde{\mathbb{C}}'$ is derived by an operation similar to subtracting the compression contribution from the original reference material tangent modulus $\tilde{\mathbb{C}}$ [86],

$$\tilde{\mathbb{C}}' = \tilde{\mathbb{C}} - \frac{\tilde{\mathbb{C}}\mathbf{n}_w \cdot \mathbf{n}_w^T \tilde{\mathbb{C}}}{\mathbf{n}_w^T \tilde{\mathbb{C}} \cdot \mathbf{n}_w}. \tag{3.47}$$

The implementation of this law is verified by simulating the inflation of a thin membrane cushion, as discussed in [87]. Good agreement with the results is obtained and the stress result, for the minimal principal stress is plotted in Figure 3.4. Clearly, without the TF, unrealistic compression stresses develop in the membrane.

* The derivation is presented in Appendix B.

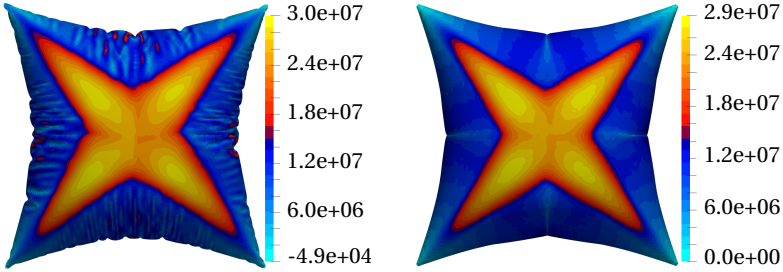

(a) Without the TF: Unfeasible compression stresses develop in the thin membrane cushion.

(b) Applying the TF: The stresses rearrange in the membrane, omitting compression stresses.

Figure 3.4: Simulation of an inflated thin membrane cushion and visualization of the minimum principal second Piola-Kirchhoff stress in N/m^2. The problem setup is taken from [87] and good agreement with the results is obtained.

3.2.6.3 1D Hyper-Elasticity: Ogden and the Transformation to other Constitutive Laws

Following [6, 65], one of the most general hyper-elastic constitutive laws is the Ogden law [92]. With the correct values chosen it can easily be transferred to other constitutive laws, such as St. Venant-Kirchhoff or Neo-Hookean. To provide the necessary entities for the simulation of various hyper-elastic laws for one-dimensional structures, such as the cables in the flexible protection structures, a short summary of the Ogden law and its transformation to other laws is given.

The strain energy function for the Ogden law reads [6, 65],

$$\Psi_O\left(\lambda_1^\#, \lambda_2^\#, \lambda_3^\#\right) = \sum_{i=1} \frac{\gamma_{O,i}}{\beta_{O,i}} \left(\left(\lambda_1^\#\right)^{\beta_{O,i}} + \left(\lambda_2^\#\right)^{\beta_{O,i}} + \left(\lambda_3^\#\right)^{\beta_{O,i}} - 3 \right) \tag{3.48}$$

where $\lambda_i^\#$ are the eigenvalues* of the right stretch tensor $\mathbf{U}$, as given in equation 3.4. γ_O, β_O are Ogden material parameters to be defined by the user.
To apply the Ogden law to one-dimensional stress states (truss, cable elements) the following simplifications are applied:

- $\nu = 0$, no consideration of the Poisson effect and thus no change of the cross-section.
- $\lambda_1^\# = \lambda^\# = \frac{l}{L} = \mathcal{F}$, the first principal stretch equals the stretch of the element along its axis. $\mathcal{F}$ is the one-dimensional deformation gradient, l represents the deformed element length, and L the undeformed (reference) length.

* Principal stretches.

- $\lambda_2^{\#} = \lambda_3^{\#} = 1$.
- $\mathscr{F} = J = v/V = \lambda^{\#} = \frac{l}{L}$, with $\nu = 0$ the cross area remains constant and the change in volume is only described by the change in length.

These simplifications allow to express equation 3.48 with respect to the first principal stretch,

$$\Psi_O\left(\lambda^{\#}\right) = \sum_{i=1} \frac{\gamma_{O,i}}{\beta_{O,i}} \left(\left(\lambda^{\#}\right)^{\beta_{O,i}} - 1\right) = \Psi_O\left(\mathscr{F}\right). \tag{3.49}$$

Following [6, 61, 65] the first Piola-Kirchhoff stress tensor **P** can be derived,

$$\bar{P}_{11} = \frac{\partial \Psi}{\partial \mathscr{F}} = \frac{\partial \Psi}{\partial \lambda^{\#}} = \frac{E}{\beta_{O,1} - \beta_{O,2}} \left(\left(\lambda_1^{\#}\right)^{\beta_{O,1}-1} - \left(\lambda_1^{\#}\right)^{\beta_{O,2}-1}\right), \tag{3.50}$$

which can be directly transformed to the second Piola-Kirchhoff stress tensor **S**,

$$\bar{S}_{11} = \mathscr{F}^{-1} \bar{P}_{11} = \frac{1}{\lambda^{\#}} \bar{P}_{11} = \frac{E}{\beta_{O,1} - \beta_{O,2}} \left(\left(\lambda_1^{\#}\right)^{\beta_{O,1}-2} - \left(\lambda_1^{\#}\right)^{\beta_{O,2}-2}\right). \tag{3.51}$$

With the reformulation of the strain - principal stretch relation,

$$\bar{E}_{11} = \frac{1}{2}\left(\frac{l^2}{L^2} - 1\right) = \frac{1}{2}\left(\left(\lambda^{\#}\right)^2 - 1\right) \longrightarrow \lambda^{\#} = \sqrt{2\bar{E}_{11} + 1}, \tag{3.52}$$

the second Piola-Kirchhoff stress reads,

$$\bar{S}_{11}\left(\bar{E}_{11}\right) = \frac{E}{\beta_{O,1} - \beta_{O,2}} \left[\left(2\bar{E}_{11} + 1\right)^{\beta_{O,1}/2-1} - \left(2\bar{E}_{11} + 1\right)^{\beta_{O,2}/2-1}\right], \tag{3.53}$$

and with the help of equation 3.41 the material tangent modulus is expressed,

$$\begin{aligned} \bar{\mathbb{C}}_{1111} = & \frac{E}{\beta_{O,1} - \beta_{O,2}} \cdot \\ & \left[\left(\beta_{O,1} - 2\right)\left(2\bar{E}_{11} + 1\right)^{\beta_{O,1}/2-2} - \left(\beta_{O,2} - 2\right)\left(2\bar{E}_{11} + 1\right)^{\beta_{O,2}/2-2}\right]. \end{aligned} \tag{3.54}$$

The advantage of the preceding derivation lies in the general structure of equations 3.53 and 3.54. With the help of the appropriate material parameters, the stresses and the material tangent moduli for other constitutive laws can be obtained from these equation. The following table 3.2 gives the appropriate values for the St. Venant-Kirchhoff and the Neo-Hookean law.

	$\beta_{O,1}$, $\beta_{O,2}$	$\bar{S}_{11}$	$\bar{\mathbb{C}}_{1111}$
Ogden	Arbitrary	Equation 3.53	Equation 3.54
St. Venant-Kirchhoff	4, 2	$E\bar{E}_{11}$	E
Neo-Hookean	2, 0	$\left(E\bar{E}_{11}\right)/\left(2\bar{E}_{11}+1\right)$	$E/\left(2\bar{E}_{11}+1\right)^2$

Table 3.2: Transformation from Ogden to St. Venant-Kirchhoff and Neo-Hookean.

3.2.6.4 1D: Plasticity - Isotropic Linear Hardening

To dissipate as much energy as possible the support cables of flexible protection structures often do not connect directly to the ground. Instead, braking elements are installed, connecting the cables and the foundation, as presented in Figure 2.4. These braking elements are highly ductile and absorb a lot of energy by plastic deformation* and friction.

Remark: FEM Modeling of Braking Elements

This work models the braking elements as single truss elements, described in section 3.2.7.1, combined with a linear isotropic[a] hardening plasticity law.

[a] The simplification of the rather complex hardening behavior to an isotropic hardening rule assumes the yield surface to dilate instead of translating.

The results of this chapter are close to the content given in [36] and are additionally simplified to a one-dimensional stress state. First, a yield function Φ needs to be postulated (using $|\bullet|$ to express the absolute value of a given scalar). Several new symbols are needed to be reintroduced at this point: The one-dimensional yield stress $\bar{S}_y$, the hardening modulus E_h, the internal hardening variable α_y, and the one-dimensional pre-stress $\bar{S}_0$ in a local Cartesian coordinate system.

$$\Phi\left(\bar{S}_{11},\bar{S}_0,\bar{S}_y,\alpha_y\right) = |\,\bar{S}_{11}+\bar{S}_0\,| - \left(\bar{S}_y + E_h\alpha_y\right) \leq 0. \tag{3.55}$$

The stress is calculated with respect to the one-dimensional elastic strain $\bar{E}_{\text{elastic}}$ only. Consequently, the one-dimensional plastic strain $\bar{E}_{\text{plastic}}$ needs to be subtracted from the total strain,

$$\bar{S}_{11} = E\bar{E}_{\text{elastic}} = E\left(\bar{E}_{11} - \bar{E}_{\text{plastic}}\right). \tag{3.56}$$

* The accumulated plastic strain remains after complete unloading.

Additionally, the plastic multiplier $\dot{\gamma}_y$ is introduced to express the flow rule, which relates the time derivative of the plastic strain to the sign $sgn(\bullet)$ of the current stress state, if $\Phi = 0$[*],

$$\dot{\bar{E}}_{plastic} = \dot{\gamma}_y sgn\left(\bar{S}_{11} + \bar{S}_0\right). \tag{3.57}$$

Subsequently, following [36] the Kuhn-Tucker condition and respectively the consistency condition can be expressed,

$$\dot{\gamma}_y \Phi = 0, \qquad \dot{\gamma}_y \dot{\Phi} = 0. \tag{3.58}$$

Finally, with $\dot{\gamma}_y = \dot{\alpha_y}$ the plastic multiplier is derived for the case $\dot{\gamma}_y > 0$[†],

$$\dot{\Phi} = 0 \longrightarrow \dot{\gamma}_y = \frac{E\dot{\bar{E}}_{11} sgn\left(\bar{S}_{11} + \bar{S}_0\right)}{E + E_h}, \tag{3.59}$$

and the elastic-plastic[‡] tangent modulus E_p,

$$E_p = \frac{EE_h}{E + E_h}. \tag{3.60}$$

Depending on whether additional plastic or elastic deformations develop, the change in the stress state can be calculated using the following Table 3.3.

Elasticity: $\Phi < 0$	Plasticity: $\Phi = 0$
$\dot{\bar{S}}_{11} = E\dot{\bar{E}}_{11}$	$\dot{\bar{S}}_{11} = E_p\dot{\bar{E}}_{11}$

Table 3.3: Calculating the current change in stress state.

[*] $\Phi = 0$: The stress state is on the yield surface.
[†] Extra plastic deformation.
[‡] E_p relates to the total strain, whereas E_h relates to the plastic strain only.

3.2.7 Finite Element Models

In order to capture the correct deformation behavior of the protection structures, suitable element formulations must be chosen for the respective structural components. This section introduces the most important element formulations and discusses their real world counterparts. Depending on their load-carrying behavior, truss, cable, plate in membrane action, and beam elements are applied and shortly introduced. All elements are derived to be completely geometrically nonlinear or use a co-rotating frame if they have rotational degrees of freedom.

3.2.7.1 Truss

In order to allow large deformations, it is typically attempted to transfer forces via tension and generally normal forces, omitting bending. To this end, most of the supports of the protective structures contain moment hinges, and cables are used to span the nets to the rock-face or the ground. For components that only carry normal forces, modeling with the aid of one-dimensional truss and cable finite elements is suitable. Depending on the ability to bear compressive forces, a distinction between truss and cable elements is made. Figure 3.5 shows which structure parts are modeled in this way.

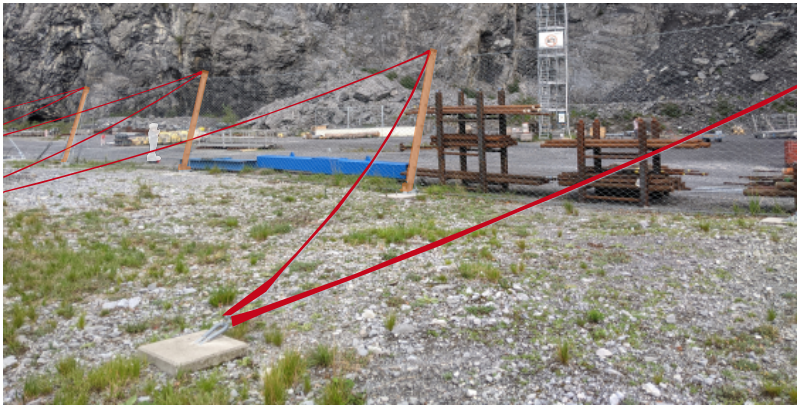

Figure 3.5: Depiction of the application of truss finite elements in the construction of the flexible protection structure. The columns highlighted in orange will be modeled with trusses. Entities highlighted in red will be modeled with cable elements, described in subsection 3.2.7.2. Photograph taken in Walenstadt, Switzerland.

With respect to Figure 3.5 the columns are modeled with trusses because they can carry compression forces and are not clamped at the foundation as demonstrated in Figure 2.5. Cable finite elements, which cannot carry compression forces, are employed to model the cables and are described in subsection 3.2.7.2.

A truss element is defined by two nodes n_i, n_j and has only translational nodal degrees of freedom. Figure 3.6 depicts the geometric description and the map from the reference frame to the deformed geometry.

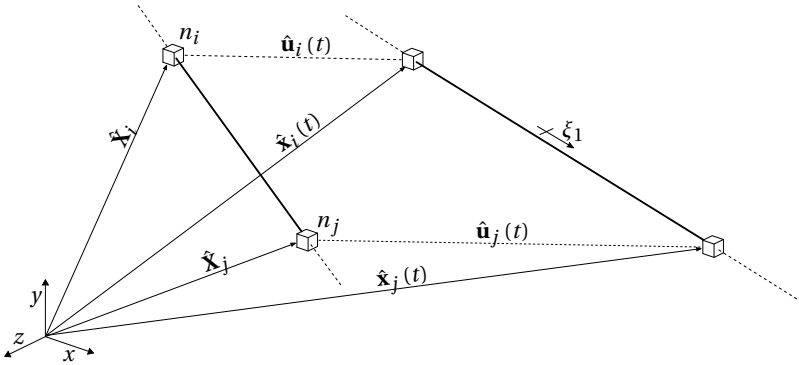

Figure 3.6: Spatial mapping between reference and current configuration, adapted from [106].

The three-dimensional virtual work equation 3.19 can be simplified to one dimension, resulting in the following scalar operation.

$$\delta W_{\text{int}} = \int_{\Omega_0} \left(\bar{S}^{11} + \bar{S}_0\right) \delta \bar{E}_{11} \, d\Omega_0 = \int_{\Omega_0} \left(\bar{S}_{11} + \bar{S}_0\right) \delta \bar{E}_{11} \, d\Omega_0, \tag{3.61}$$

$$\bar{E}_{11} = 0.5 \left(l^2 - L^2\right) / L^2. \tag{3.62}$$

Arbitrary material laws can be used to calculate the stresses in equation 3.61, such as presented in sections 3.2.6.3 and 3.2.6.4.

3.2.7.2 Cable

The cable element plays a crucial role in the modeling of flexible protective structures, as demonstrated in Figure 3.5. While it can only carry tensile forces, stability problems do not arise, resulting in smaller cross-sections and longer spans. The cables will be modeled by single geometrically non-linear cable finite elements with two nodes. The formulation is the same as for the truss element presented in subsection 3.2.7.1 with an additional check for compression stresses:

$$\text{if} \quad \bar{S}^{11} + \bar{S}_0 < 0.0: \qquad \hat{\mathbf{F}}_{\text{int}} = \mathbf{0}, \qquad \mathbf{K} = \mathbf{0}, \qquad \mathbf{M} = \mathbf{M}. \tag{3.63}$$

While the internal forces $\hat{\mathbf{F}}_{\text{int}}$ and the stiffness matrix $\mathbf{K}$ will be omitted in the construction of the global system of equations, the mass of the element, represented by the mass matrix $\mathbf{M}$, needs to be kept in the system. This relates to the actual behavior of the structure, which will not be supported by a cable under compression but will still be subjected to the dead load of the element.

3.2.7.3 Sliding Cable

To allow for large deformations the wire mesh of the protection structures is typically connected to the carrier ropes by shackles. Instead of fixing the connection rigidly the shackles are free to move along the carrier rope, only restricted by friction as depicted in Figures 3.7, 3.8b. Additionally, guide rollers redirect the carrier ropes, which is shown to the very left of Figure 3.7 and in Figure 3.8a.

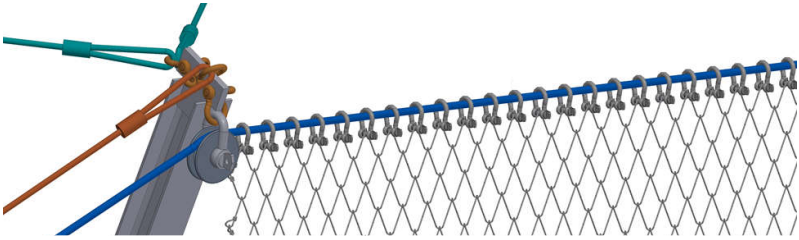

Figure 3.7: Sketch of upper rope installation, taken from [51] and adapted from [103], compare with Figure 3.8a. The blue line depicts the structural part which is modeled by the sliding cable element.

(a) Edge installation.

(b) Upper rope installation.

Figure 3.8: Photographs of the real world model of the sliding cable element, taken in Walenstadt, Switzerland.

Remark: Alternative Modeling of Sliding Nodes

A variety of different modeling approaches have been tested in the course of this work, of which the best one is presented in this section. Alternative models and a comparison are discussed in the Appendix C.

[13, 124] describe a sliding cable element formulation which inherently handles the sliding of inner nodes and allows the efficient inclusion of friction. The for-

mulation calculates the strain with respect to the change of the total length of the element instead of the single line segments and has a constant normal force if no friction is considered.

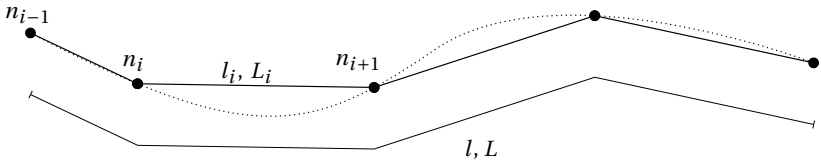

Figure 3.9: FEM discretization of sliding cable element, adapted from [103].

Figure 3.9 depicts the discretization of one single element with an arbitrary number of inner nodes. The real cable is simplified with linear line segments spanning between the inner nodes with each length being l_i in the deformed configuration and L_i in the reference configuration. The single line segments lengths sum up to the total length of the whole element [13, 106],

$$l = \sum_{i}^{n_{\text{lines}}} l_i, \qquad L = \sum_{i}^{n_{\text{lines}}} L_i, \qquad \longrightarrow \bar{E}_{11} = 0.5\left(l^2 - L^2\right)/L^2. \tag{3.64}$$

Finally, the virtual internal work equation is expressed, following [13, 106],

$$\delta W_{\text{int}} = \frac{l}{L} A\left(\bar{S}_{11} + \bar{S}_0\right) \begin{bmatrix} -\Delta\hat{x}_1/l_1 \\ -\Delta\hat{y}_1/l_1 \\ -\Delta\hat{z}_1/l_1 \\ \Delta\hat{x}_{i-1}/l_{i-1} - \Delta\hat{x}_i/l_i \\ \Delta\hat{y}_{i-1}/l_{i-1} - \Delta\hat{y}_i/l_i \\ \Delta\hat{z}_{i-1}/l_{i-1} - \Delta\hat{z}_i/l_i \\ \dots \\ \Delta\hat{x}_{n_{\text{nodes}}-1}/l_{n_{\text{nodes}}-1} \\ \Delta\hat{y}_{n_{\text{nodes}}-1}/l_{n_{\text{nodes}}-1} \\ \Delta\hat{z}_{n_{\text{nodes}}-1}/l_{n_{\text{nodes}}-1} \end{bmatrix}^T \cdot \delta\hat{\mathbf{u}}, \tag{3.65}$$

which uses the direction of the resulting internal forces at each internal node and the reference cross-section A. Equation 3.65 makes use of the discrete coordinate distance between two internal nodes, e.g. $\Delta\hat{x}_i = \hat{x}_{i+1} - \hat{x}_i$.
Adapting the approach by [124], the influence of the friction on the internal forces can be efficiently handled by first calculating the norm $\| \bullet \|$ of the resulting inner force at each node $\| \hat{\mathbf{F}}_{\text{int},i} \|$ and then multiplying it with a given friction value μ,

$$\Delta\bar{S}_{11,i} = \mu \| \hat{\mathbf{F}}_{\text{int},i} \| . \tag{3.66}$$

The additional friction force $\Delta\bar{S}_{11,i}$ is finally included in the total normal force at n_i in the cable, which would be constant along the element without any friction.

Sliding Cable Net Demonstration

Figure 3.10 demonstrates the structural behavior of a plane cable net spanning between two sliding cable elements on both sides subjected to gravity. The influence of the friction can clearly be distinguished, restricting the movement of the edge nodes.

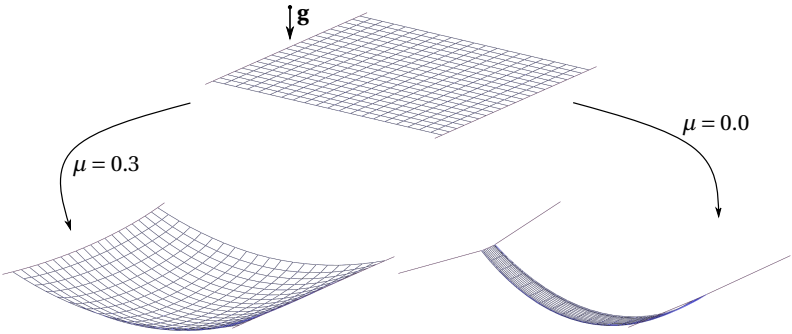

Figure 3.10: Plane cable net discretized with cable elements subjected to gravity **g** for different friction values μ on the edge cables. The edge cables are represented by the sliding cable element formulation.

3.2.7.4 Plate in Membrane Action

As described in [37, 100, 104] plate in membrane action elements are suitable to approximate the behavior and response of rockfall protection structures. With respect to the mesh geometry, depicted in Figure 3.11 a homogenized surface discretization will be applied using triangular plate in membrane action elements to model the appropriate structural response for these kind of wire meshes. In combination with a suitable material law* the structural deformation behavior can be suitably approximated.

Remark: Efficient Modeling

This is in contrast to publications, such as [83, 117] which apply shell elements or even [43] which models each of the connections in the wire mesh with so-called "chain-link" elements. A more simplified but more efficient approach is chosen in this work to maximize efficiency and minimize computational cost while still closely approximating the realistic global structural deformation behavior, as will be shown in sections 5.1 and 5.2.

In contrast to the one-dimensional elements, which are presented in the preceding sections, a two-dimensional stress state is observed in the plate in membrane

* Of which the most important ones in this work are presented in the subsections 3.2.6.1 and 3.2.6.2.

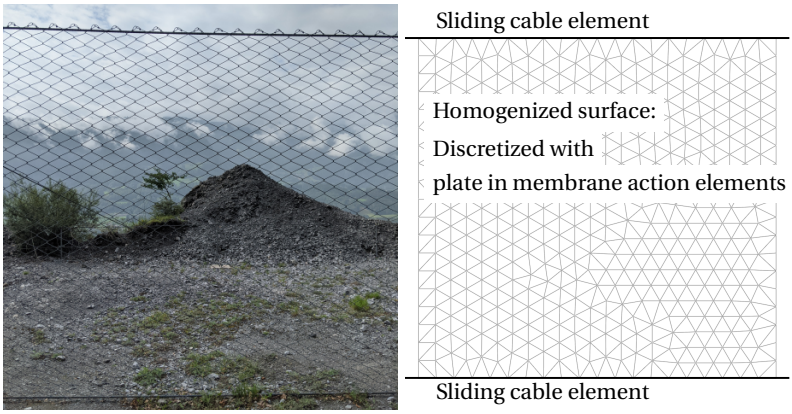

Figure 3.11: Discretizing the wire mesh structure with triangular plate in membrane action finite elements. The homogenization of the surface still allows for penetration of small particles as will be shown in section 4.

action elements. To model the realistic deformation behavior of the wire meshes, compression stresses should be excluded by applying the TF theory, introduced in subsection 3.2.6.2. Figure 3.12 demonstrates the structural behavior after impact of a single sphere under gravitational loads for both cases: Including and respectively excluding compression stresses.

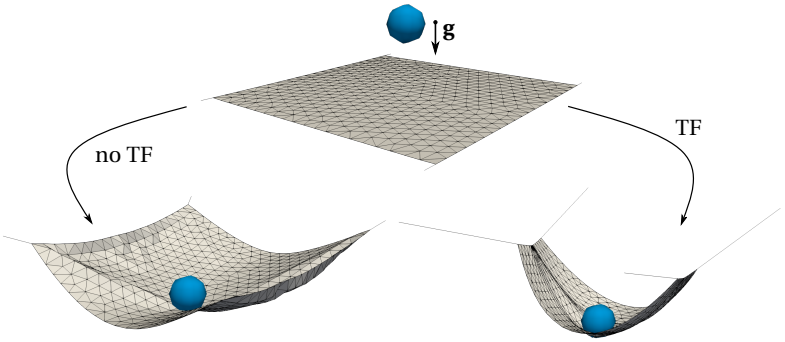

Figure 3.12: Plane cable net discretized with triangular plates in membrane action including sliding cable elements on the edges, adapted from [102]. A sphere subjected to gravity **g** impacts the plane. Using the TF theory, introduced in subsection 3.2.6.2, the unrealistic compression stresses are excluded and a realistic deformation figure is obtained.

Remark: Small Particle Penetration of Homogenized Surface

The coupling approach which will be introduced in chapter 4 handles the interface in such a way that small particles are still able to penetrate the wire-mesh but at the same time use the approach of a homogenized surface structure.

Geometric Shear Stiffness of Pre-Stressed Cable Nets

In order to justify the simplifications of the load-bearing behavior of cable nets with a homogenized plane structure, it is not sufficient to argue only that both structures have no bending stiffness. An important aspect is also the consideration of the geometric in-plane shear stiffness. For a plate in membrane action element, shear stiffness terms are inherent in the element formulation. This is not the case for a cable element.
However, as soon as a cable net is pre-stressed, additional terms develop in the tangent stiffness matrix, granting the elements a stiffness against deformations non-parallel to their axis already in the undeformed configuration.
A more practical explanation can be found in the recoil force of the $P-\Delta$ effect. Figure 3.13 explains the development of recoil forces $P \cdot \frac{\Delta}{L}$ in a pre-stressed cable net, which result in a geometric shear stiffness of the total structure.

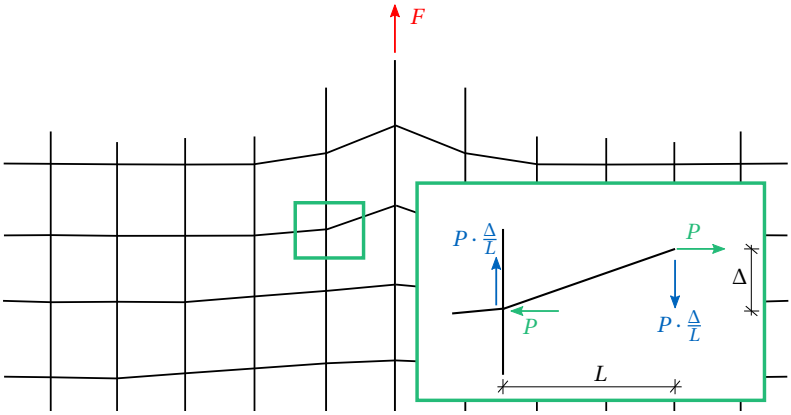

Figure 3.13: Visualization of the $P-\Delta$ effect in a pre-stressed cable net. The notation deviates from this thesis and is chosen to keep the symbols which are used in common literature for the $P-\Delta$ effect. The background figure of the cable net is extracted from [75].

The special research report on the construction of the roofing of the Olympic Stadium in Munich [75] deals, among other things, with the question of the geometric shear stiffness of pre-stressed cable nets.

Two comments are to be quoted here*:

- *"Due to the pre-stressing, it [the cable net] acquires a geometric shear stiffness even in the net surface."*
- *"Individual forces acting on the edge or within the net surface are distributed via nodal displacements. The shear stiffness increases with the magnitude of the pre-stressing."* †

For this reason, a pre-stressed cable net does indeed exhibit a geometric shear stiffness and thus reinforces the assumption that a simplification per homogenized plane structures is applicable.

3.2.7.5 Co-Rotational Beam

For the simulation of impact on the supporting columns beam elements must be used instead of truss elements, as they can carry moments and shear forces. Impact on the columns can result in the destruction of the supporting structure as shown in Figure 3.14.

(a) Column with plastic damage. (b) Detailed view of the damage zone.

Figure 3.14: Impact on the columns can lead to the destruction of the supporting structure. Photographs taken in Walenstadt, Switzerland.

A co-rotating element formulation is used for the beam, which is derived in [7, 71]. The co-rotating element formulation allows to use a linear element formulation to simulate large deformations by describing a co-rotating frame to the finite element which efficiently handles large rotations. It extracts rigid body movements from the total deformation state. While this approach allows to avoid a cumbersome derivation of a complete geometrically non-linear element formulation it is restricted to small deformations within the co-rotating frame.

* Freely translated from [75] p. 9.
† Refers to Figure 11 of [75] p. 9.

3.3 Discrete Element Method (DEM)

To model the impacting objects, this work uses the DEM. The general framework, including all important features, such as contact detection, contact force calculation, and appropriate time integration, have already been implemented in KRATOS at the beginning of this dissertation. The whole workflow has been adapted in the coupled simulations, while adjustments and additions to the code had to be done during the development process. Especially to realize the strong coupling, which will be presented in section 4, a detailed review of the existing code and major changes were necessary. Additionally, the idea of using clusters of single spheres to model arbitrary-shaped objects was extensively investigated. A detailed review of the DEM theory has been performed, of which the most important aspects will be discussed in the proceeding section. The findings lay the foundation for the following sections about the partitioned coupling scheme.

The DEM is a discrete particle method whose particular strengths lie in efficiently analyzing the motion and interaction of individual particles. One of its key features is the usage of an efficient and fast explicit time integration. The method is used in many industries, especially when the interaction between granular materials or rigid objects with large motions and continuous systems is of interest. Thereby the applications are numerous and range from the thermomechanical behavior [57] of contact between frictional bodies [21, 35], assessment of strains in the simulation of shot peening [11, 85], races and balls in ball bearings [4, 15, 118], general tribological systems [69, 78] such as the simulation of rail tracks [53, 54, 89], to more advanced investigations, including fracture due to blast loads [94] and granular flows [55]. But also production processes such as rotating machinery [22] for industrial grain distribution systems and the interaction of particles with fluids [29] can be investigated using the DEM.

The method was first proposed by [32] and has been increasingly used since then. [80] describes the underlying theories of DEM, while many publications deal with the detailed analysis of contact formulations. Special mention should be made of [108], who have done fundamental work on this topic. Building on this, [31, 107, 120] have described improved formulations and contact models, contributing to the current state of the art. Some of their important findings are part of the discussion about the appropriate formulation of contact forces and are discussed in section F. A detailed description of contact search and computation between discrete spherical particles and boundary conditions discretized by finite elements was presented by [98, 99], which form the basis for the present work. [63] carried out a detailed study of suitable time integrators, especially concerning the integration of rotational motion, which is of great importance in the present case.

To model arbitrarily shaped objects while keeping the efficient contact algorithms for spheres, clusters of single spherical elements are used within this work. This approach was formulated by [68] and subsequently used by [103, 104] for the analysis of rockfall events. [104] performs a refinement study, which is presented in section 5.1.1. This flexible modeling strategy allows simple contact algorithms without compromising the approximate modeling of irregular rock geometries. As mentioned earlier, experiments confirm that the rotation of impacting objects

has a significant effect on the overall behavior of the impact, so the shape of the rock must be taken into account. For example, disk-shaped rocks typically have much higher rotational energy than cube-shaped ones.

3.3.1 Solution Procedure

The DEM in this work is penalty based and calculates the current contact forces with respect to the overlap between the respective contact partners. Therefore, the matching contact partners must first be found to calculate their overlap. Once this step is completed, the contact forces can be calculated with the help of suitable contact laws. Finally, the forces and the particle inertias are used to solve the equation of motion and calculate the displacements, velocities, and accelerations.

The basic steps in a DEM simulation are:

Step	Task	Section
1.	Contact detection	3.3.2
2.	Evaluation of contact forces	3.3.3
3.	Integration of motion	3.3.4

Table 3.4: Basic steps of the solution procedure for the DEM.

3.3.2 Contact detection

The contact detection is a crucial part of the overall DEM solution procedure. [98, 99] discuss the contact detection for spherical elements with other spheres, vertices, lines, and surfaces in detail. The use of clusters allows to avoid complex contact algorithms for complicated element geometries as discussed in subsection 3.3.5. The four remaining operations are described in the following.

Sphere - Sphere

The contact between two spheres i, j, as shown in Figure 3.15a, can be efficiently handled by comparing their respective radii R_i, R_j with the distance between their global center coordinates $\mathbf{V}_i, \mathbf{V}_j$ [98],

$$\| \mathbf{V}_i - \mathbf{V}_j \| < R_i + R_j. \tag{3.67}$$

Sphere - Vertex

Similar to the preceding operation the contact between a sphere and a given vertex can be detected by a scalar comparison including the coordinates of the vertex $\mathbf{n}_i$ shown in Figure 3.15b,

$$\| \mathbf{V}_j - \mathbf{n}_i \| < R_j. \tag{3.68}$$

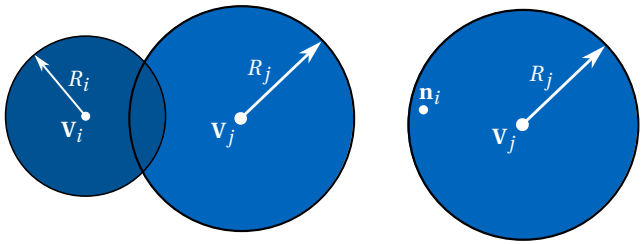

(a) Contact between two spherical elements.

(b) Contact between a sphere and a vertex.

Figure 3.15: Contact including vertices.

Sphere - Edge

For the contact detection between spheres and edges the shortest distance r_i, see Figure 3.16a, between the edge and the center of the sphere $\mathbf{V}_i$ needs to be calculated. The calculation of r_i is given in detail in [98, 99]. As soon as r_i is calculated it is compared to the radius of the sphere to check for contact,

$$r_i < R_i. \tag{3.69}$$

Sphere - Surface

The same operation as for the *sphere - edge* check has to be applied when checking contact with a surface. The shortest distance r_i needs to be calculated by projecting the sphere's center on the surface*. As depicted in Figure 3.16b, r_i is used to detect contact with respect to equation 3.69.

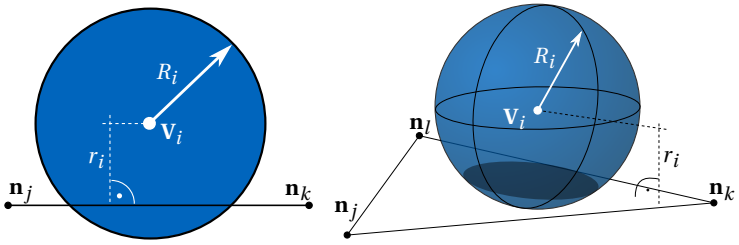

(a) Contact between a sphere and an edge.

(b) Contact between a sphere and a surface.

Figure 3.16: Contact including edges and surfaces.

* Detailed descriptions can be found in [98, 99].

The Double Hierarchy

It is not always clear which of the four preceding contact cases are to be considered. A sphere can be in contact with a vertex, a line, and a surface at the same time. To handle this problem efficiently, [99] introduces the Double Hierarchy method, containing a contact type hierarchy and a distance type hierarchy. A top-down approach is introduced with the following steps for the contact type check:

1. Check for contact with surface.
2. Perform an inside-outside test with the finite elements which discretize the surface.
3. Check for contact with the edges of the intersected finite element.
4. Check for contact with the vertices of the intersected finite element.
5. Based on the preceding operations: Decide if contact is found and with which geometric entity the sphere intersects.

Subsequently, the distance type hierarchy takes into consideration every newly found contact by the contact type check and compares its characteristic distance to the center of the sphere with all previously found contact types. Based on an efficient distance hierarchy check, introduced in [99], all valid contacts are finally found and used in the subsequent force evaluation.

3.3.3 Evaluation of Forces

The exact calculation of the contact forces in the DEM requires many geometric operations and depends on the contact force model used. A detailed discussion of the contact force calculation is postponed to Appendix F due to its length.

It is important to mention that a Hertz Mindlin Spring Dashpot Model (HM+D) [31] is used in this work. While the HM+D was developed for perfectly spherical and rigid particles, it is able to prevent complete penetration of the particle and its contacting partner with a penalty approach. As the discrete particles are simplified to rigid spheres no internal elasticity or energy dissipation (deformation of the impacting object) is implicitly considered. The viscous damping part of the HM+D model additionally enables modeling of the damping effects and loss of energy at the contact point. If not only the complete penetration should be prevented but the actual correct contact force is of interest the material parameters need to be calibrated. While contact force models such as Linear Spring Dashpot Model (LS+D) [108] or Plastic Dissipation Model (PLS(B)) [120] are also conceivable, the HM+D offers the best compromise between accuracy and simplicity of implementation.

Remark: Interpretation of DEM Parameters

In the following chapters, it will become apparent that many material parameters of the particles have to be tuned and vary from case to case. In this context, the naming of material parameters such as Young's Modulus often pretends a physical reference. As with other penalty-based methods, the penalty factor for the contact force calculation in the DEM is not always apparent in advance and is calculated from values such as Young's Modulus and the coefficient of restitution of the particles. A detailed description of the contact force calculation is given in Appendix F.

After the calculation of the contact forces, all interacting forces are assembled to derive the forces and torques on each particle or boundary element i [98, 99]:

$$\mathbf{F}_i = \mathbf{F}_{ext,i} + \mathbf{F}_{d,i} + \sum_j^n \mathbf{F}_{ij}, \tag{3.70}$$

$$\mathbf{T}_i = \mathbf{T}_{ext,i} + \mathbf{T}_{d,i} + \sum_j^n \left(\mathbf{r}_c^{ij} \times \mathbf{F}_{ij} \right). \tag{3.71}$$

Table 3.5 explains the symbols which are used in equations 3.70 and 3.71.

Symbol	Explanation
i	Particle or boundary element.
n, j	Total number n of contact partners j.
$\mathbf{F}$,$\mathbf{T}$	Sum of all forces, torques on object i.
$\mathbf{F}_{\text{ext}}$, $\mathbf{T}_{\text{ext}}$	External forces, such as gravity loads.
$\mathbf{F}_d$, $\mathbf{T}_d$	External damping forces.
$\mathbf{r}_c^{ij}$	Vector connecting the particle center and the contact point.
$\mathbf{F}_{ij} = F_n \mathbf{n}_c^{ij} + F_t \mathbf{t}_c^{ij}$	Interaction contact force between contact partners i, j.
F_n, F_t	Contact force in normal and tangential direction.
$\mathbf{n}_c^{ij}$, $\mathbf{t}_c^{ij}$	Normal and tangential unit vector at contact point.

Table 3.5: Symbols in equations 3.70 and 3.71, adapted from [98, 106]. More information is available in the Appendix F.

After the successful calculation of all contact forces the DEM proceeds to the integration of motion.

3.3.4 Time Integration

The DEM applies an explicit time integration scheme which efficiently advances in time. Various different methods are available with increasing accuracy. Generally the forces and torques are calculated with respect to masses m and inertia tensors $\mathbf{I}$ [63, 80],

$$\mathbf{F} = m\ddot{\mathbf{u}}, \tag{3.72}$$

$$\mathbf{T} = \mathbf{I}\dot{\boldsymbol{\omega}} + \dot{\boldsymbol{\omega}} \times (\mathbf{I}\dot{\boldsymbol{\omega}}). \tag{3.73}$$

While $\ddot{\mathbf{u}}$ describes the translational acceleration, $\dot{\boldsymbol{\omega}}$ and $\ddot{\boldsymbol{\omega}}$ refer to the rotational velocity and acceleration. Naturally, all tensors represent discrete values in the DEM.

3.3.4.1 Translational Velocity

The force calculation in equation 3.72 is independent of the reference frame* and thus the translational motion can be efficiently integrated with the velocity verlet (central difference) scheme, which is explained in Appendix E.1. The same scheme is used in this work to integrate the translational motion of the structural elements.

3.3.4.2 Rotational Velocity

In contrast to the force calculation, the torque calculation in equation 3.73 relies on the inertia tensor $\mathbf{I}$, which is highly dependent on the choice of reference frame [63].
The general equation for the inertia tensor can be calculated via Steiner's theorem†: Following equation 3.74, with the identity matrix $\mathbb{I}$ and the distance vector $\mathbf{r}$ connecting an arbitrary material point with the origin of the chosen reference frame.

$$\mathbf{I} = \int \mathrm{tr}\left(\mathbf{r}^T\mathbf{r}\right)\mathbb{I} - \mathbf{r}\mathbf{r}^T \, dm. \tag{3.74}$$

If $\mathbf{I}$ in equation 3.74 is evaluated with respect to the principal axes of inertia [63, 84] it results in a diagonal matrix. Then, the diagonal entries describe the eigenvalues of $\mathbf{I}$ [80]. In this case $\mathbf{r}$ connects an arbitrary material point with the object's barycenter.

Spherical Elements

Following [63], equation 3.73 can be simplified for a perfect sphere with a completely symmetric shape, due to the independence of the reference frame,

$$\mathbf{T} = \mathbf{I}\dot{\boldsymbol{\omega}} + \cancel{\dot{\boldsymbol{\omega}} \times (\mathbf{I}\boldsymbol{\omega})} = \mathbf{I}\dot{\boldsymbol{\omega}} = \frac{2}{5} m R^2 \dot{\boldsymbol{\omega}}. \tag{3.75}$$

* Assume a constant mass density ρ: The mass m is independent of the reference frame.
† Also called: Parallel axis theorem or Huygens–Steiner theorem.

The constant inertia tensor **I** allows the use of the same velocity verlet time integration scheme as for the translational motion. In the algorithm, given in appendix E.1, the translational terms need to be replaced with rotational terms to be applicable for the integration of the rotational motion of spherical elements.

Non-Spherical Elements

For non-spherical geometries, as they will be applied when working with clusters of spheres, the inertia tensor **I** is not constant anymore and a more detailed analysis is needed. For simplicity the inertia tensor **I** is typically evaluated in a body-fixed element reference frame. As a result, **I** is a diagonal matrix and relates the torques to the rotations in the body-fixed frame. To enable a time integration of motion on the global level, multiple steps need to be performed which are nicely described in [63]:

1. Calculate the diagonal matrix **I** in the body-fixed element reference frame.
2. Transform the global assembled torques **T** in the body-fixed element reference frame.
3. Calculate the local rotational accelerations with equation 3.73.
4. Transform the local rotational accelerations from the body-fixed element reference frame to the global reference frame.
5. Apply the velocity verlet scheme and update the rotations and rotational velocities.

3.3.5 Clusters

In contrast to preceding works, such as [37, 83, 117], the rocks will be modeled with the help of sphere clusters* instead of standard finite element discretized objects. With regard to the application to rocks, the disadvantageous modeling of smooth surfaces with clusters can be neglected. As stated in [80], this approach results in reduced computational time to calculate overlaps and thus to detect contact. The simple geometry of spheres allows the use of less complex mathematical operations compared to other geometric entities, like lines, edges, and surfaces [88, 112]. The more spheres are used to build the cluster, the smaller this advantage.
Section 5.1.1 investigates the influence of the number of spheres on the computational time in Figure 5.17. A detailed discussion and the first mention of sphere clusters in DEM can be found in [68].

* [80] calls it *connected spheres* or *multi-spheres*.

Various ways to create clusters are available while only one of them is demonstrated in the following, as it is important to properly calculate the object's moment of inertia $\mathbf{I}$ and its mass m.

1. Create a Computer-Aided Design (CAD) model of the desired shape as demonstrated in Figure 3.17a.
2. Create a tetrahedral volume mesh of the CAD model, see Figure 3.17b.
3. Calculate the total mass m of the object and the moment of inertia tensor $\mathbf{I}$ via equation 3.74.
4. Use the algorithm, described in [17, 18], to create any desired level of sphere cluster refinement of the provided CAD model, see Figure 3.17c. The corresponding online tool-kit can be obtained from [16].

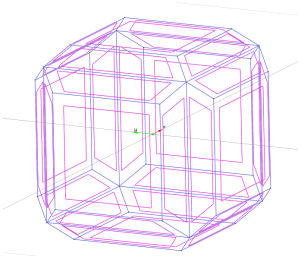

(a) CAD model of the desired shaped.

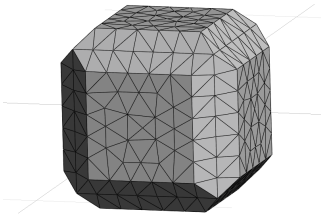

(b) Tetrahedral discretization of the CAD model, used to calculate inertia and mass.

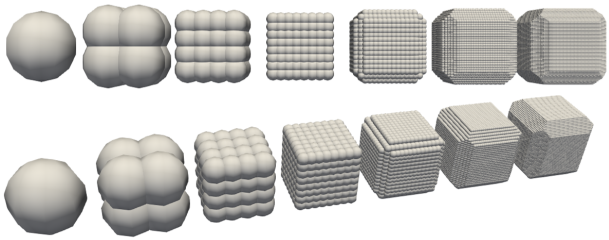

(c) Cluster refinements, adapted from [104].

Figure 3.17: Cluster: From CAD model to a variety of different cluster refinements. The clusters are finally used in the simulation to efficiently detect contact.

3.3.6 A Brief Note On Chaos

Chaos always occurs when slight deviations from initial values lead to strongly differing results. Examples for such chaotic systems are a double pendulum, or the course of a pinball [12]. Especially in non-linear systems, minor changes in the initial conditions can lead to very different results. Significantly the given boundary conditions influence the course and can characterize chaotic systems. An example of this is sharp edges in a DEM simulation. One way to classify these systems is to investigate their stability [80]. A system is said to be stable if it does not change too much when the initial values are changed [80]. In the following chapters about the simulation of rockfall protection systems, the input values, like impact location, impact velocity, and many more, are constantly varied to exclude a chaotic system behavior. The rockfall protection simulations benefit from the low number of particles in the system. A high number of particles and as a result a high number of possible contact scenarios increases the non-linearity of the system and thus directly the potential chaotic behavior. The very short impact times of less than one second also lead to disregarding the so-called butterfly effect. Eventually, the simulations in this work were repeated several times with the same settings to exclude chaotic influences of numerical instabilities.

CHAPTER 4

Staggered Coupling of DEM and FEM

This chapter represents the core of this dissertation. In order to combine different numerical computational methods in a partitioned simulation environment, the interface equation has to be defined first, and suitable coupling algorithms have to be developed. Intending to couple the DEM and the FEM, the interface equation is first presented in the following, and afterwards different coupling algorithms are discussed. Special features of DEM and FEM coupling are discussed, and the presented weak and strong coupling are introduced. Finally, several small test examples and benchmark tests are calculated to show the correctness of the coupling. All necessary steps for the partitioned coupling of the two numerical methods are described in detail, and algorithms are explicitly given. Finally, the transfer of data, i.e. the mapping, and special features of the DEM-FEM coupling are discussed.
The results of this section were published by the author in [106] and are discussed and reproduced below in the context of this dissertation. Some parts of the following text passages are copied directly from [106] and are therefore to be interpreted as quotations.*

4.1 Structure-Particle Equilibrium

To put the two independent physics, the DEM and the FEM, into an equilibrium state, the following force equilibrium at the structure needs to be achieved:

$$\begin{aligned} &\mathbf{F}_C\left(\mathbf{u}^{\Omega_{S,\Gamma_c}}(t),\dot{\mathbf{u}}^{\Omega_{S,\Gamma_c}}(t),\mathbf{u}^{P}(t),\dot{\mathbf{u}}^{P}(t)\right)\\ &-\mathbf{F}_{\text{int}}^{\Omega_{S,\Gamma_c}}\left(\mathbf{u}^{\Omega_S}(t),\dot{\mathbf{u}}^{\Omega_S}(t),\ddot{\mathbf{u}}^{\Omega_S}(t)\right)=0. \end{aligned} \tag{4.1}$$

Ω_S represents the structural domain, while Γ_c of Ω_S includes all nodes laying on the coupling interface. P describes the DEM particles. With respect to equation 4.1, the contact forces $\mathbf{F}_C$ of the particles, which are dependent on their

* Whose main author and copyright owner is the author of this dissertation.

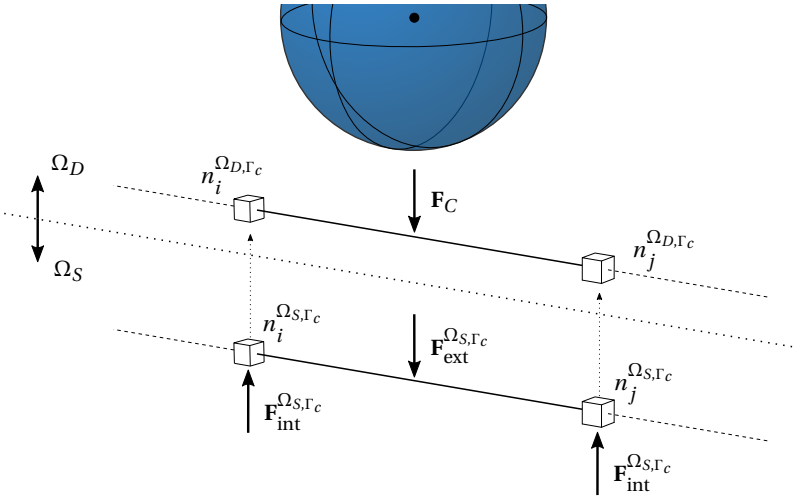

Figure 4.1: Domain definition and force equilibrium in DEM and FEM simulation [106].

displacements and velocities, need to be in equilibrium with the internal forces $\mathbf{F}_{\text{int}}^{\Omega_{S,\Gamma_c}}$ of the structure. The equilibrium of both, DEM and FEM simulation is graphically depicted in Figure 4.1.

The basic idea of the proposed partitioned coupling simulation is the interchange of primary (such as the displacement) and secondary (e.g., forces) interface variables which are obtained as the solution of the respective components of the simulation.

4.2 Interface Equations

In the following, the DEM problem is solved independently from the structural problem. To do so, the displacements and velocities of the structure at the given time step are transferred to the DEM model and this structure is further seen as the DEM wall, described by the domain Ω_D. It is used to calculate contact forces with the DEM particles P, which depend on their displacements and velocities (see Appendix F for contact laws and force calculations). After solving the DEM problem, the resulting contact forces are transferred to the structural analysis problem. With the contact forces, seen as external forces, the dynamic structural problem is solved, resulting in new displacements and velocities on the domain Ω_S. This procedure is outlined in Figure 4.2.

Following this, the contact forces $\mathbf{F}_C$ are now dependent on the displacements and velocities of Ω_D and not directly of Ω_S and are defined as the external forces coming from the DEM:

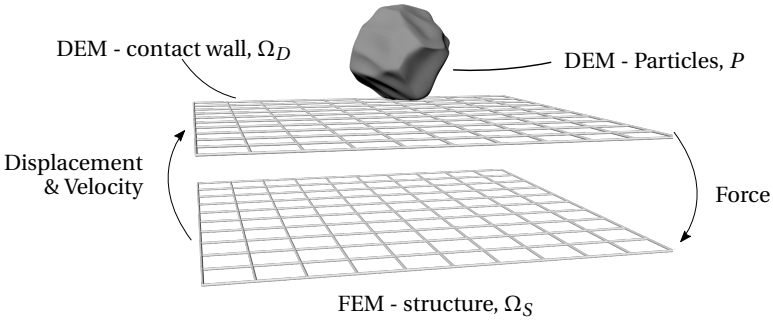

Figure 4.2: Transfer of force, displacement, and velocity between different applications [106].

$$\mathbf{F}_{\text{ext}}^{\Omega_{S,\Gamma_c}} = \mathbf{F}_C\left(\mathbf{u}^{\Omega_{D,\Gamma_c}}(t), \dot{\mathbf{u}}^{\Omega_{D,\Gamma_c}}(t), \mathbf{u}^{P}(t), \dot{\mathbf{u}}^{P}(t)\right) \tag{4.2}$$

The equilibrium within the structural mechanics problem is given as following:

$$\mathbf{F}_{\text{ext}}^{\Omega_{S,\Gamma_c}} - \mathbf{F}_{\text{int}}^{\Omega_{S,\Gamma_c}}\left(\mathbf{u}^{\Omega_S}(t), \dot{\mathbf{u}}^{\Omega_S}(t), \ddot{\mathbf{u}}^{\Omega_S}(t)\right) = 0. \tag{4.3}$$

After solving both domains, the two interface conditions, for the displacements and the velocities between both fields, are not fulfilled anymore:

$$\mathbf{u}^{\Omega_{D,\Gamma_c}}(t) - \mathbf{u}^{\Omega_{S,\Gamma_c}}(t) = 0, \tag{4.4}$$

$$\dot{\mathbf{u}}^{\Omega_{D,\Gamma_c}}(t) - \dot{\mathbf{u}}^{\Omega_{S,\Gamma_c}}(t) = 0. \tag{4.5}$$

As a result, the contact forces $\mathbf{F}_C$ computed within Ω_D and the contact forces which would be computed within Ω_S are not the same anymore, and thus, the equilibrium expression is not fulfilled:

$$\begin{aligned} &\mathbf{F}_C\left(\mathbf{u}^{\Omega_{D,\Gamma_c}}(t), \dot{\mathbf{u}}^{\Omega_{D,\Gamma_c}}(t), \mathbf{u}^{P}(t), \dot{\mathbf{u}}^{P}(t)\right) \\ -&\mathbf{F}_C\left(\mathbf{u}^{\Omega_{S,\Gamma_c}}(t), \dot{\mathbf{u}}^{\Omega_{S,\Gamma_c}}(t), \mathbf{u}^{P}(t), \dot{\mathbf{u}}^{P}(t)\right) = 0. \end{aligned} \tag{4.6}$$

Remark: Small Time Steps

For small time steps, resulting in smaller initial penetration, the tracking of the interface equilibrium can be negligible. However, the resulting difference will lead to inaccuracies for ill-conditioned systems and large time steps and make the solution unstable. To solve this problem, a possible approach is presented in section 4.5.

4.3 Mapping

In the previous chapters, the term "mapping" was coined in the context of exchanging data. Generally speaking, it is the data exchange at the interface between arbitrarily different discretization of the same domain and is an independent research topic discussed, for example, in [19, 121]. The partitioned coupling method of two simulation participants makes it necessary to exchange the data at the interface. A mapper is used to transfer the data from one domain to another. [121] offers a detailed discussion about mappers and mapping algorithms.

Concerning equation 4.4, the displacements at the interface of the two domains must be equal. If the structure is taken as the sending domain of the displacements, the discrete displacements on the DEM wall domain $\hat{\mathbf{u}}^{\Omega_{D,\Gamma_c}}$ can be expressed as follows employing a mapping matrix $\mathbf{H}_{df}$,

$$\hat{\mathbf{u}}^{\Omega_{D,\Gamma_c}} = \mathbf{H}_{df}\hat{\mathbf{u}}^{\Omega_{S,\Gamma_c}}. \tag{4.7}$$

The exchange of discrete nodal forces again uses a different mapping matrix $\mathbf{H}_{fd}$,

$$\hat{\mathbf{F}}_{\text{ext}}^{\Omega_{S,\Gamma_c}} = \mathbf{H}_{fd}\hat{\mathbf{F}}_C. \tag{4.8}$$

Conservation of Energy at the Interface

Especially when exchanging the forces, the conservation of energy at the interface has to be considered. This results in the following mathematical condition,

$$\hat{\mathbf{u}}^{\Omega_{D,\Gamma_c}\,T}\hat{\mathbf{F}}_C = \hat{\mathbf{u}}^{\Omega_{S,\Gamma_c}\,T}\hat{\mathbf{F}}_{\text{ext}}^{\Omega_{S,\Gamma_c}}. \tag{4.9}$$

Equations 4.7 and 4.9 finally result in the energy-conserving mapping matrix for interface forces,

$$\hat{\mathbf{F}}_{\text{ext}}^{\Omega_{S,\Gamma_c}} = \mathbf{H}_{df}{}^{T}\hat{\mathbf{F}}_C. \tag{4.10}$$

If the forces are exchanged by equation 4.8, it is called a consistent or direct mapping. On the other hand, a conservative mapping uses equation 4.10 for the exchange of forces. With the conservative mapping, the force mapping matrix does not need to be recalculated and instead is simply the transposed displacement mapping matrix.

Mapping Algorithms

Various different mapping algorithms exist of which two are shortly discussed in the following. Figure 4.3 represents a visualization of the respective algorithms.

- The *nearest neighbor* mapping, in Figure 4.3a, finds the nearest nodes on the partner domain and directly exchanges data. The mapping matrices consist only of 0 and 1. The figure also illustrates why the results of the nearest neighbor algorithm often oscillate for highly differing meshes. It is visible that some nodes do not receive any force. Especially when the source domain is more coarsely refined than the target domain. Even though the algorithm performs poorly for very different meshes, it is very efficient and beneficial for conforming meshes.
- The *nearest element* mapping algorithm, on the other hand, finds the next element on the partner domain by projecting the position of the current node onto the partner domain. Using the element shape functions, the values are then extrapolated to the adjacent discrete nodes. Figure 4.3b illustrates this behavior.

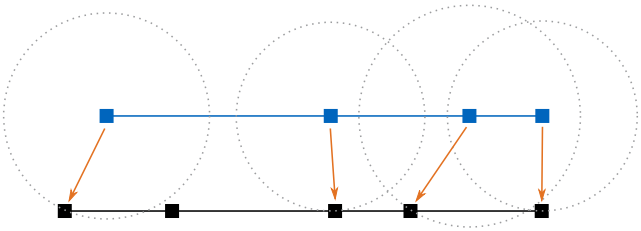

(a) Nearest neighbor.

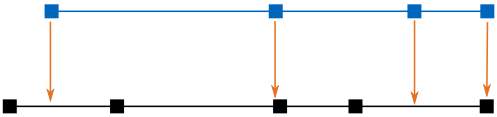

(b) Nearest element.

Figure 4.3: Nearest neighbor and nearest element mapping algorithms. The blue domain represents the origin and the black domain is the mapping destination.

Remark: Conforming Meshes

The simulations in this dissertation are performed with matching discretization of the two simulation participants. This simplifies the complicated topic of mapping to the direct data exchange of overlaying nodes.

Mesh Dependency

For the specific application of highly flexible cable structures in this study, such as rockfall protection nets or any other kind of cable-like structures, the DEM wall condition Ω_D discretization and the FEM Ω_S discretization on Γ_c must exactly coincide (conforming meshes). The respective meshes represent a physical mesh that must be correctly described to model the exact contact positions. To demonstrate this behavior, Figure 4.4a visualizes the DEM part of the simulation. A cable net is modeled and impacted by two spheres. A large sphere finds contact and deforms the boundary while a smaller sphere penetrates an opening. In addition, Figure 4.4b represents the respective FEM structure which is used to calculate the adequate structural response.

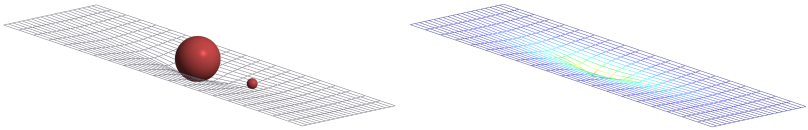

(a) Discretized Ω_D. (b) Discretized Ω_S.

Figure 4.4: Modeling of impact with cable structured boundaries [106]. See Figure 4.5 for the total simulation results.

If surface elements such as shells or membranes, which do not possess physically predetermined discrete contact positions, are used within a coupled simulation, arbitrary meshes can be used. In that case, a mapper [19, 121] will be responsible for the correct data transfer. Figure 4.5 shows the time course of a coupled simulation in which a tiny particle penetrates the mesh without finding contact while a large one is intercepted. This is also possible if the structure is modeled with homogenized surface elements since it is sufficient if the DEM wall represents the actual contact nodes. Figure 4.6 illustrates this behavior.

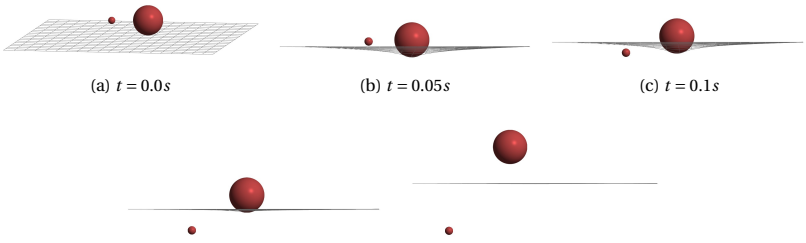

(a) $t = 0.0s$ (b) $t = 0.05s$ (c) $t = 0.1s$

(d) $t = 0.15s$ (e) $t = 0.2s$

Figure 4.5: A small particle is penetrating and falling through the coarse cable net. A big particle collides with cable structure and is stopped and thrown back by the protection structure [106].

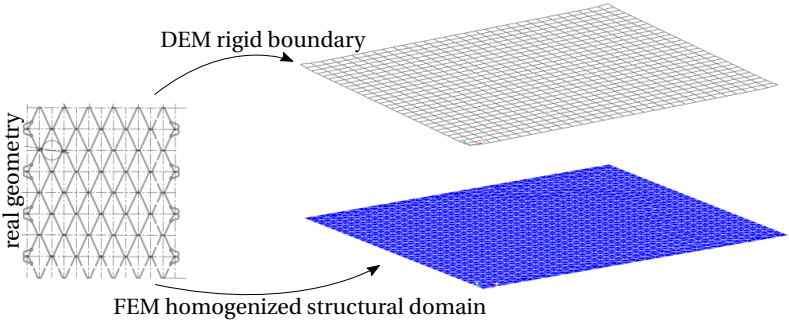

(a) A DEM Wall with physically correct contact nodes and a simplified structural model is created from the actual geometry.

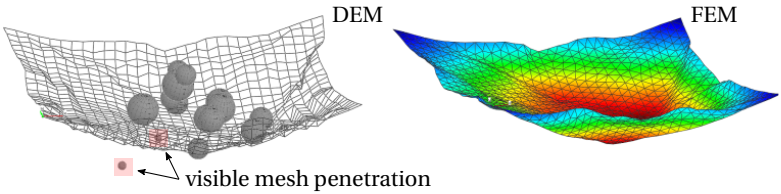

(b) Thus, despite the simplified homogeneous structure model, the penetration of small particles can be modeled.

Figure 4.6: Instead of discretizing both the DEM wall and the structure with individual cable elements, it is advisable to represent the structure as a homogenized surface structure. Furthermore, the presented coupling method allows the model of the two interface parts independently thanks to its partitioning. Thus, per DEM wall, all physically correct contact points can be modeled while a simplified structural model can be used. The figures are adapted from [102].

4.4 Staggered Weak Coupling

The fundamental idea of the weak coupling* follows a single exchange of coupling data in each time step. The communication pattern is depicted in Figure 4.7 while the essential steps at each time, including this communication pattern, can be summarized as follows:

1. Solve DEM (results: $\mathbf{u}^P, \dot{\mathbf{u}}^P, \mathbf{F}_C$).
2. Map† *Contact Forces* from DEM to Structure.
3. Solve Structure (results: $\mathbf{u}^{\Omega_S}, \dot{\mathbf{u}}^{\Omega_S}, \ddot{\mathbf{u}}^{\Omega_S}$).
4. Map *Displacement* and *Velocity* from Structure to DEM.
5. Advance in time.

The interface variables are accordingly updated and mapped (see steps **2.** and **4.**):

$$\text{Displacements:} \qquad {}^{k+1}\mathbf{u}^{\Omega_{D,\Gamma_c}} \overset{\text{map}}{=} {}^{k}\mathbf{u}^{\Omega_{S,\Gamma_c}}, \tag{4.11}$$

$$\text{Velocities:} \qquad {}^{k+1}\dot{\mathbf{u}}^{\Omega_{D,\Gamma_c}} \overset{\text{map}}{=} {}^{k}\dot{\mathbf{u}}^{\Omega_{S,\Gamma_c}}, \tag{4.12}$$

$$\text{Contact forces:} \qquad {}^{k+1}\mathbf{F}_{\text{ext}}^{\Omega_{S,\Gamma_c}} \overset{\text{map}}{=} {}^{k}\mathbf{F}_C. \tag{4.13}$$

This algorithm is comparatively easy to implement and typically does not require deep interaction. Standard DEM and FEM simulation environments provide the exchange data as an output. Therefore, different software can also be efficiently applied here. Furthermore, it is shown that the algorithm can be applied if the time steps do not become too large (see examples in sections 4.6.2 and 4.6.3). However, the behavior of this procedure can become unstable as soon as the differences in stiffness, mass, and velocity between the two physics become very high. The procedure is then very prone to the time step size used. Yet, decreasing the time step size will usually lead to inefficient and numerically costly simulations.

* Sometimes also called explicit coupling [131].
† See section 4.3 for a discussion of the mapping.

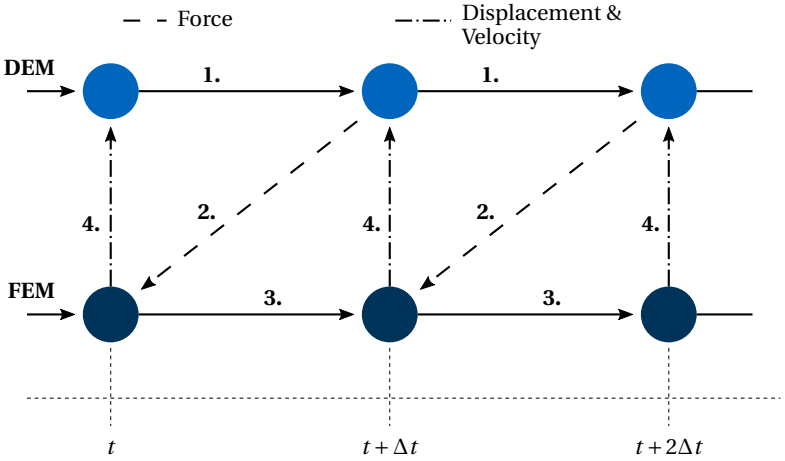

Figure 4.7: Staggered weak coupling procedure between DEM and FEM [106].

To gain a deeper understanding of the underlying procedure, this approach is further detailed in the following Algorithm 2.

Algorithm 2 Weak Coupling

```
1:  Initialize
2:  while t ≤ t_end do
3:      if particle_near_wall then
4:          use pre-defined time step
5:      else
6:          use increased time step
7:      Search nearest neighbors and find contact                ▷ Sec. 3.3.2
8:      Calculate F_C                                            ▷ Eq. F.5
9:      Time integration of DEM part                             ▷ Sec. 3.3.4
10:     Map* F_C on Γ_c from Ω_D to Ω_S                          ▷ Eq. 4.10
11:     if forces ≠ 0.0 then
12:         Solve structure (FEM)
13:         Map u, u̇ on Γ_c from Ω_S to Ω_D                      ▷ Eq. 4.7
14:         Update position of Ω_D and Ω_S                       ▷ Eq. 3.1
15:     t = t + Δt
16: Finalize
```

In this procedure, two additional features will be discussed. They are independent of the coupling approach but improve the performance significantly. They are added within Algorithm 2 and highlighted in the following:

particle_near_wall (line 3 - 6) – Checks if the individual particles are in the vicinity of the structural model to adjust the time step. A particle moving

freely in space can be simulated with a time step larger than it would be required for the simulation of the DEM-FEM interaction.

$forces \neq 0.0$ (line 11 - 14) – Is an additional check, which is used only to solve the structure when contact forces are present. This is only valid if the self-weight of the structure or any other loads (except impact loads) are neglected. Otherwise, a preliminary simulation or a form-finding (see e.g. [38, 131]) of the structure is needed.

4.5 Staggered Strong Coupling

As known from other coupled multi-physics problems, such as Fluid-Structure Interaction (FSI) [129, 130, 131], the direct, explicit transfer of the interface data (forces, velocities, displacements) can lead to divergence problems in the staggered simulation. Large contact forces will cause problems due to differences in velocities, acceleration, and highly different masses on both sides. In contrast to the weak coupling approach, the strong coupling* adds an additional iteration loop in each time step, which solves for the equilibrium between both numerical physics. This requires a Gauss-Seidel loop between DEM and FEM, which might need to be solved multiple times within one time step [44, 45, 73, 110, 131]. This strategy enforces the coupling conditions (equations 4.4 - 4.6) to be fulfilled. While the convergence is considered to be achieved as soon as the interface residual is below a user-defined tolerance ϵ, the residual formulation is defined by equation 4.14.

The steps of this approach are shown in Figure 4.8 and summarized in the following:

1. Solve DEM (results: $\mathbf{u}^P, \dot{\mathbf{u}}^P, \mathbf{F}_C$).

2. Map† *Contact Forces* from DEM to Structure.

3. Solve Structure (results: $\mathbf{u}^{\Omega_S}, \dot{\mathbf{u}}^{\Omega_S}, \ddot{\mathbf{u}}^{\Omega_S}$).

4. Map *Displacement* and *Velocity* from Structure to DEM.

5. Calculate interface residual (Equation 4.14).

6. Repeat steps 1-5 until the interface residual reaches a given tolerance.

7. Advance in time.

The weak coupling algorithm, described in the preceding section 4.4, expresses one single iteration in the strong coupling scheme (step **1.** - **4.**). The additional interface loop (step **6.**, being controlled by the breaking criteria in step **5.**) adds complexity to the solution procedure and significantly increases the computation costs as the system now needs to be solved multiple times within one time

* In the literature also called implicit coupling [131] or a conventional serial staggered approach within the context of loose coupling [44, 45, 110].

† See section 4.3 for a discussion of the mapping.

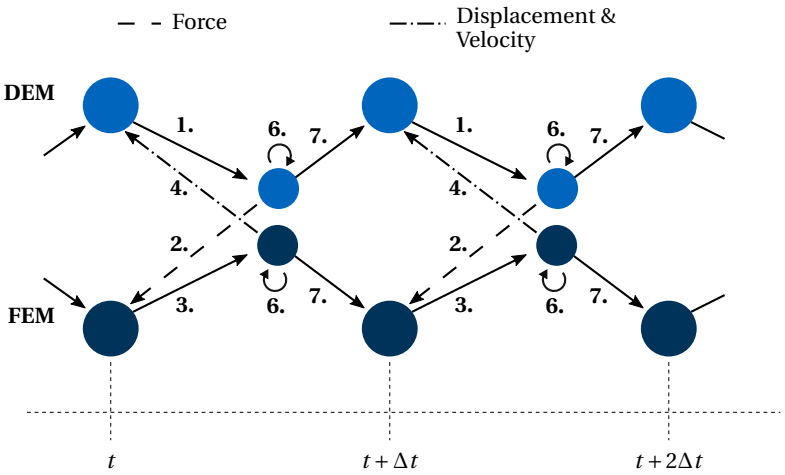

Figure 4.8: Strong coupling communication diagram [106].

step. However, it allows more accurate results and higher simulation stability. It can be noted that the number of solving iterations is typically still lower than if the time step would be reduced to a value where the weak coupling approach would still be applicable. This is primarily because many coupling iterations are typically not required throughout the entire simulation but only at specific time steps. The comparison of the two procedures, including a view on the performance, is outlined in section 4.6.

4.5.1 Interface Residual

The residual criteria within the strong coupling loop is defined by:

$$\epsilon \geq \frac{\| {}^{k}\boldsymbol{r} \|}{\sqrt{n_{\text{eq}}}}, \tag{4.14}$$

where ϵ is the user-defined breaking tolerance. It is checked after each iteration k by scaling the norm of the residuum ${}^{k}\boldsymbol{r}$ with the square root of the number of degrees of freedom n_{eq} at the interface Γ_c [74]. It is important to note that the interface tolerance should be larger than the convergence tolerances of the respective individual solvers within the coupled system. Otherwise, the convergence criteria cannot be reached. The residuum can either be obtained by the displacements, the velocities, or the contact forces. By subtracting the current discrete solutions on the boundary Γ_c from the previous discrete solutions of step $k-1$, the residuum of each variable is noted as follows:

$$\text{Displacement residuum:} \quad {}^{k}\boldsymbol{\mathcal{r}}_u = {}^{k}\hat{\mathbf{u}}^{\Omega_{S,\Gamma_c}} - {}^{k-1}\hat{\mathbf{u}}^{\Omega_{S,\Gamma_c}}, \tag{4.15}$$

$$\text{Velocity residuum:} \quad {}^{k}\boldsymbol{\mathcal{r}}_{\dot{u}} = {}^{k}\hat{\dot{\mathbf{u}}}^{\Omega_{S,\Gamma_c}} - {}^{k-1}\hat{\dot{\mathbf{u}}}^{\Omega_{S,\Gamma_c}}, \tag{4.16}$$

$$\text{Contact force residuum:} \quad {}^{k}\boldsymbol{\mathcal{r}}_F = {}^{k}\hat{\mathbf{F}}_C - {}^{k-1}\hat{\mathbf{F}}_C. \tag{4.17}$$

4.5.2 Convergence Acceleration via Relaxation

Furthermore, large time steps typically lead to large differences in the interface velocities and displacements, and thus the result can be non-physical large contact forces. If those forces are too high, small time steps can still lead to unstable simulations, even with the proposed strong coupling algorithm. As a remedy, the transferred data can be gradually applied, also called relaxation, permitting a faster interface convergence. The so-called *convergence acceleration* (see also [131]) can be achieved by numerous methods and is discussed in the following.

Two different strategies can be chosen for the relaxation: either the relaxation of the displacements and velocities or the relaxation of the contact forces. The relaxation is done with respect to the residual (equations 4.15 - 4.17), respectively:

$$\text{Relaxed displacements:} \quad {}^{k}\hat{\mathbf{u}}^{\Omega_{S,\Gamma_c}}_{\text{rel}} = {}^{k-1}\hat{\mathbf{u}}^{\Omega_{S,\Gamma_c}}_{\text{rel}} + {}^{k}\alpha_u\, {}^{k}\boldsymbol{\mathcal{r}}_u, \tag{4.18}$$

$$\text{Relaxed velocities:} \quad {}^{k}\hat{\dot{\mathbf{u}}}^{\Omega_{S,\Gamma_c}}_{\text{rel}} = {}^{k-1}\hat{\dot{\mathbf{u}}}^{\Omega_{S,\Gamma_c}}_{\text{rel}} + {}^{k}\alpha_{\dot{u}}\, {}^{k}\boldsymbol{\mathcal{r}}_{\dot{u}}, \tag{4.19}$$

$$\text{Relaxed contact forces:} \quad {}^{k}\hat{\mathbf{F}}_{C,rel} = {}^{k-1}\hat{\mathbf{F}}_{C,rel} + {}^{k}\alpha_F\, {}^{k}\boldsymbol{\mathcal{r}}_F. \tag{4.20}$$

Each variable is subsequently updated from the previous solution (step $k-1$) using the respective interface residuum scaled by relaxation factor α.
There are different approaches to obtain the scaling factor α (see also [110]). The relaxation factor can be set to a user-defined constant value, which is very simple and helps to improve the quality of the simulation. Another approach is to use the Aitken method* [1]. It optimizes α in every iteration with respect to the current residuum ${}^{k}\boldsymbol{\mathcal{r}}$ and the previous residuum ${}^{k-1}\boldsymbol{\mathcal{r}}$:

$${}^{k}\alpha(\boldsymbol{\mathcal{r}}) = -{}^{k-1}\alpha\, \frac{{}^{k-1}\boldsymbol{\mathcal{r}} \cdot \left({}^{k}\boldsymbol{\mathcal{r}} - {}^{k-1}\boldsymbol{\mathcal{r}}\right)}{\| {}^{k}\boldsymbol{\mathcal{r}} - {}^{k-1}\boldsymbol{\mathcal{r}} \|^2}, \tag{4.21}$$

respectively, $\alpha_u = \alpha(\boldsymbol{\mathcal{r}}_u)$, $\alpha_{\dot{u}} = \alpha(\boldsymbol{\mathcal{r}}_{\dot{u}})$, $\alpha_F = \alpha(\boldsymbol{\mathcal{r}}_F)$. The influence of the relaxation factor α is studied in the example in section 4.6.4.
In this study, either the displacement and the velocity field or the contact forces are independently relaxed and subsequently mapped. However, in the case of displacements and velocities, both residua have to be achieved to ensure that both solution fields still coincide on both sides. Thus, the resulting residua for both relaxing procedures are given as follows:

* Appendix D demonstrates the operation of the Aitken method by solving a scalar function.

$$\text{Displacement and velocity residuum:} \quad {}^{k}\boldsymbol{\varkappa} = \text{abs max}\left({}^{k}\boldsymbol{\varkappa}_{u}, {}^{k}\boldsymbol{\varkappa}_{\dot{u}}\right), \tag{4.22}$$

$$\text{Contact force residuum:} \quad {}^{k}\boldsymbol{\varkappa} = {}^{k}\boldsymbol{\varkappa}_{F}. \tag{4.23}$$

The interface variables are updated and mapped accordingly (see steps **2.** and **4.** in Figure 4.8). The following variables are exchanged within the interface:

Without relaxation:

$$\text{Displacements:} \quad {}^{k+1}\mathbf{u}^{\Omega_{D,\Gamma_c}} \overset{\text{map}}{=} {}^{k}\mathbf{u}^{\Omega_{S,\Gamma_c}}, \tag{4.24}$$

$$\text{Velocities:} \quad {}^{k+1}\dot{\mathbf{u}}^{\Omega_{D,\Gamma_c}} \overset{\text{map}}{=} {}^{k}\dot{\mathbf{u}}^{\Omega_{S,\Gamma_c}}, \tag{4.25}$$

$$\text{Contact forces:} \quad {}^{k+1}\mathbf{F}_{\text{ext}}^{\Omega_{S,\Gamma_c}} \overset{\text{map}}{=} {}^{k}\mathbf{F}_{C}. \tag{4.26}$$

With relaxation:

$$\text{Displacements:} \quad {}^{k+1}\mathbf{u}^{\Omega_{D,\Gamma_c}} \overset{\text{map}}{=} {}^{k}\mathbf{u}_{\text{rel}}^{\Omega_{S,\Gamma_c}}, \tag{4.27}$$

$$\text{Velocities:} \quad {}^{k+1}\dot{\mathbf{u}}^{\Omega_{D,\Gamma_c}} \overset{\text{map}}{=} {}^{k}\dot{\mathbf{u}}_{\text{rel}}^{\Omega_{S,\Gamma_c}}, \tag{4.28}$$

$$\text{Contact forces:} \quad {}^{k+1}\mathbf{F}_{\text{ext}}^{\Omega_{S,\Gamma_c}} \overset{\text{map}}{=} {}^{k}\mathbf{F}_{C,rel}. \tag{4.29}$$

In summary, both solution strategies are described within Algorithm 3 and Algorithm 4 in pseudo code.

Algorithm 3 Strong Coupling - Relaxed Displacement and Velocity

```
Initialize
while t ≤ t_end do
    while ε < ‖ᵏϰ‖/√n_eq do                                   ▷ Eq. 4.14
        Search nearest neighbors and find contact             ▷ Sec. 3.3.2
        Calculate ᵏF_C                                        ▷ Eq. F.5
        Time integration of DEM part                          ▷ Sec. 3.3.4
        Map* ᵏF_C on Γ_c from Ω_D to Ω_S                      ▷ Eq. 4.10
        Solve structure (FEM)
        Map ᵏu, ᵏu̇ on Γ_c from Ω_S to Ω_D                     ▷ Eq. 4.7
        Calculate ᵏϰ_u, ᵏϰ_u̇                                  ▷ Eq. 4.15, 4.16
        Relax ᵏu, ᵏu̇                                         ▷ Eq. 4.18, 4.19
        Update position of Ω_D                                ▷ Eq. 3.1
        Calculate ᵏϰ                                          ▷ Eq. 4.22
    Update position of Ω_S                                    ▷ Eq. 3.1
    t = t + Δt
Finalize
```

Algorithm 4 Strong Coupling - Relaxed Force

```
Initialize
while t ≤ t_end do
    while ε < ‖ᵏ𝓇‖/√n_eq do                                   ▷ Eq. 4.14
        Search nearest neighbors and find contact             ▷ Sec. 3.3.2
        Calculate ᵏF_C                                        ▷ Eq. F.5
        Time integration of DEM part                          ▷ Sec. 3.3.4
        Map ᵏF_C on Γ_c from Ω_D to Ω_S                       ▷ Eq. 4.10
        Calculate ᵏ𝓇_F                                        ▷ Eq. 4.17
        Relax ᵏF̂_C                                            ▷ Eq. 4.20
        Solve structure (FEM)
        Map ᵏu, ᵏu̇ on Γ_c from Ω_S to Ω_D                     ▷ Eq. 4.7
        Update position of Ω_D                                ▷ Eq. 3.1
        Calculate ᵏ𝓇                                          ▷ Eq. 4.23
    Update position of Ω_S                                    ▷ Eq. 3.1
    t = t + Δt
Finalize
```

Remark: The Coefficient of Restitution (COR)

Large contact forces will result in difficult fulfillment of interface conditions (Equations 4.4 - 4.6). Section 4.5 proposes a remedy for that problem. One major factor influencing the magnitude of the contact forces is the DEM particle property COR. This value must be defined by the user and heavily influences the stability of the coupled simulation (see example 4.6.5). The coefficient represents the ratio of initial velocity and final velocity after impact [80, 98] (see equation F.6), and is further discussed in Appendix F.1. Since this coefficient is determined manually for each simulation, it is essential to be careful when calibrating.

4.6 Systematic Assessment of the DEM-FEM Coupling

This section presents some examples that systematically analyze the difference between the introduced coupling approaches and their application within the simulation of relevant industrial applications. The examples show impacting objects on highly flexible lightweight cable structures, such as protection nets. These interaction problems typically have numerical stability issues within the simulations, as the net structures have a low mass, whereas the rocks are typically heavy. This instability leads to the problem that the forces might become very large, especially when the first impact occurs. Thus, due to the different masses, this may lead to convergence problems, especially if the chosen time step is large, leading to inaccuracies in the simulation.

- First, a benchmark test is calculated from [98]. In the test in subsection 4.6.1, a spherical particle impacts on a single-span beam and the resulting contact forces and displacements are compared.
- In the first academic problem in subsection 4.6.2, a cable structure is modeled to evaluate the influence of different time step values.
- Subsection 4.6.3 subsequently uses a cable structure with a large pre-stress while also showing the influence of the Coefficient of Restitution (COR) in order to analyze the influence of larger contact forces on the required time step.
- Subsection 4.6.3 investigates the difference between relaxing forces (see Algorithm 4) and relaxing displacements and velocities (see Algorithm 3).
- The proper choice of a relaxation factor is further discussed in the example of subsection 4.6.4.
- The influence of the COR, which scales the contact forces, is then analyzed in subsection 4.6.5.
- Subsection 4.6.6 investigates the conservation of energy in the coupled system with two different DEM parameter sets.
- Finally, a practical application of a rockfall into a cable net, using the herein explained approaches, is presented in subsection 4.6.7.

All examples apply a Hertz Mindlin Spring Dashpot Model (HM+D) law to calculate the DEM contact forces. A detailed description is given in Appendix F. Additionally, no structural self-weight is considered in this section, to fully concentrate on the coupling method.

4.6.1 Impact on a Single-Span Beam

A benchmark test is performed to verify the coupling algorithm in which a spherical particle impacts a single-span beam. As shown in Figure 4.9, the beam is hinged on the left and right and is discretized with 60 linear beam elements. Table 4.1 shows the input data for the simulation, and the simulation results are presented in Figure 4.10 and compared with [98]'s results. A time step Δt of $= 5e-8s$ is used to resolve the very short contact time of $\approx 0.16ms$. While the analytical solution is given in [82], it can be easily seen that the results match almost exactly.

	$\rho_0 \left[\frac{kg}{m^3}\right]$	$E \left[\frac{N}{m^2}\right]$	$\nu\,[-]$	$\varepsilon_n\,[-]$	$\mu_P\,[-]$	$\mathbf{g} \left[\frac{m}{s^2}\right]$
Particle	7960	2.1582e11	0.289	1.0	0	[0,0,0]
Structure	7960	2.1582e11	0.289	-	-	

Table 4.1: Simulation data, obtained from [98]. The dimensions of the structure and the particle are shown in Figure 4.9.

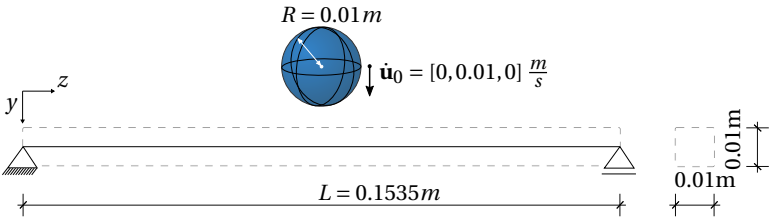

Figure 4.9: Sketch of the beam impact problem setup, adapted from [98]. The remaining simulation data is given in Table 4.1.

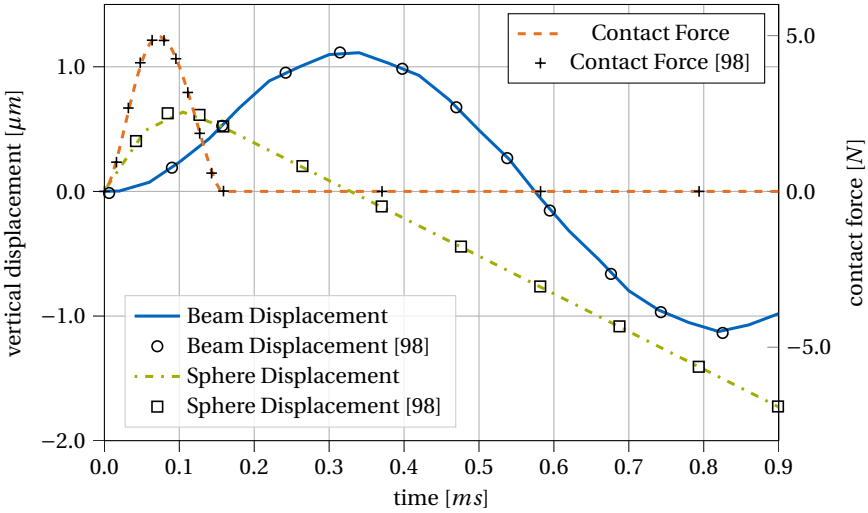

Figure 4.10: Visualization of displacement of impacting sphere, displacement of beam, and contact forces over time. For verification the data is compared to [98].

4.6.2 Impact on a Compliant Cable: Large Deformations

In this example, a single DEM particle with perfect spherical dimensions impacts a pre-stressed cable, which is discretized with three finite elements. Here, the contact point on the structure is known, and thus it can be focused on the performance of the coupling algorithms. The setup of this academic example can be found in Figure 4.11a. It demonstrates the necessity of a strong coupling algorithm since, for larger time steps, the phenomena of artificial contact loss due to large initial contact forces occur.

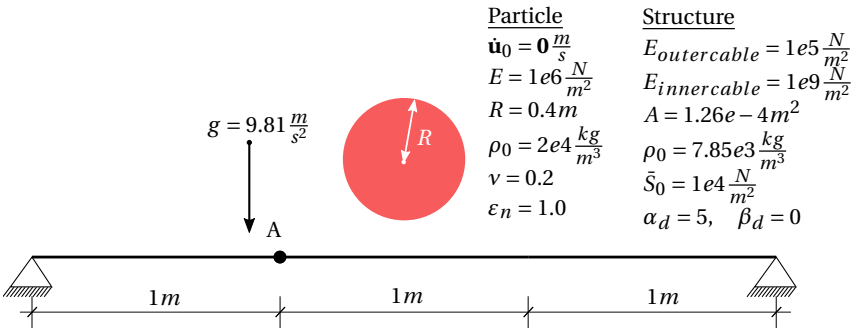

(a) Problem setup.

(b) Weak coupling after impact.

(c) Strong coupling after impact.

Figure 4.11: Problem setup, including all geometrical and physical input parameters for the simulation. Results after impact with time step of $\Delta t = 1e-2s$ [106].

Within empirical tests, the time step $\Delta t = 1e-3s$ is found to be the highest possible time step for which the weak coupling algorithm can resolve to an appropriate solution. Here, the coefficient of restitution (COR) is set to be 1.0. Implicit time integration is used for the structure, as the chosen time step is too large for an appropriate solution with an explicit time integration scheme. Figure 4.11b and 4.11c show the behavior of the cable after the first contact, for the time step size of $\Delta t = 1e-2s$. Using the weak coupling approach, a "jump" can be outlined as shown in Figure 4.11b. Due to the large time step, a greater indentation and higher velocities occur. Consequently, the interacting force is too large so that the sphere and cable do not continuously stay in contact during the entire time. This leads to nonphysical behavior of the coupled problem, as shown in Figure 4.12. By adding the additional interface loop to solve for the contact force, the convergence of the problem can be achieved for a larger time step of $\Delta t = 1e-2s$.

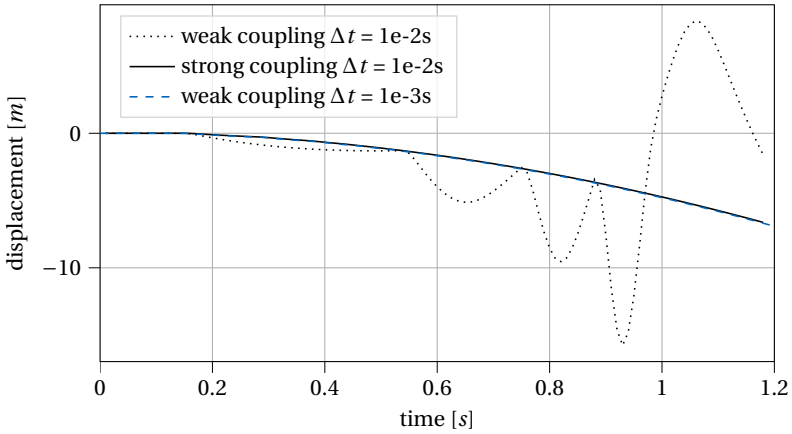

Figure 4.12: Comparison of weak coupling approach with $\Delta t = 1e-2s$ and $\Delta t = 1e-3s$ against the strong coupling approach with $\Delta t = 1e-2s$ for the vertical displacement of node A (see also Figure 4.11a) [106].

Interface Convergence

In the following, the time step of the first contact is discussed in detail. It can be seen (Figure 4.13d) that the contact force is relatively large in the first inner iteration (coming from the relatively large time step) and decreases within the interface iteration to a converged solution due to the application of the Aitken relaxation, introduced in equation 4.21. The large discrepancy in the contact force leads to an unstable coupled simulation when using a standard weak coupling algorithm. The same accounts for the deflections of the impacting sphere as shown in Figure 4.13c.
Figures 4.13a and 4.13b present a visual description of the interface condition in equation 4.4 and 4.5. It can be seen that the position of Ω_D and Ω_S do converge to a common value, to fulfill the interface displacement/velocity equilibrium.
Exemplarily, the total number of inner iterations for each time step are shown in Figure 4.14. It shows that the number of inner iterations can vary greatly (between one, if there is no contact, and nine iterations) within each time step. However, it can be noted that the number of contact simulations is still lower than if the time step would be decreased to $\Delta t = 1e-3s$, which is the limit for which the weak coupling approach still converges.

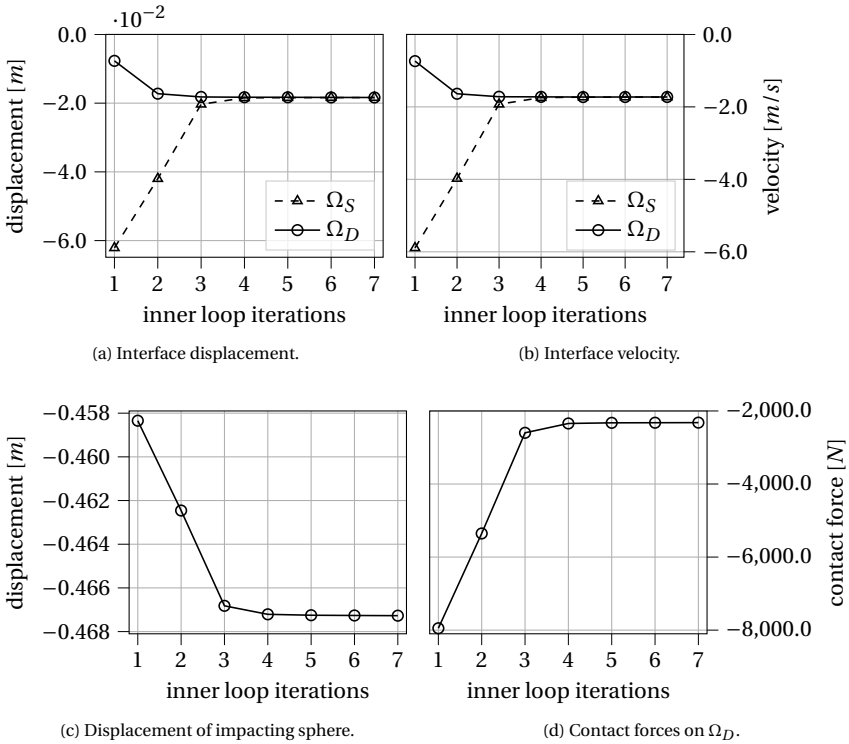

(a) Interface displacement.

(b) Interface velocity.

(c) Displacement of impacting sphere.

(d) Contact forces on Ω_D.

Figure 4.13: Simulation results within one time step over inner coupling iterations [106].

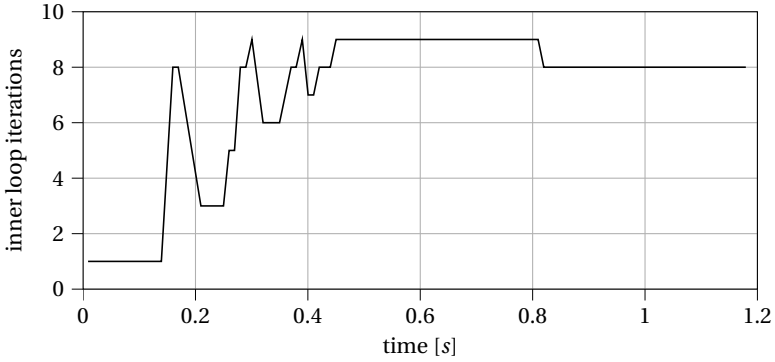

Figure 4.14: Number of interface iterations per time step, adapted from [106].

4.6.3 Comparison to Position of Rest With Different Time Steps

In this section a setup similar to the previous example (see subsection 4.6.2 and Figure 4.11a) with an increased pre-stress ($\bar{S}_0 = 1e6\frac{N}{m^2}$) and a homogeneous Young's Modulus ($E = 1e9\frac{N}{m^2}$) in the cable structure is used with the following changes for the impacting sphere: $R = 0.12m$ and $\rho_0 = 3.5e4\frac{kg}{m^3}$.

The result of the transient analysis will be compared to the static solution, considering the particle weight as an external static force F_m.

$$F_m = \overbrace{\underbrace{\frac{4}{3}\pi R^3_{\text{sphere}}}_{V_{\text{sphere}}} \cdot \rho_{\text{sphere}}}^{m_{\text{sphere}}} \cdot \underbrace{9.81\frac{m}{s^2}}_{\text{gravity}}. \tag{4.30}$$

The resulting static deflection of node A (see Figure 4.11a) is shown in Figure 4.15. This comparison proves that the transient analysis approaches the static solution after a certain time.

Furthermore, the sensitivity of the time step within each coupling algorithm is also studied in this example. The results of all solutions are presented and compared in Figure 4.15. It shows that the weak coupling approach provides an accurate performance for a time step of $\Delta t = 1e-3s$, whereas the solution for $\Delta t = 1e-2s$ is very unstable. It turns out that the result oscillates around the expected solutions for large time steps.

Finally, the measured solutions for time steps of $\Delta t = 1e{-}2s$ and $\Delta t = 3e{-}2s$ show that the strong coupling algorithm still allows for good convergence for rather large time steps. However, by increasing the time steps, the number of interface iterations subsequently increases, which is shown in Figures 4.16 and 4.17. Especially when the impact occurs, the large difference in interface velocities leads to an increased number of interface iterations (see Figure 4.16). The proposed algorithm decreases this difference within the scope of coupled simulations, leading to a smaller number of iterations.

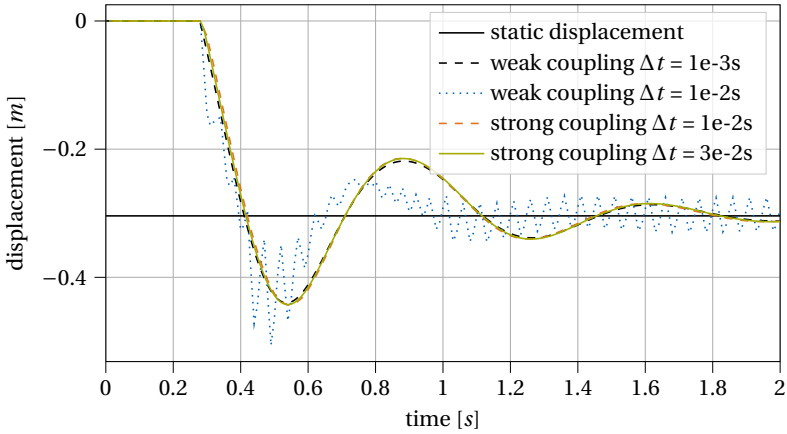

Figure 4.15: Comparison of weak coupling approach with $\Delta t = 1e-2s$ and $\Delta t = 1e-3s$ against the strong coupling approach with $\Delta t = 1e-2s$ and $\Delta t = 3e-2s$ for the vertical displacements of node A (see also Figure 4.11a). Furthermore, the static solution of the problem is provided to show which value the results should approach [106].

Relaxation Variants

The influence if either displacements and velocities or forces are relaxed is examined in the following. Both options are described in Algorithm 3 and Algorithm 4, respectively. Comparing Figures 4.17 and 4.16, it can be noted that relaxing the forces facilitates slightly faster convergence than relaxing displacements and velocities.
In this specific case at hand, clear and marked-off points of load application (impact position) do exist. However, in different cases, such as in the following subsection 4.6.7, where a variety of possible impact nodes exist, relaxing displacements and velocities are shown to be the better choice. In those cases, which appear more frequently, the impacting spheres can rapidly change the impacting position and thus lead to a slow converging force residual.

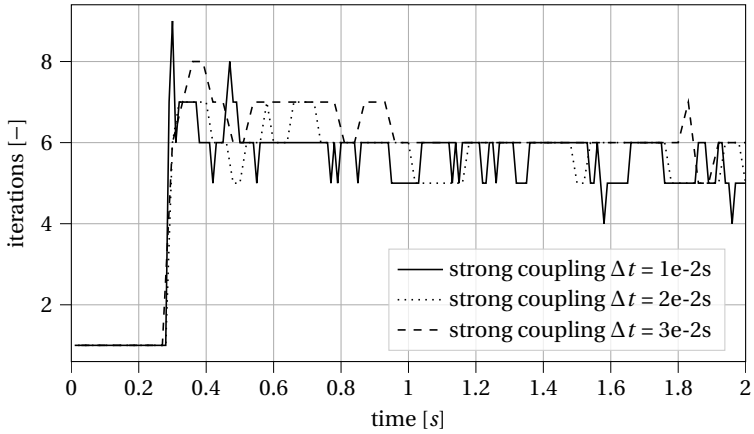

Figure 4.16: Number of interface iterations per time step - relaxed forces, adapted from [106].

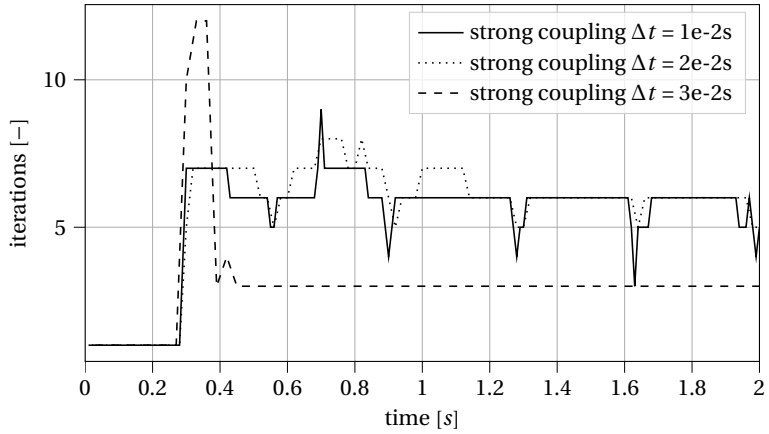

Figure 4.17: Number of interface iterations per time step - relaxed displacements and velocities, adapted from [106].

4.6.4 Influence of the Relaxation Factor

In this example, the influence of the relaxation factor ω in the case of relaxed displacements and velocities is investigated by comparing the Aitken relaxation (see equation 4.21) and a set of constant relaxation factors. For this purpose, the COR ε_n is set to 1.0 (which physically describes a perfectly elastic impact on a rigid obstacle) to neglect the influence of the wall velocity and thus concentrate solely on the relaxation factor. The same problem setup as in section 4.6.3 is used.

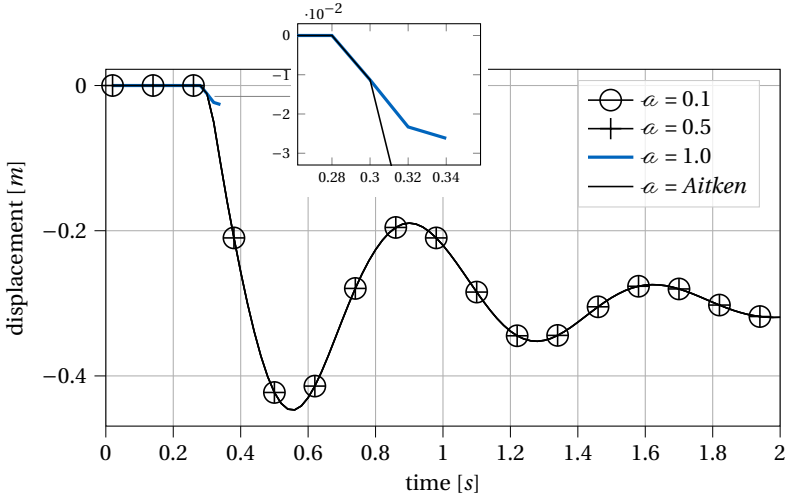

Figure 4.18: Comparison of displacement of node A, in Figure 4.11a, over time for different relaxation factors ω. With $\omega = 1.0$ the simulation becomes unstable shortly after the first contact is detected. Underrelaxation of $\omega < 1.0$ leads to stable simulations, too. However, this is more computationally costly than using the optimized Aitken relaxation factor [106].

As Figure 4.18 shows, a constant relaxation factor can be used as long as it is smaller than 1.0. $\omega = 1.0$ describes a non-relaxed system and does not find a proper solution for this given example. Manually finding a suitable constant relaxation factor is cumbersome and is dependent on the system setup. In addition, it heavily influences the solving time, as Table 4.2 demonstrates. For a constant ω and the Aitken ω (see equation 4.21), the comparison is performed with respect to computation time. It can be noted that although constant relaxation factors provide good results, the optimized Aitken relaxation factor facilitates faster convergence to the residual.

relaxation factor ω	relative computation time
0.1	100.0 %
0.2	54.1 %
0.5	20.4 %
0.7	28.5 %
Aitken	18.7 %

Table 4.2: Comparison of computation time with different relaxations and the Aitken relaxation [106].

4.6.5 Influence of the Coefficient of Restitution

Appendix F.1 discusses the influence of the coefficient of restitution ε_n with Figure F.3 visualizing the course of the influence of ε_n on the contact forces. If ε_n is close to 0, the influence of ε_n becomes larger and larger and finally tends to infinity. To investigate possible consequences for a coupled simulation, ε_n is varied in this section and the results are presented in Figure 4.19. It shows, ε_n directly influences the contribution of the DEM rigid wall velocity to the contact force. Current state of the art publications such as [5, 24, 97] express the importance of the ε_n value for impact simulations.

Different ε_n values are used while the time step is kept constant to perform this case study.

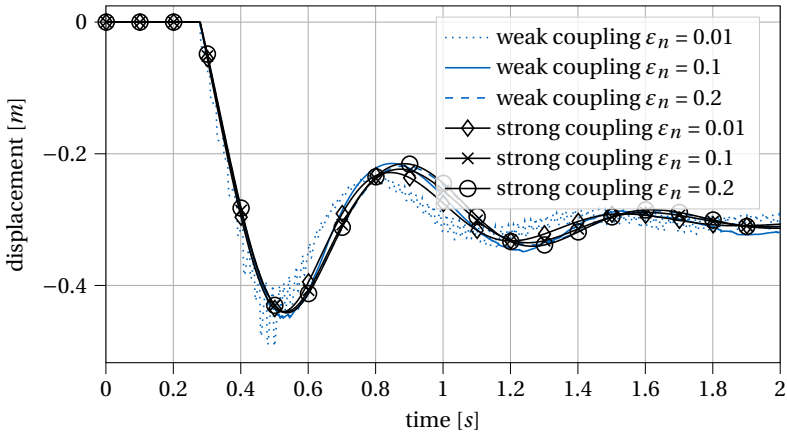

Figure 4.19: Comparison of different ε_n values [106].

As visible in Figure 4.19 the interface coupling becomes unstable as soon as ε_n reaches a small value. This instability can be overcome by using the strong coupling algorithm presented in section 4.5 and is a result of the increased influence on the contact force in the system [31], see Figure F.3. Additionally, Figure 4.19 describes another important feature: The choice of ε_n does not influence the final damped solution of the structure* but only the maximum transient solution.

Figure 4.20 visualizes the progression of the maximum interface iterations over the simulation time and indicates the advantages of the proposed coupling algorithm. The large number of iterations at the time of first contact ($t \approx 0.25s$) calls for a small time step due to the increased difference in interface velocities. This can be overcome with the help of additionally introduced interface iterations. As the simulation proceeds and the initial velocity difference is properly controlled, fewer iterations are needed to enforce the interface conditions.

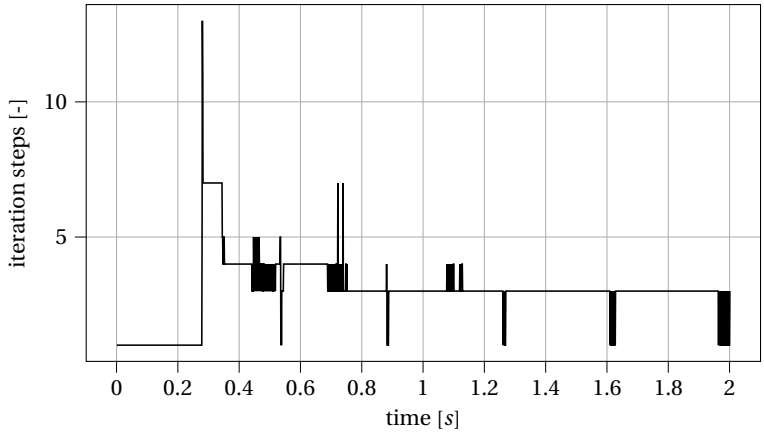

Figure 4.20: Strong coupling interface iterations for $\varepsilon_n = 0.2$ [106].

* See "static" in Figure 4.15.

4.6.6 Energy-Conservation

In order to study the evolution of energy in both individual systems and the coupled system, Figure 4.11a's setup is simulated with the following parameters. A particle with a radius $R = 0.25m$ is dropped from a height of $0.26m$ on a cable structure with a reference cross section $A = 0.01m^2$. Structural damping is neglected.

	$\rho_0 \left[\frac{kg}{m^3}\right]$	$E \left[\frac{N}{m^2}\right]$	ν [−]	ε_n [−]	μ_P [−]	$\bar{S}_0 \left[\frac{N}{m^2}\right]$	$g \left[\frac{m}{s^2}\right]$
Particle	2500	1e5	0.2	1.0/0.5	0.58	-	9.81
Structure	7850	2.069e11	0.3	-	-	1e5	

Table 4.3: Simulation input data.

The COR ε_n is varied to model both a fully elastic and partially elastic impact. During the non-perfect elastic impact, energy is "lost"*, which is then referred to and tracked as damping energy.

- The following Figures, 4.21 and 4.22, show the simulation results for ε_n = 1.0 and ε_n = 0.5, respectively.
- Figures 4.21a and 4.22a represent the path of the impacting particle.
- Figures 4.21b and 4.22b visualize the energy in the DEM simulation and Figures 4.21c and 4.22c in the FEM simulation.
- Finally, Figures 4.21d and 4.22d show the total energy in the system, which must remain constant.

It is evident in both figures that the total energy remains constant except for a minor error, and no additional energy is introduced into the system.

Remark: Derivation of Energy Terms

Appendix G contains the equations necessary to calculate the respective energy terms.

* Transformed to energy terms that are not apparent in the mechanical DEM system, such as heat, noise, and other effects, for instance, irreversible deformations in the particle.

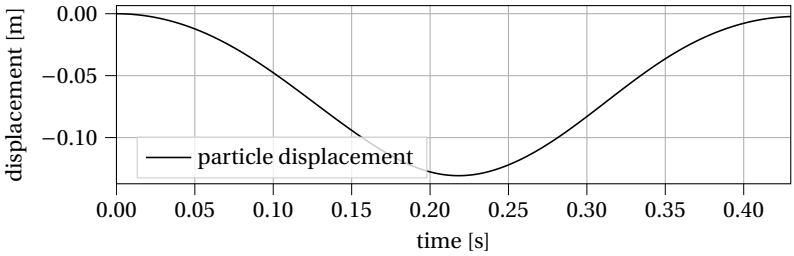

(a) Displacement of impacting sphere.

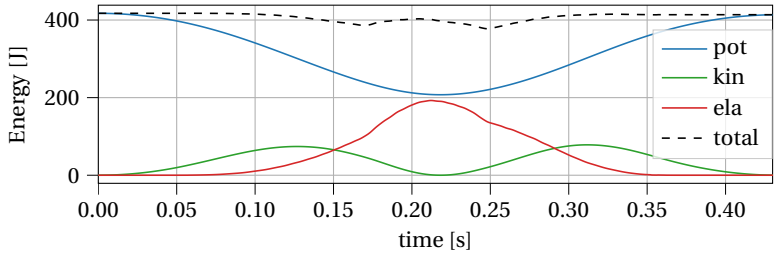

(b) Energy DEM.

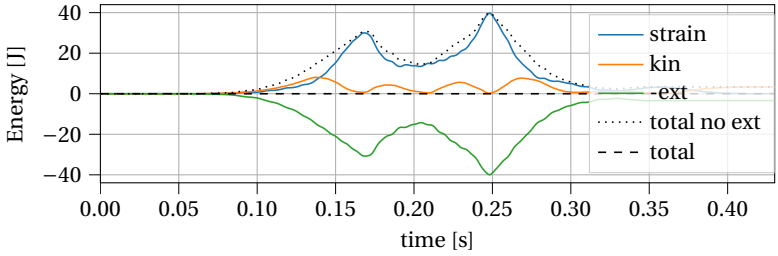

(c) Energy FEM.

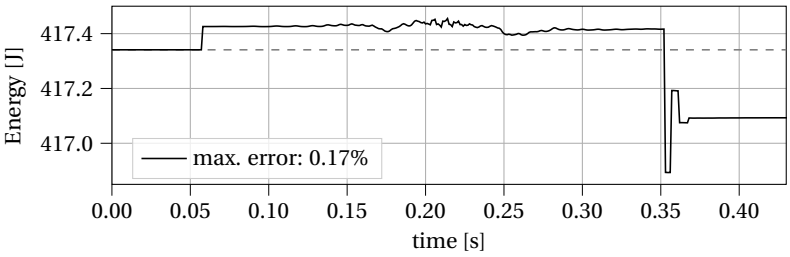

(d) Energy total system.

Figure 4.21: Course of the energy over time. Simulation with a COR $\varepsilon_n = 1.0$. No energy is dissipated by the impact of the sphere.

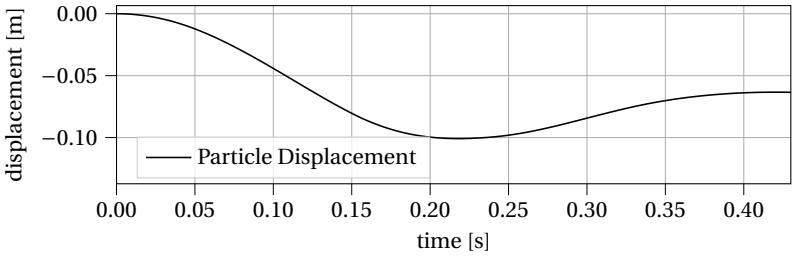

(a) Displacement of impacting sphere.

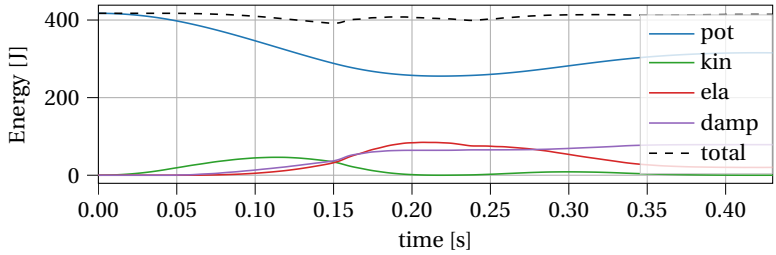

(b) Energy DEM.

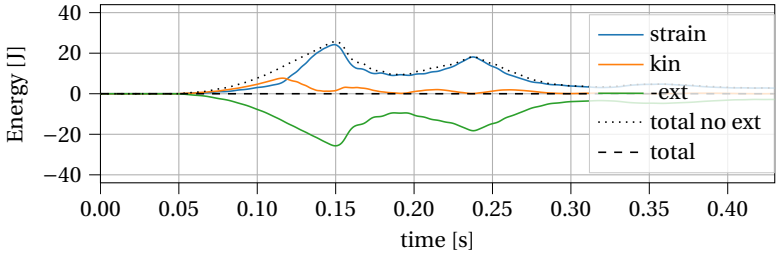

(c) Energy FEM.

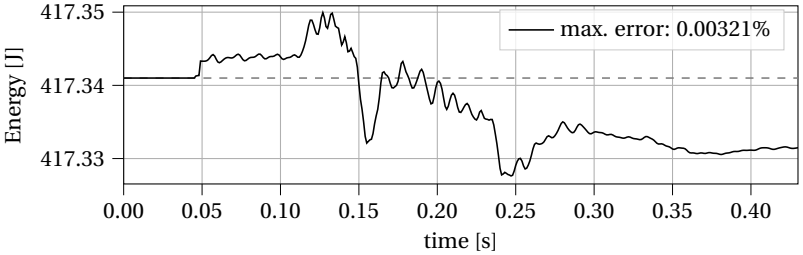

(d) Energy total system.

Figure 4.22: Course of the energy over time. Simulation with a COR $\varepsilon_n = 0.5$. Some energy is dissipated by the impact of the sphere. The dissipated energy is tracked over time and visualized by the damping energy in Figure 4.22b.

4.6.7 Practical Application: Angled Protection Net

One prominent practical application case of highly flexible structures can be found in mountainous regions. As an alternative to horizontal protection nets, angled nets can also be spanned over roads to direct impacting objects to a safe spot, as shown in Figure 4.23a.

(a) Route Chalais-Vercorin, Valais. Photograph is property of Geobrugg (https://www.geobrugg.com).

(b) Numerical DEM-FEM coupled model.

Figure 4.23: Picture of the protection net and the corresponding, simplified numerical model, including the net as cable structure and two impacting rocks modeled as single DEM particles. One particle is chosen to be small enough to penetrate the net, verifying the correct contact detection [106].

To test the limits of the presented algorithms, in this study, the same system as shown in Figure 4.23b is modeled without pre-stressing the cable structure, leading to a very compliant structure (compare Table 4.4). Additionally, a small COR of $\varepsilon_n = 0.2$ and a high impact velocity are chosen to introduce even more difficulties due to an increased contact force.

FEM		DEM	
E	$7e5\,\frac{N}{m^2}$	E	$1e5\,\frac{N}{m^2}$
A	$1.26e-5m^2$	$\dot{\mathbf{u}}_0$	$[0.0,-5.54,-5.54]\,\frac{m}{s}$
ρ_0	$7.85e3\,\frac{kg}{m^3}$	ρ_0	$2.5e3\,\frac{kg}{m^3}$
$\bar{S}_0$	0	R_i	$[0.21, 0.05]\,m$
α_d	20	ν	0.20
β_d	0	ε_n	0.2

Table 4.4: Properties of FEM and DEM part [106].

Using a time step of $2e-4s$, the different behaviors after impact are presented in the following figures 4.24a and 4.24b.
Similar to the example from subsection 4.6.2, the weakly coupled problem experiences too large contact forces and loses contact between the impacting object and the structure, whereas the strong coupling algorithm manages to keep the contact for the given time step (see Figure 4.25).

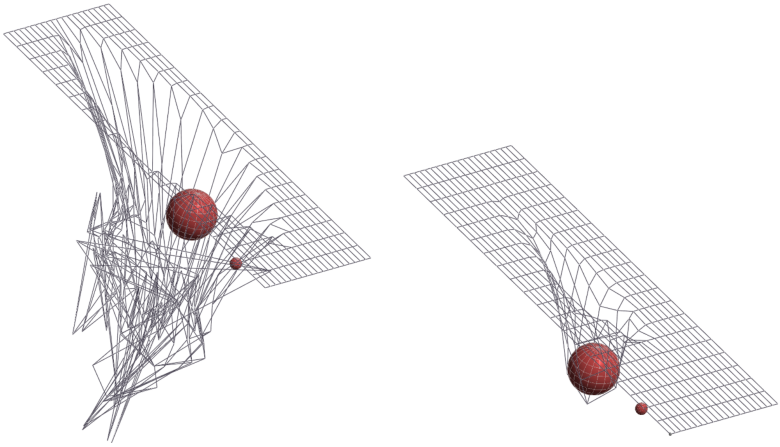

(a) Weak coupling. (b) Strong coupling.

Figure 4.24: Comparison of the weak coupling to the strong coupling approach with the same time step $\Delta t = 2 \cdot 1e-4s$ [106].

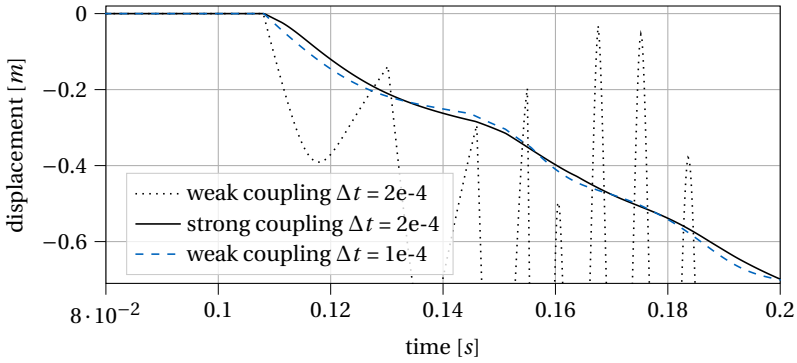

Figure 4.25: Weak vs. strong coupling displacement of center node [106].

CHAPTER 5

Validation of Simulation Approach

The following chapter shows the application of the theoretical approaches described so far by applying the element formulations, material laws and the described coupling methodology. Two actual experiments are investigated and simulated. The selection is made so that the two most important types of protective structures are discussed. In section 5.1's first experiment, a standardized rock is dropped without rotation in the direction of gravity onto a flat protective net.
In contrast, an Attenuator protection net is modeled and calculated in section 5.2. Here, the rock hits a vertically suspended net with a particular rotational velocity. This resembles a curtain and guides the impacting rocks instead of catching them. Several studies are conducted during the simulations. Among others, the influence of the DEM cluster refinement on the accuracy of the results and the required computation time is investigated in section 5.1.
The results of this chapter were published by the author in [104] and [103] during the course of this dissertation.

All examples apply a Hertz Mindlin Spring Dashpot Model (HM+D) law to calculate the DEM contact forces. A detailed description is given in Appendix F.

5.1 CTI Frame

The experiment presented here is modeled and simulated to verify the DEM-FEM coupling methodology and apply it to an actual structure. The simplicity of the structure construction is an advantage to focus on the coupling and further on the investigation of the DEM cluster refinement. For this reason, simplified structural parameters are chosen.
First, a description of the experiment and a discussion of the structural modeling using the FEM is given. Subsequently, the appropriate modeling of the impacting rock and the corresponding DEM cluster refinement are discussed. Then, the simulation results are compared with the experimental data.
The results of this section were published by the author in [104] and are discussed and reproduced below in the context of the dissertation. Some parts of the follow-

ing text passages are copied directly from [104] and are therefore to be interpreted as quotations.*

5.1.1 Experiments

The experiment setup is described below. In this work, only the required comparative data will be published, while the remaining data are not publicly accessible as a property of Geobrugg. A standardized† concrete block is used, with a total mass of $180kg$ (the concrete block mass in itself weighs $175kg$, the attached wire rope strap weighs $5kg$ bringing the total mass of the block to $180kg$) and an edge length of $0.41m$ impacts a $3.9 \times 3.9m^2$ DELTAX® G80/2 [49] (see Figure 5.2) net which is spanned into a CTI-Frame with rigid boundaries. The rigid boundaries are, in this case, 5/8" shackles connecting the mesh to the steel frame.
The block is dropped from a height of $2.0m$ which results in an impact velocity of $\dot{u} = \sqrt{2.0 \cdot 9.81 \cdot 2.0} = 6.261484 \frac{m}{s}$. The tests are laid out to produce a rebound of the block without failure of any mesh wire.

The same test is repeated twice, whereas (due to different pre-stresses) the initial sag, as a result of the dead load, varies from $0.05 - 0.10m$, labeled with *exp_1* respectively *exp_2* hereafter.

Label	*exp_1*	*exp_2*
Initial Sag $[m]$	0.05	0.10

Three main parameters, displacement, velocities, and forces are obtained from these tests utilizing a high-speed camera and an internal acceleration measuring device. The high-speed camera records at a resolution of 1280×1024 and a frame rate of $5e2$ fps. The acceleration sensor is composed of a built-in triaxial accelerometer with a range up to $5e2g$ and a sampling rate of $2e4Hz$ and is incorporated in the test block. Deflection, this means, the vertical displacement or sag of the mesh after impact, is measured directly through the analysis of the videos obtained from the high-speed camera. The block's velocity is calculated by following the block's trajectory over time in the high-speed video, based on the principle $dx/\Delta t$. The velocity before impact is compared between the computed one, as explained above, and the result from the video analysis, to ensure the plausibility of the video analysis. Finally, the analysis of the accelerations obtained by the accelerometer yields the force evolution over time.
The repeatability of the tests is deemed to be given. Five tests are carried out in total. The test block and the drop height are the same for all tests, this means, the input parameters are kept constant. Three parameters vary slightly, but all are considered to be in a negligible range. The dimensions of the net panel itself vary by $+/-5\%$. The tensioning force is not directly measurable when installing the net panel in the test frame. This leads to a variation of the sag of $+/-5cm$. Finally, the material's tensile strength varies between $1700N/mm^2$

* Whose main author and copyright owner is the author of this dissertation.
† Swiss Agency for Environment, Forests and Landscape (SAEFL)

Figure 5.1: Photograph of the testing site in Walenstadt, Switzerland, showing the CTI-frame [104].

and $2030 N/mm^2$. This could be important when analyzing the breaking load, although this variation is also deemed negligible in the practical application since the lowest value is always considered. The tensile strength is of minor importance for this work as no damage in the mesh is observed.

5.1.2 Modeling

5.1.2.1 Structure

Due to the set-up of the experiment and the fine mesh of the used protection netting (see Figure 5.2), a simplification of the net to a closed, homogeneous surface suggests itself. This assumption simplifies structural modeling and allows the use of two-dimensional finite elements. Publications such as [83, 117] suggest a shell element to be used. While the advantages are clarified in these publication, it would mean an overhead for the underlying experiment. Owing to its simplified set-up, a plate in membrane action is used. An initial plane geometry has zero out-of-plane stiffness, carrying only in-plane stresses and omitting rotational nodal degrees of freedom. As a remedy, a minor pre-stress is applied to the structural model (see Table 5.1) to provide a non-singular stiffness matrix at the beginning of the simulation. The modeling procedure is visualized in Figure 4.6a.
The Young's Modulus is calibrated to the given value in Table 5.1 in order to achieve an initial sag due to dead-load of $\approx 0.05m$ (see Figure 5.3), as described in the experimental set-up.

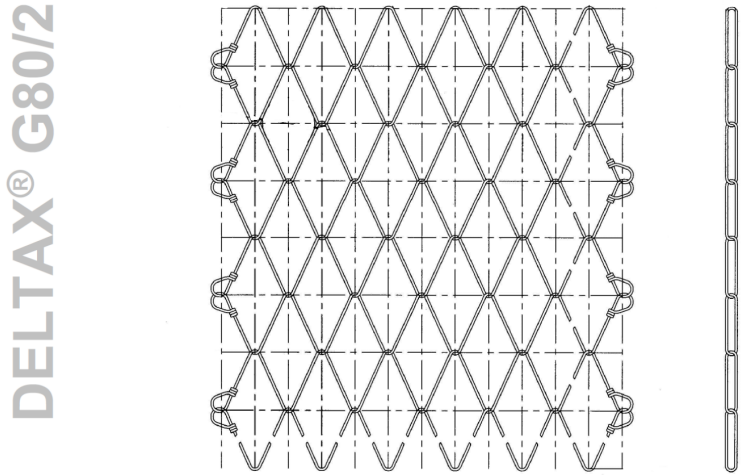

Figure 5.2: Technical drawing of the DELTAX® G80/2 [49, 104].

Thickness d $[m]$	$8e-3$
Isotropic Pre-stress $\tilde{\mathbf{S}}_0$ $\left[N/m^2\right]$	$[0.01, 0.01, 0.0]$
Density ρ_0 $\left[kg/m^3\right]$	81.25
Young's Modulus E $\left[N/m^2\right]$	$5e7$
Poisson's ratio ν $[-]$	0

Table 5.1: Numerical properties for the structure.

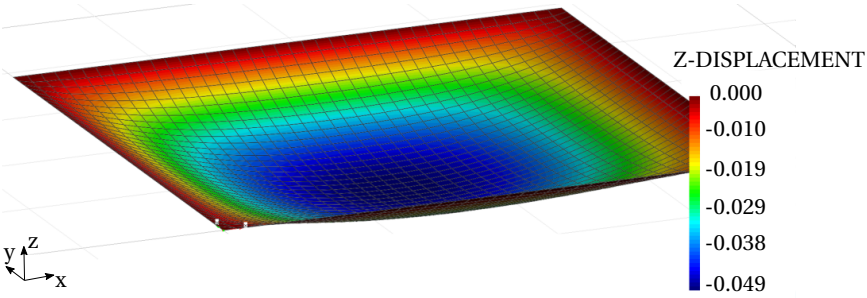

Figure 5.3: Initial static analysis to obtain equilibrium position for dead-load $[m]$ (plot scaled by factor $\times 10$) [104].

With respect to the technical data sheets available on [49] the thickness of the plate in membrane action element is set to $0.008m$, whereas the density is derived from the provided mass of $0.65\,\frac{kg}{m^2}$ DELTAX® mesh standard roll:

$$\rho_0 = 0.65\ \frac{kg}{m^2} / 0.008\ m = 81.25\ \frac{kg}{m^3}. \tag{5.1}$$

Remark: Simplified Structural Modeling

As described in the experimental set-up in section 5.1.1 the two tests that are investigated show a rebound of the impacting sphere and no damage. Due to the observed structural response a simple elastic material model [8] and a Poisson's ratio of $\nu = 0$ is applied. In the course of this work it is shown that structural models with the right simplifications allow a correct assessment of the global behavior. If a detailed analysis of the deformation behavior and failure behavior of individual structural elements is to be carried out, more attention must be paid to structural modeling.

5.1.2.2 Impacting object

In section 3.3.5, the use of particle clusters is explained. This method for modeling the real rock geometry will be used in the following. Since no detailed investigation of the appropriate refinement of DEM clusters for modeling actual rock geometries has been published so far*, different refinement levels are generated. Furthermore, their influence on the results and the required computational time are investigated.
As depicted in Figure 5.4, the standardized experiment object is modeled with seven different levels of refinement. Ranging from a representation as a single sphere to a detailed geometrical description with up to 22,232 spheres. Special algorithms are needed to create such refined cluster files. Accordingly, the Sphere-Tree algorithm described in [17, 18] is employed as it is available in an online toolkit [16].

* The results and investigations of this chapter have been published by the author in [104].

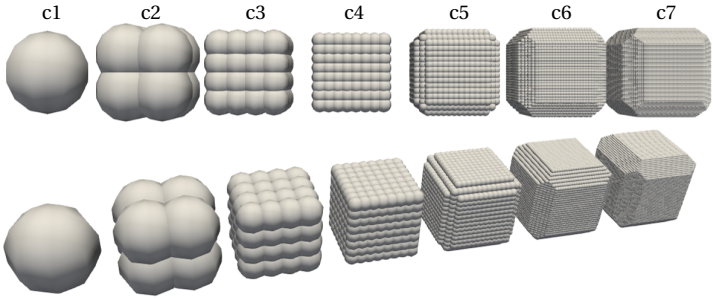

Figure 5.4: Cluster refinement (1,8,56,296,1280,5408,22232) [104].

The density of the respective cluster is fitted to obtain a total cluster mass of $180kg$ (see section 5.1.1). Important DEM parameters, such as the coefficient of restitution ε_n [107] and the Young's Modulus E of the particle, are varied with respect to Table 5.2 while studying their influence. The range in which E is selected is based on the results of a preliminary study*.

#	nr. of spheres	ε_n	$E\,[N/m^2]$
c1	1	0.5	$1e5$
c2	8		
c3	56		
c4	289		
c5	1280		
c5_a	1280	0.2	$5e5$
c6	5408	0.5	$1e5$
c7	22232		

Table 5.2: Cluster versions, as visualized in Figure 5.4 [104].

5.1.3 Validation

The experiment produced results which are used to validate the proposed coupling algorithm and to investigate the influence of discrete element cluster refinement, time step Δt, coefficient of restitution ε_n, and the Young's Modulus E on the final solution of displacement, velocity and reaction force F_R. Furthermore, it is shown that simplified structural modeling allows an appropriate evaluation of the global structural behavior.
Each of the aforementioned clusters, described in Table 5.2, is used in the numerical impact simulations. If not mentioned otherwise a time step value of $\Delta t = 1e-5s$ is used. The results with the label *"small Δt"* follow from a simulation with $\Delta t = 1e-6s$.

* Comments on the proper choice of the Young's Modulus and its interpretation as a penalty factor can be found in sections 3.3.3 and 5.2.3.1.

Although the simulated system setup is more similar to *exp_1*, the experimental results for *exp_2* are added to the result plots as it represents an experiment with the same impact velocity and the same mass of the impacting object. Moreover, the difference in the initial sag is a result of the test setup and can hardly be controlled. Thus, it allows error zones to be added in the result plots to show the variability of the experimental results.

5.1.3.1 Displacement

The simulated displacement values of the impacting object are compared to the experimental results. Figure 5.5 demonstrates that the simulation results lie between the two experimental results. It is noticeable that already with more than one sphere in the cluster a good agreement with the experimental data can be seen. To explain this behavior the simulation is visualized at the time of maximum displacement in Figures 5.7 - 5.13 (see Figure 5.6 for comparison to the experiment). Due to the fact, that the contact forces in DEM are calculated with the help of spring-dash-pot models [31, 98, 107] the single sphere with one large radius experiences an indentation, which is larger than it is for the clusters with more smaller spheres. This has additional effects too, which become clear in Figures 5.14 and 5.15. The single particle has a larger indention (Figure 5.7) and thus decelerates slower (Figure 5.14). This finally leads to lower contact/reaction forces and a longer duration of load application, as visualized in Figure 5.15. The same behavior is observed when decreasing the time step* and consequently can be concluded to be a problem of the very rough representation of the original geometry as a single sphere and not the choice of the time step size.
Regarding the remaining refinement levels, a good agreement with the *exp_1* is shown, as the initial sag of the numerical model due to dead-load matches with the initial sag of the first experiment set-up *exp_1* of $0.05m$, while the displacements of all simulation results are within the error zone.

* See Figure 5.5, label "c1 small Δt".

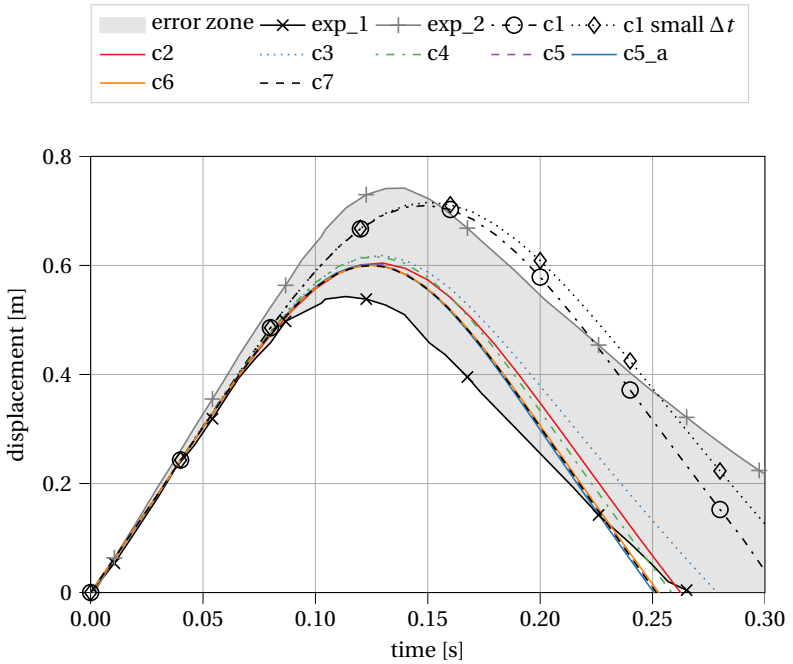

Figure 5.5: Displacement of impacting objects [104].

Figure 5.6: Maximal deflection, experiment [104].

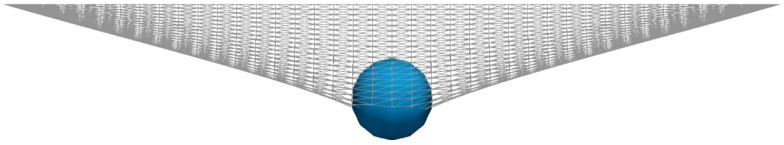

Figure 5.7: Maximal deflection, cluster 1 [104].

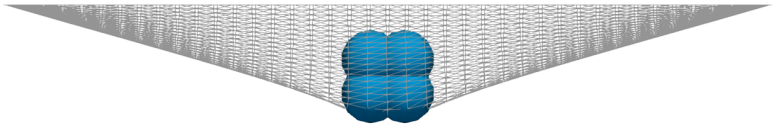

Figure 5.8: Maximal deflection, cluster 2 [104].

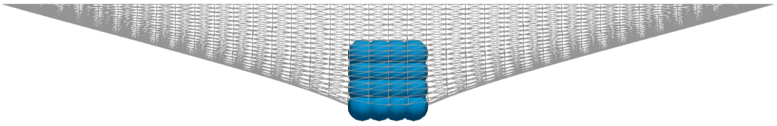

Figure 5.9: Maximal deflection, cluster 3 [104].

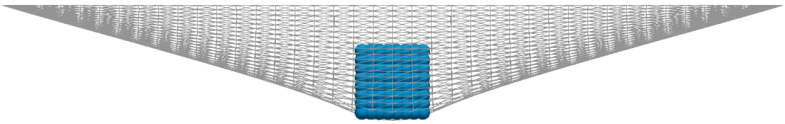

Figure 5.10: Maximal deflection, cluster 4 [104].

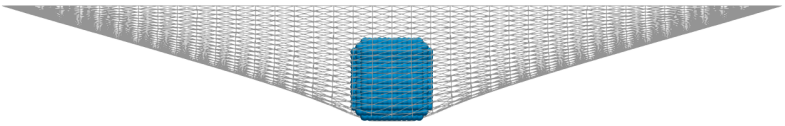

Figure 5.11: Maximal deflection, cluster 5 [104].

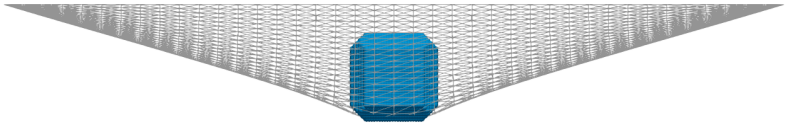

Figure 5.12: Maximal deflection, cluster 6 [104].

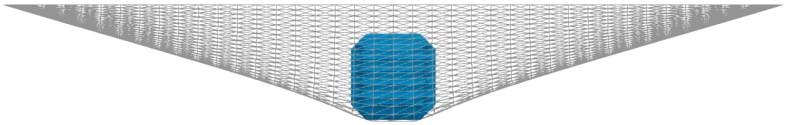

Figure 5.13: Maximal deflection, cluster 7 [104].

5.1.3.2 Velocity

Similar to the observations in subsection 5.1.3.1 all cluster refinement levels show good agreement with the experimental velocity results in Figure 5.14. The exception is again the single sphere c1 which decelerates more slowly due to its larger indention (Figure 5.7). Again, the choice of the time step size does not strongly influence the behavior of c1.

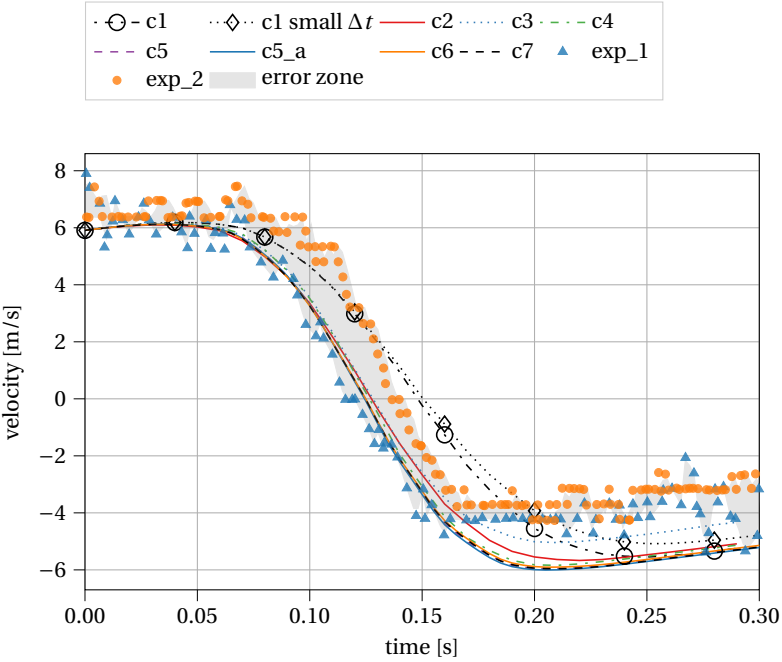

Figure 5.14: Velocity of impacting objects [104].

5.1.3.3 Force

Lastly, the forces obtained from the numerical simulation are compared to the experiment results. Figure 5.15 shows the reaction forces in the structure as a sum over all boundary nodes. A good agreement for all cluster refinements >c1 can be observed for both the force value as well as the contact time. Similar to the observations in the previous sections, the roughest object representation performs poorly. The maximum force is below the experimentally obtained value, and the time the object is in contact with the structure is too large. c1, as the roughest object representation, is a single sphere, poorly representing the correct object shape.

Concerning the forces, it can also be said that more precise modeling of the exact object geometry plays a significant role, even if the impact, as in this case, takes place without rotations.

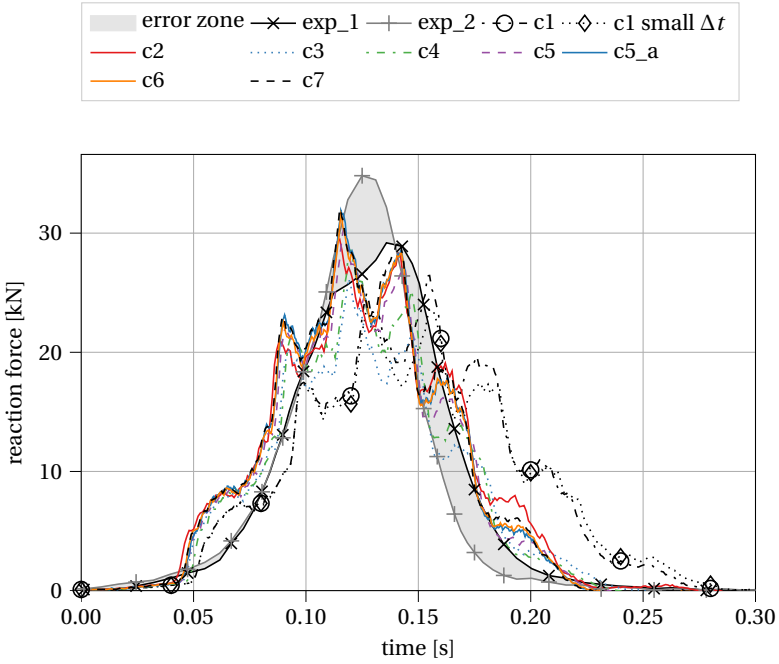

Figure 5.15: Reaction forces $F_R(t)$ [104].

Impulse

Another helpful parameter in comparing simulation results with experiments is an integration of forces over time. This ignores local differences and puts the overall behavior into context. By integrating the reaction forces over time, Figure 5.16 visualizes the comparison of the impulse. Almost all simulation results are slightly above the experimental results but close to them. For example, cluster version c4 fits excellently, while the coarsest simplification c1 represents the worst result. Considering the differences between c5 and c5a, the importance of matching material value tuning can be emphasized again. Good simulation results can be achieved once suitable material values, and cluster refinements are found. This tuning is, as already mentioned, a weakness of the method and is due to the contact force calculation of the DEM. The results of the cluster versions c4 - c6 deviate by a maximum of 7% from the experimental results, and show for the time course of the reaction forces in Figure 5.15 good agreement with the time course of the experiment.

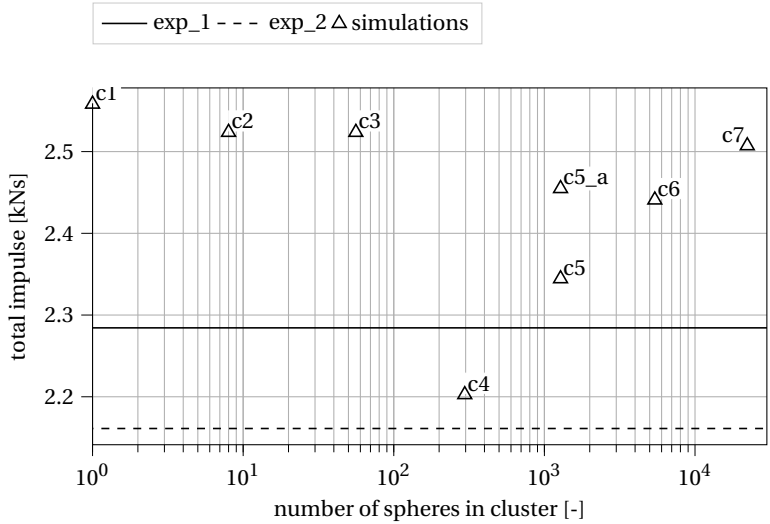

Figure 5.16: Total impulse $\int_0^t F_R(t)\,dt$. Integration of forces in Figure 5.15 over time.

5.1.3.4 Results

With respect to the relative computational time for each simulation, shown in Figure 5.17, the effect of additional particles is negligible under $\approx 10^3$ spheres but increases rapidly for larger number of spheres.

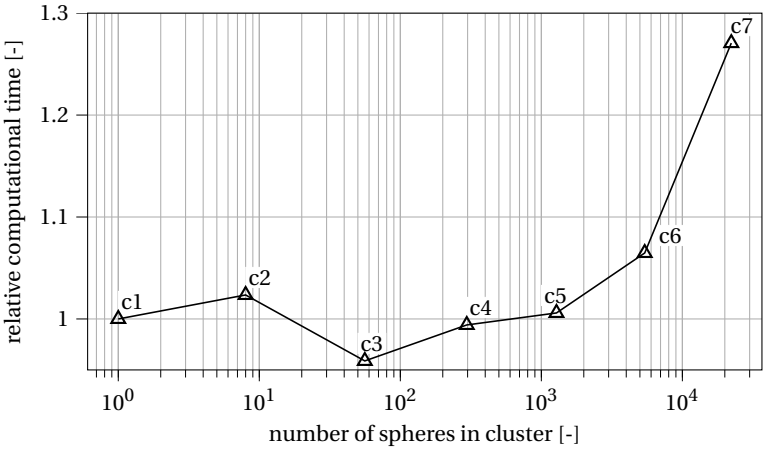

Figure 5.17: Comparison of relative computational time for different cluster refinement levels, adapted from [104].

Additionally, considering the results in the section 5.1.3, the cluster version c4 is recommended for usage. It represents the best compromise between accuracy and computing effort, while also properly representing the geometry (see Figure 5.4). It is also expected that the fine representation of the impacting object influences the simulation results favorably if the rotation of the object plays a crucial role*. This feature will come in handy for the experiment in the next section, in which the impacting rock has an angular impact velocity.
The computational time for the simulation of the cluster c4 is discussed as an example. A total time of $1,108s \approx 18.5min$ with an increased time step of $\Delta t = 2e-5s$ for a total simulation time of $0.3s$ is required. With respect to Figure 5.5, the cluster leaves the reference axis of origin at $\approx 0.25s$, thus the simulation time could be further reduced by $\approx 17\%$. The Central Processing Unit (CPU) system settings for this simulation is an `Intel(R) Xeon(R) CPU E5-2623 v4 @2.60GHz`. A good agreement can be found with the experimental results regarding the simulation results. Of course, the influence of the cluster refinement and the appropriate choice of material parameters affect the simulation results, but the general course suggests the correctness of the coupling methodology. With the confidence in the simulation environment gained here, a much more complex protection structure is investigated in the following section.

* See also [128], where a simplified Attenuator is simulated by using an arbitrary shaped rock object.

5.2 Attenuator Barrier

After the results of the previous section 5.1 have inspired confidence in the presented coupling method, a more complex protection structure is investigated and simulated in this section. So-called Attenuator structures are not installed horizontally or inclined but hang vertically in the gravitational direction. Therefore, they can be compared simplified with curtains. Their mode of operation also differs from ordinary protective nets in that they deflect impacting objects instead of catching them. In the following section, the suitable experiment and the performed measurements are described in detail. Subsequently, the structural modeling will be discussed using the element formulations and material laws from the theory section 3.2. The modeling of the rocks is performed with particle clusters as in the previous section. However, a study of the cluster refinement is omitted, and instead, the experiences of the previous section are used. Finally, the usability of the coupling method is demonstrated by two different experimental runs and the corresponding simulations, showing that the simulation results agree very well with the experimental data.
The results of this section were published by the author in [103] and are discussed and reproduced below in the context of the dissertation. Some parts of the following text passages are copied directly from [103] and are therefore to be interpreted as quotations.*

5.2.1 Experiments

In 2017 the Swiss company Geobrugg conducted an experimental program to confirm the effectiveness of a novel SPIDER® mesh [50]. The following section is a summary of crucial test aspects relevant for numerical replication†.

5.2.1.1 Test Site

The test site is a near-vertical, approximately $60m$ high slope situated in a disused granite quarry in British Columbia, Canada. For this experiment an Attenuator design with a hanging net and limited slope contact of the net, as shown in Figure 5.18a, is investigated. The test setup consists of three $8m$ steel posts set $9m$ apart and anchored to the slope with six retention cables, two lateral support cables, and one top cable penetrating the post heads. The net is attached to the top cables with shackles in each mesh opening as detailed in Figure 3.7. Three principal attenuation zones are investigated by varying the impact, transition, and collection zones of the high tensile steel wire nets.

5.2.1.2 Site Survey and Rockfall Modeling

Truline Survey‡ performed a terrain survey of the site in 2016, which was used as the basis for rockfall modeling to adapt the Attenuator geometry between the

* Whose main author and copyright owner is the author of this dissertation.
† Refer to [60] for full testing details.
‡ https://www.trulinelandsurveyors.com/

testing series of 2016 and 2017. Chapter 6 demonstrates how such terrain models may be incorporated into simulations to enhance accuracy and predictive confidence further.

5.2.1.3 Impacting Object

The rocks used for testing are either granite blocks of various characteristic shapes (such as cubic, angular, and disc-like) or prefabricated concrete blocks with a special housing in the center for rock motion sensors (see Figure 5.18b). An excavator then releases the blocks and rocks on top of the slope. The rocks bounces three to four times on the granite slope before impacting the net.

5.2.1.4 Instrumentation

Experimental instrumentation includes load-cells in all cables, high-speed cameras filming the block's trajectory from different angles, and rock motion sensors in the concrete blocks. This section will predominantly focus on the trajectory path, translational velocity, and rotational velocity experimental data collected.

High Speed Cameras

Analysis of the high-speed camera videos with a sampling rate of $5e2$ fps facilitates the quantification of the rockfall dynamics. By tracking the block's position through time, a translational velocity can be obtained, and the tracking of every $90°$ rotation of the block serves as an indicative quantification of angular velocity. In addition, the cameras are located to have a frontal view on the mesh and a perpendicular view. This also allows to determine in which plane the block is moving.

Rock Motion Sensors

The rock motion sensors measures the accelerations and rotations of the block about its three axes for the duration of each test. Comparing the angular velocity obtained from the video analysis and the rock motion sensor shows good agreement and therefore provides confidence in the translational velocity data estimated by video analysis.

5.2.1.5 Tests Used for Numerical Validation

The tests used to validate the modeling and simulation use a Geobrugg SPIDER® S4/130 mesh (described in [50] and visualized in Figure 5.18c). Additional weights in the form of steel bars are shackled to the bottom of the mesh (see Figure 5.18a) to increase the inertia and vertically pre-tension of the system and is incorporated in the simulation with additional point masses. The middle post is slightly bent after sustaining two rock impacts in previous tests, but the integrity and function of the system are not compromized.

The blocks used during the test are

- a near-cubic $626kg$ concrete block with an initial volume of approximately $0.75 \times 0.75 \times 0.75m^3$ called **T092** and
- a $278kg$ granite block with an initial volume of approximately $0.75 \times 0.51 \times 0.48m^3$ called **T089**.

Since the blocks are used for several tests and accumulate greater damage after each run (see Figure 5.18b for T092), the mass before and after each run is the characterizing measurement (instead of volume).
Critical experimental data pertinent to numerical replication, including translational and rotational velocity at the time of impact and the rock's path and mass, are summarized in subsection 5.2.2.2.

(a) Additional weight at the bottom of the protection net to ensure a more controlled structural deformation.

(b) Photograph of the impacting object T092 (some damage can be observed). The visible metal cap covers the housing of the motion sensors.

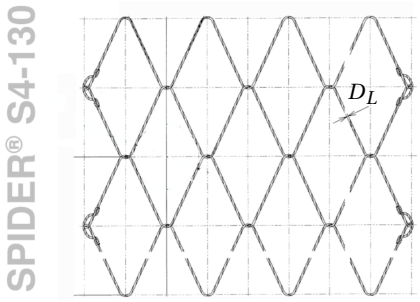

(c) Technical drawing of the SPIDER® S4-130, taken from [50], $D_L = 8.6\ mm$.

Figure 5.18: Experiment setup, adapted from [103].

5.2.2 Modeling

5.2.2.1 Structure

Figure 5.19 is adapted from [51] and depicts the respective participants in the simulation, each of which are discussed below.

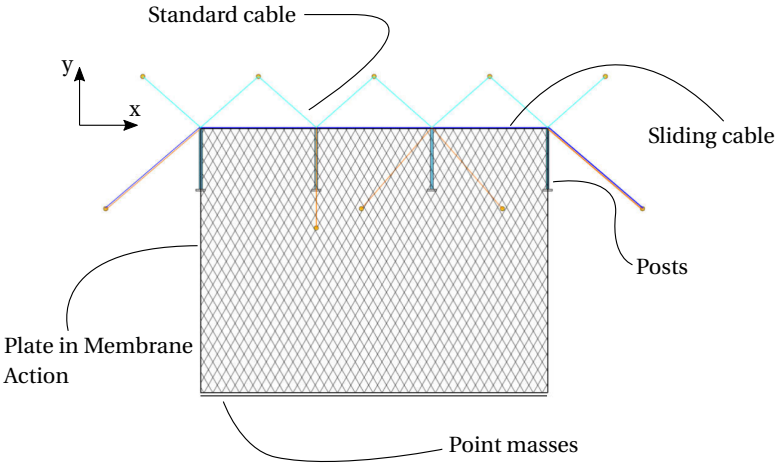

Figure 5.19: Participants in the FEM model, adapted from [51] and taken from [103].

Due to the small time steps necessary to resolve the impact, an explicit time integration scheme is selected. The central-difference explicit scheme as described by [8] is used to conduct the numerical time integration of the structural response with a time step of $\Delta t = 5e-5s$.

Point Masses

The additional weights at the bottom of the protection net, depicted in Figure 5.18a, are modeled with single point masses (summing to an additional total mass of $m_{add} = 358kg$) equally distributed along the lower boundary of the mesh (see Figure 5.19). Including these masses is critical to properly model the gravitational forces and the additional dynamic inertia.

Sliding Cable Element

Modeling the upper support rope, illustrated in Figure 3.7, demands a sophisticated element formulation, which is discussed in subsection 3.2.7.3. This formulation allows internal nodes to slide along the element, while internal forces are calculated based on the change of the total length, as discussed in [13, 124]. The following structural properties, based on construction plans in [51], are applied in the simulation.

Young's Modulus $E\ [N/m^2]$	$1.130e11$
Cross area $A\ [m^2]$	$1.645e-4$
Density $\rho_0\ [kg/m^3]$	$7.850e3$
Friction Coefficient $\mu\ [-]$	0.25

Table 5.3: Structural properties of the sliding cable element, representing the upper carrier rope [51].

Standard Cable Element

Bracing cables, modeled with standard cable elements, are anchored in the rock face and connected to strategically selected points on the supports of the protective structure. As presented in subsection 3.2.7.2, a one-dimensional truss element formulation is applied and combined with an additional check for compression stresses in the element. If such stresses are detected, the elemental stiffness contribution is temporarily eliminated from the global system of equations. Realistic structural properties are also obtained from construction plans provided in [51] and listed in the following.

Young's Modulus $E\ [N/m^2]$	$1.100e11$
Cross area $A\ [m^2]$	$1.160e-4$
Density $\rho_0\ [kg/m^3]$	$7.850e3$

Table 5.4: Structural properties of the cable element, representing the bracing cables [51].

Posts

The posts, which predominantly carry vertical loads to support the protective structure, are simply supported in the rock face. At the top they are connected to both the upper support cable as well as the bracing cables (see Figure 3.7). In accordance with subsection 3.2.7.1, these posts may be suitably modeled as one-dimensional truss elements (neglecting any initial damaged bending) with the following data.

Young's Modulus $E\ [N/m^2]$	$2.100e11$
Cross area $A\ [m^2]$	$2.010e-3$
Density $\rho_0\ [kg/m^3]$	$7.850e3$

Table 5.5: Structural properties of the truss element, representing the posts [51].

Protection net

Due to the set-up of the experiment, similar to the set-up in section 5.1, and the complex geometry of the SPIDER® net system (see Figure 5.18c), the net is

idealized as a closed homogeneous surface and is discretized with plane-stress plate in membrane action finite elements. Publications, such as [83, 117], suggest that shell elements should be used, although they introduce additional complexity and computational expense compared to plates in membrane action elements. In the interest of efficiency, plate in membrane action elements described in subsection 3.2.7.4 are employed, which, considering the excellent agreement achieved with experimental results in section 5.2.3, appear sufficiently accurate for the present study. The modeling procedure is visualized in Figure 4.6a.

The following properties in Table 5.6, determined from the mesh technical drawing in Figure 5.18c, technical data sheets [50] and proprietary Geobrugg experimental tensile tests, are applied to the plate in membrane action elements for the simulation.

Thickness d $[m]$	$8.60e-3$
Density ρ_0 $\left[kg/m^3\right]$	$5.814e2$
Young's Modulus X E_x $\left[N/m^2\right]$	$0.23e8$
Young's Modulus Y E_y $\left[N/m^2\right]$	$1.40e8$
Shear Modulus G $\left[N/m^2\right]$	$0.81e8$
ν_{xy} $[-]$	0.30

Table 5.6: Structural properties of the plate in membrane action element [50].

Remark: Small Strains

Although the material behavior is in principle non-linear, the large deformations are predominantly rigid and accompanied by small strains, justifying the linear elastic material behavior assumption.

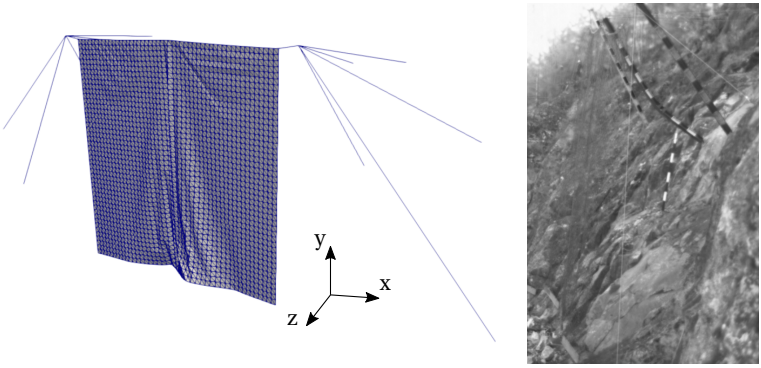

(a) Simulation.

(b) Experiment photographed just before impact.

Figure 5.20: Deformation figure after dead-load equilibrium (before impact), adapted from [103].

By comparing Figure 5.20a and 5.20b a perfect agreement between the reference computer model and the real structure cannot be achieved as some posts in Figure 5.20b are already damaged. Additionally, the position and alignment of the supporting structure are unlikely to match construction plans exactly.

5.2.2.2 Impacting Object

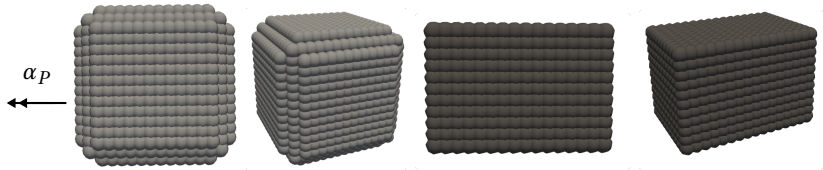

(a) Test object T092 front view.

(b) Test object T092 perspective view.

(c) Test object T089 front view.

(d) Test object T089 perspective view.

Figure 5.21: Cluster of spheres to model impacting objects, adapted from [103]. α_P describes the reference angular orientation.

In contrast to preceding works, such as [83, 124], this simulation follows subsection 5.1.2.2 to flexibly model arbitrary objects with discrete spherical element clusters. The advantage compared to standard finite element discretized objects is the simplified contact detection between arbitrary boundary objects and single spheres contained in the cluster as described by [99]. Figure 5.21 presents the DEM cluster models used within this simulation, and Figure 5.18b shows the real

impacting object T092. While the clusters in Figures 5.21a and 5.21b represent the test object T092, Figures 5.21c and 5.21d show the cluster approximation of the test object T089. A study on the proper refinement level of such clusters can be found in the previous section 5.1. Special algorithms are required to create the refined cluster file, with this section employing the algorithms described in [17, 18] available in an online toolkit [16].

Within this section several DEM particle properties are varied and their influence on the simulation result is studied, namely the friction, coefficient of restitution, and Young's Modulus. Contrasting this, the following physical properties in Table 5.7 are constant throughout all simulation runs.

	T092	**T089**
Figures	5.21a and 5.21b	5.21c and 5.21d
Mass $[kg]$	626	278
Dimension $[m^3]$	$\approx 0.75 \times 0.75 \times 0.75$	$\approx 0.75 \times 0.51 \times 0.48$
Impact translational velocity horizontal $\dot{u}_z$ $[m/s]$	10.01	13.78
Impact translational velocity vertical (gravity direction) $\dot{u}_y$ $[m/s]$	-12.08	-12.78
Impact rotational velocity $\dot{\omega}\,[rad/s]$	22.0	10.0

Table 5.7: Given physical properties of the impacting objects.

Comparing Figure 5.18b and 5.21 it can be observed that the testing objects have already suffered damage from previous experiments. When comparing the simulation results with the ones obtained by the experiment in section 5.2.3 this unavoidable difference should be considered.
An explicit central-difference scheme as described by [80] is used to conduct the numerical time integration of the translational velocity of the cluster with a time step of $\Delta t = 5e-5s$. As presented in [63], a more sophisticated time integration approach is used to integrate the rotational velocity using quaternions [59], which is especially critical due to the non-uniform geometry of the impacting clusters as shown in Figure 5.21.

5.2.3 Validation

The following section presents the simulated Geobrugg 2017 experimental results to ascertain the practical applicability and accuracy of the aforementioned numerical modeling approaches and technologies. In the subsequent investigations, the unknown model parameters are varied to check their influence on the test run T092. To validate the results, the test T089 is subsequently simulated with the best suitable parameters obtained from the investigation of T092, omitting a new material parameter tuning.

For clarity, key assumptions and uncertainties discussed in the preceding sections are summarized below:

- The exact impact location is estimated from video records.
- The model of the protective structure is taken from construction plans. However, it can be seen from photographs and video recordings that the actual structure is partially crooked and already shows damage.
- The reference angular orientation α_P of the impacting object describes the rotation around the main axis of the impacting object at the time of impact. It cannot be determined and is therefore included in the following investigation as an unknown variable. This also means that the angular velocities cannot be absolutely compared. The orientation of α_P is visualized in Figure 5.21a.
- Three further DEM specific parameters cannot be taken unambiguously from the test and have to be varied to study their influence. The particle's Young's Modulus E, coefficient of restitution ε_n and friction μ_P are partly problem-dependent and their influence is not well-researched with regard to Attenuator barriers.
- As visualized in Figure 5.18b the impacting test object already shows damage, which is neglected in the modeling of the DEM sphere cluster.

The rock trajectory, translational velocities, and the general trends of the angular velocity are used for comparison with the experiment.

5.2.3.1 Trajectories

The most reliable and functionally-important comparison is the simulated versus experimental rock trajectory. Attenuator barriers are used to protect exposed areas such as motorways from falling rocks, therefore, the object's path is of particular interest. Figures 5.22 and 5.23 illustrate the influence of the DEM parameters for T092 (which are not clearly defined and have to be varied to study their influence).

T092

The T092 test case is simulated while some specific DEM material parameters are not pre-determinable. In order to determine their influence on the simulation results and finally to find the most suitable material combination, one parameter is continuously varied in the following while the other unknown quantities are kept constant. Table 5.8 gives information about this procedure and refers to the respective figures of the trajectories.

# Figure	5.22a	5.23a	5.22b	5.23b
Coefficient of restitution ε_n [−]	0.2 – 0.6	0.6	0.6	0.6
Young's Modulus $E\,[N/m^2]$	2e6	5e5 – 2e6	2e6	2e6
Friction μ_P [−]	0.4	0.4	0.15 – 0.4	0.4
Reference angular orientation α_P [°]	146.25	146.25	146.25	0 – 135

Table 5.8: Parameter study for the simulation of T092. To investigate the influence of the respective DEM parameters, numerous simulations have been run and their results are plotted in Figures 5.22 - 5.23. The table fields with a blue background represent the parameters that are varied in each case.

Remark: The Young's Modulus and Other DEM Parameters

While the deformation of the impacting object is not of interest for this study, the so-called Young's Modulus E here represents only an algorithmic parameter in the calculation of the DEM contact forces (see Appendix F). The range of E in this simulation does not represent the physical properties of concrete but proves to result in the best fitting results. This can also be observed when the obtained parameters are used to simulate the test run T089 (see Figure 5.25). Figure 5.23a demonstrates that E does not heavily influence this kind of simulation. Further studies show that choosing E to be near the physical value of the Young's Modulus of concrete does not influence the simulation result but lead to the necessity of much smaller times steps. This contradicts the purpose of this work to offer a fast, efficient, simplified model and simulation of the Attenuator barriers.

An initial observation is that all variations give excellent agreement with the test results for T092 and accurately predict the final position of the rock with a maximum error of +10%. While varying the reference angular orientation seems to have the most negligible influence (see Figure 5.23b), the proper choice of a suitable friction value strongly influences the simulation, as shown in Figure 5.22b. This sensitivity is expected as this experiment heavily depends on the rotation of the impacting object. The variation of the Young's Modulus in Figure 5.23a, as well as the variation of the coefficient of restitution in Figure 5.22a, show little influence, likely since the Attenuator barrier primarily retards via kinetic energy instead of strain energy.

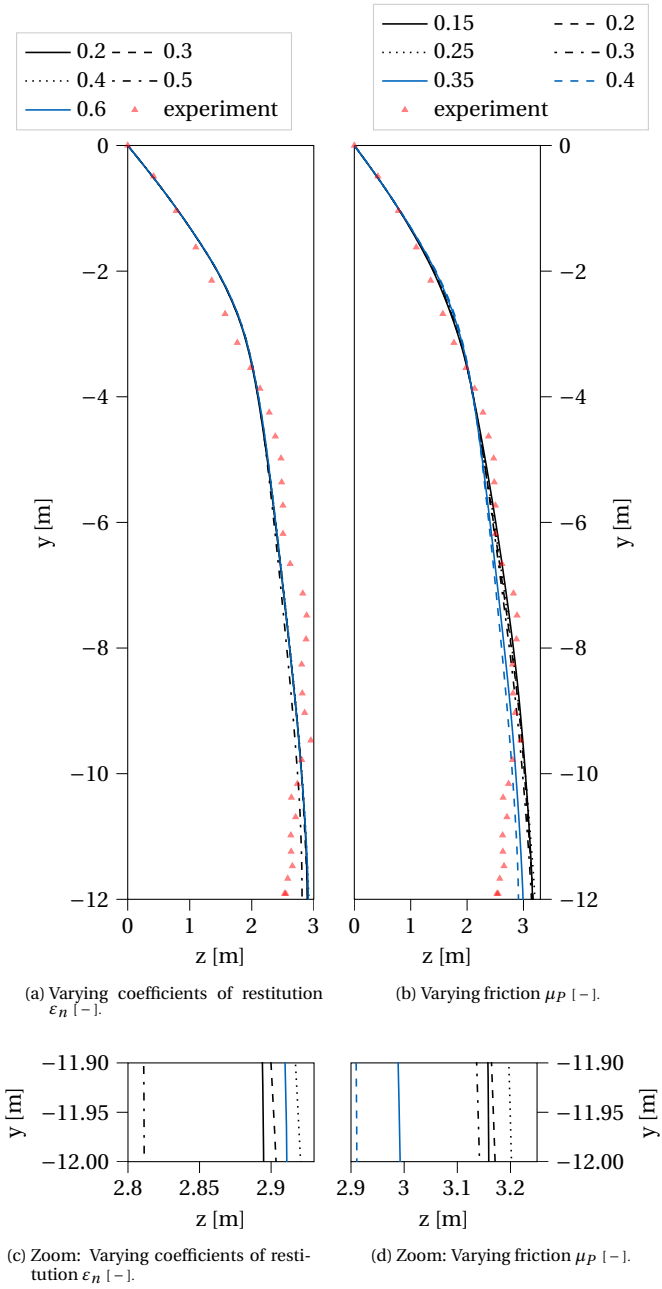

(a) Varying coefficients of restitution ε_n [−].

(b) Varying friction μ_P [−].

(c) Zoom: Varying coefficients of restitution ε_n [−].

(d) Zoom: Varying friction μ_P [−].

Figure 5.22: Visualization of object path T092 for varying input data, adapted from [103].

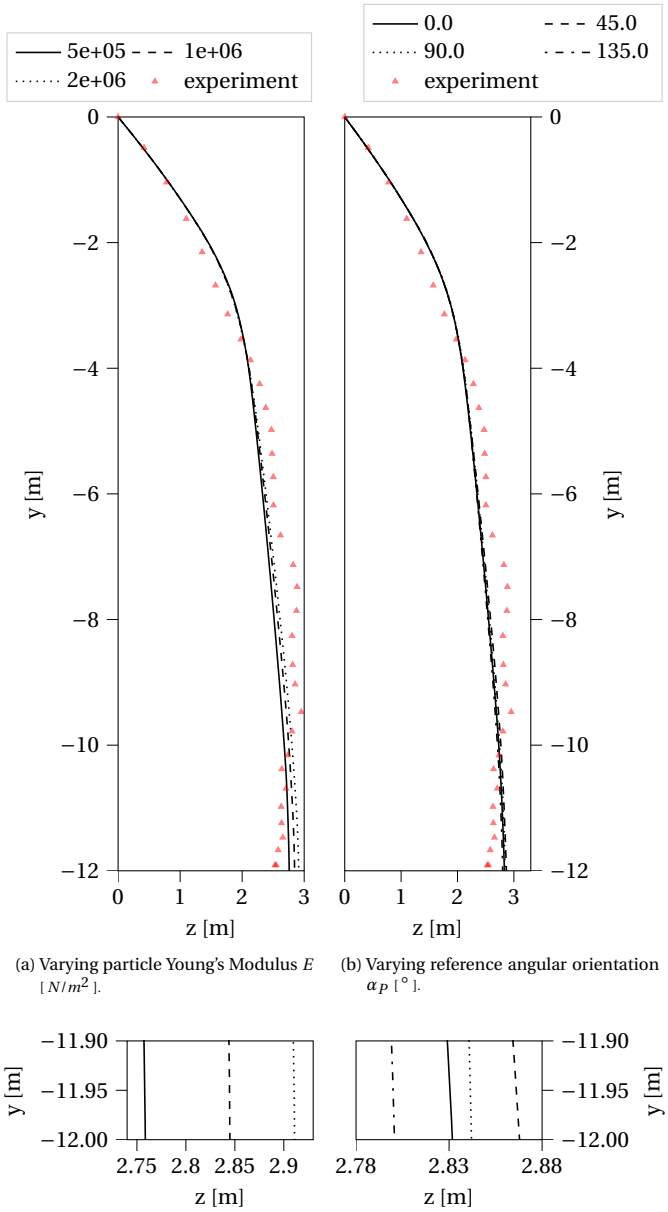

(a) Varying particle Young's Modulus E [N/m^2].

(b) Varying reference angular orientation α_P [°].

(c) Zoom: Varying particle Young's Modulus E [N/m^2].

(d) Zoom: Varying reference angular orientation α_P [°].

Figure 5.23: Visualization of object path T092 for varying input data, adapted from [103].

T092 - Most Suitable Parameter Sets

In the following, only the three best parameter variants for T092 are discussed, as the quality of the trajectories allows direct conclusions to be drawn about the correctness of the respective velocities. Therefore, the three optimal parameter combinations are presented in the following list, and their trajectories are visualized in Figure 5.24 together with the path of a free-falling object to demonstrate the efficacy of the Attenuator barrier.

Parameter set	A	B	C[†]
Friction μ_P [−]	0.4	0.4	0.4
Coefficient of restitution ε_n [−]	0.6	0.6	0.3
Young's Modulus $E\left[N/m^2\right]$	$1e6$	$2e6$	$2e6$
Reference angular orientation α_P [°]	146.25	146.25	45

Table 5.9: Parameters of the most suitable combinations for experiment T092.

The data obtained from the simulations is not only in strong accordance with the experiment results but also clearly demonstrates the effectiveness of the herein presented Attenuator barrier.

Remark: Calculation of Hazard Area - Free Fall

A rock at a height of $12m$ with an initial vertical velocity in gravity direction of $12.08m/s$ (as it is the case for T092) needs,

$$12.00m = 12.08\frac{m}{s}\cdot t + \frac{1}{2}\cdot \overbrace{9.81\frac{m}{s^2}}^{gravity}\cdot t^2 \qquad \longrightarrow \qquad t = 0.76s, \tag{5.2}$$

$0.76s$ to reach the ground. In combination with an initial horizontal velocity of $10.01m/s$ the rock travels a horizontal distance of $10.01\frac{m}{s}\cdot 0.76s \approx 7.6m$. This results in a potential hazard area that is approximately three times as large as for the protective installation as visualized in Figure 5.24.

[†] This is the most realistic parameter combination for the rock material for μ_P,ε_n.

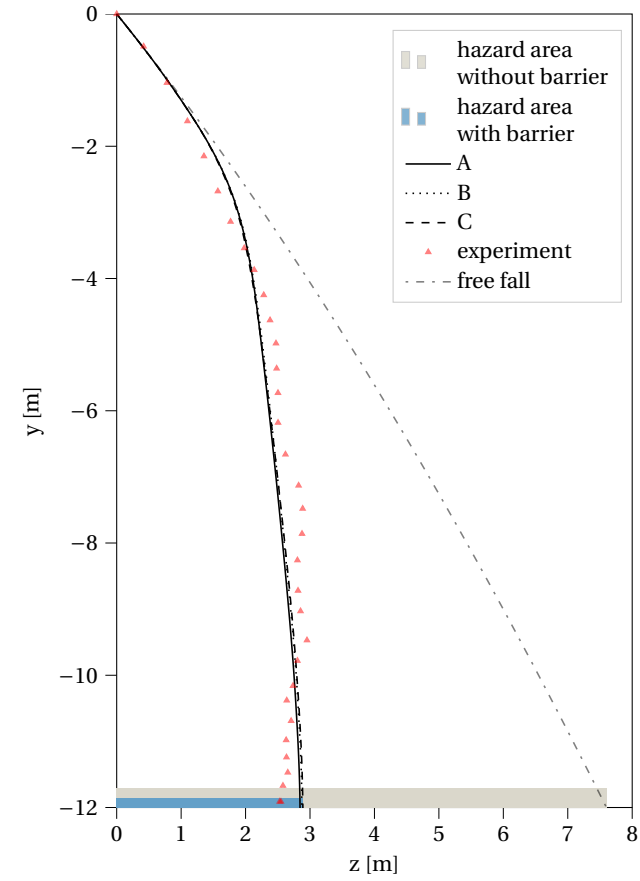

(a) Overview.

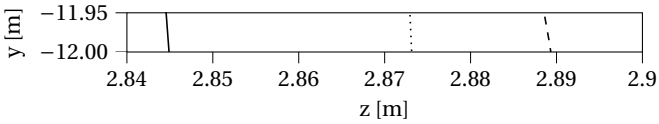

(b) Zoom.

Figure 5.24: Visualization of object path T092 and the three optimal parameter combinations (compare Table 5.9). Additionally, the free fall trajectory is added to demonstrate the correctness of the object path at the beginning of the simulation and the effectiveness of the Attenuator barrier. With the installation of the barrier the hazard area decreases by approximately 2/3, adapted from [103].

T089

Subsequently, another experiment is simulated to validate the previously found parameter combinations. The additional experiment uses the object T089, the data of which are given in Table 5.7. The results, which are shown in Figure 5.25, relate to the simulation of T089 with the parameter set C of T092 from Table 5.9. It shows that the experimental results are properly re-produced without any further need for parameter investigation. This ensures that this parameter set can recalculate other scenarios and creates confidence in the accuracy and applicability of the study presented here.

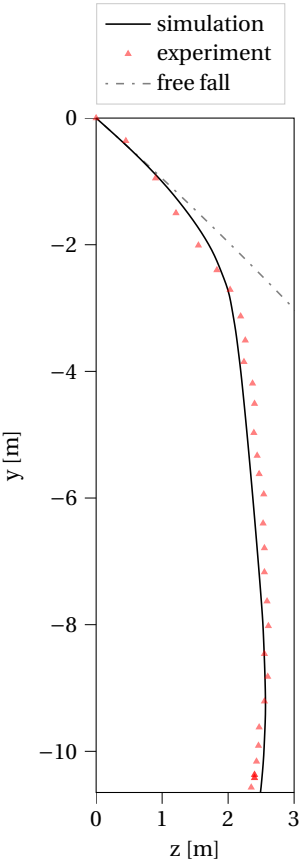

Figure 5.25: Visualization of object path T089 and the parameter set C as shown in Table 5.9, adapted from [103].

5.2.3.2 Angular Velocity

The experimental observations presented in Figure 5.27A illustrate the impacting object angularly decelerating and subsequently accelerating in the opposing angular direction. Unfortunately, the experimental data do not provide any information about the predominate rotation axis, the individual rotation components of each axis, or the rotational orientation of the specimen at the time of impact. Nevertheless, it is helpful to compare the general rotation behavior with the simulation results. Figure 5.27B illustrates that the simulation exhibits the same rotational trend as the experiment in Figure 5.27A. Additionally, Figure 5.26A visualizes the angular velocity about one of the principal axes of the impacting object, which clearly depicts the time in which the deceleration mentioned above and subsequent acceleration take place. The same behavior can be observed in Figure 5.26B, which depicts the general trend of the angular velocity obtained from the experiment.

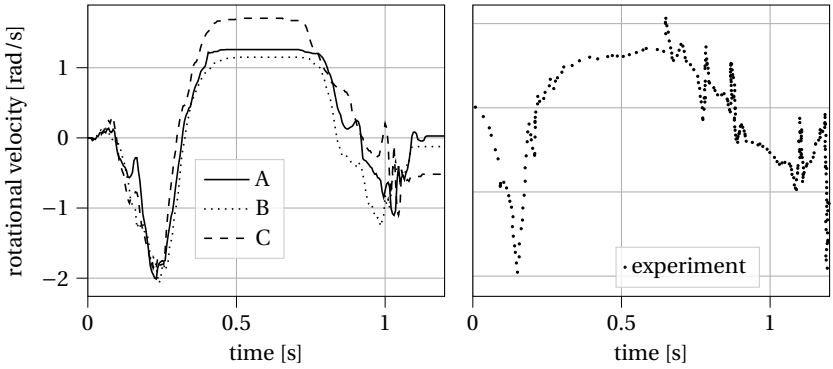

(a) Simulation.

(b) General trend from experiment.

Figure 5.26: Visualization of angular velocity about one of the main axis of the impacting object T092, adapted from [103].

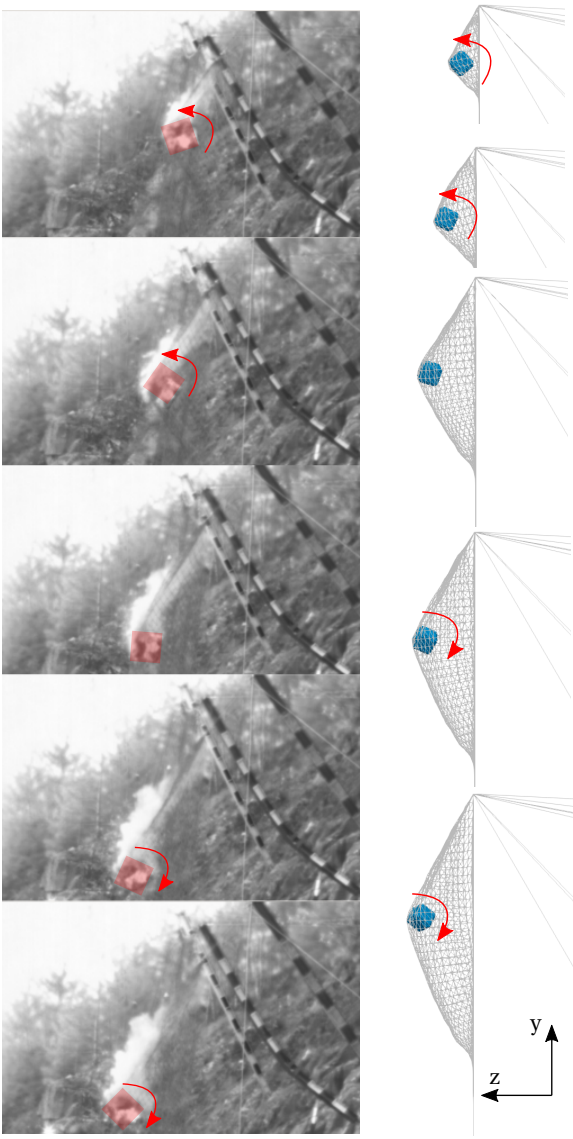

(a) Photographs of the experiment. (b) Simulation.

Figure 5.27: The test object impacts with a certain angular velocity, stops rotating, slides for a short time period and starts rotating in the opposite direction subsequently. All figures are adapted from [103].

5.2.3.3 Translational Velocity

The translational velocity of the three optimal parameter sets (as per subsection 5.2.3.1) and the experiment are illustrated in Figure 5.28a. It is noticeable that the deceleration of the impacting rock in the horizontal direction (perpendicular to the protection net) is accurately modeled by the simulation. This is particularly important for the design of protection structures since the management of horizontal momentum is the primary arresting mechanism. Although experimental results for the vertical (gravity) direction are substantially scattered, the simulation demonstrates a good agreement with the general trend of the experimental data.

Precisely as in subsection 5.2.3.1, the velocity components of the simulation and the experiment of T089 are also compared in the following. Figure 5.28b shows that these data could also be reproduced with an excellent agreement and thus allows applicable statements to be made about future rockfall events in Attenuator barriers.

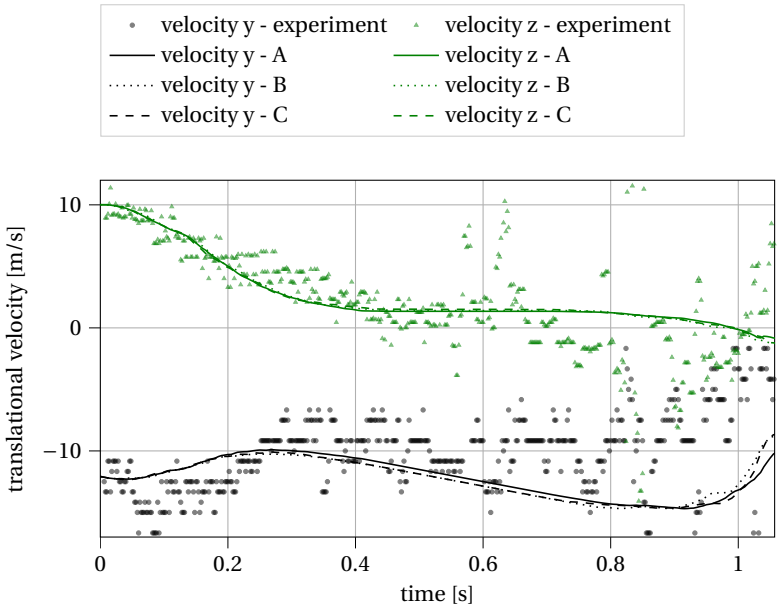

(a) The three optimal parameter combinations for T092 as shown in Table 5.9.

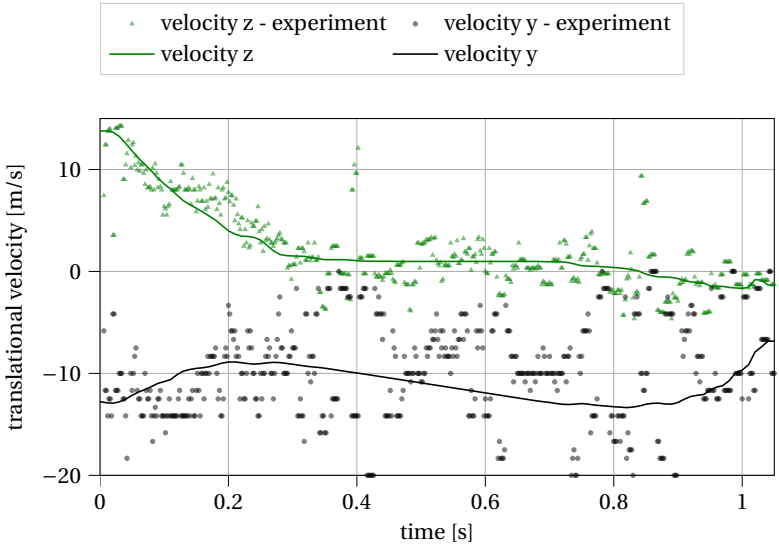

(b) T089 with parameter set C as shown in Table 5.9.

Figure 5.28: Comparison of translational velocity for both the horizontal direction, z and the vertical in gravity direction, y. All figures are adapted from [103].

CHAPTER 6

Inclusion of Terrain Data

So far, only the protective systems have been considered, and the impact positions and impact velocities have been specified. This procedure is beneficial if the impact location and velocity are known in advance or can be estimated easily. However, the exact impact positions and impact velocities are usually not known. Therefore it is helpful to determine these and analyze possible worst-case scenarios, including the surrounding terrain in the simulations. This chapter presents the advantages of this inclusion and shows how to realize it.

6.1 Workflow

The inclusion of terrain data allows the investigation of possible load scenarios. For example, the optimal position of the protective structure can be determined in preliminary studies. For this purpose, the DEM simulation without the protective structure is sufficient since, in this way, the trajectories of the rockfall can be simulated. The partitioned coupling method in this work additionally allows to integrate the FEM model of the protective structure into the terrain model and to cover the overall global model in this way. Figure 6.1 demonstrates the general procedure for the modeling. It starts with the production or the pure use of provided terrain data. These can be generated, for example, via drone images or laser surveys. Subsequently, the resulting point cloud is then transformed to a triangulated approximated surface. Following this, the surface can now be used as rigid boundary conditions in a pure DEM or coupled simulation. For this purpose, the FEM model of the protective structure is included in the terrain model at the appropriate location, and then the DEM particles or clusters representing the rocks are included. The further procedure corresponds to the simulation process presented in the previous chapters. The global model is then used to perform rockfall simulations. Figure 6.2 shows an example of the simulation of the completed model from Figure 6.1. Simple parameters and models are chosen for demonstration purposes. For example, the particles are perfect spheres, and the

protective structure is limited to the most necessary components. In addition, it is easy to see how the inclusion of the terrain data adds value to the overall simulation.

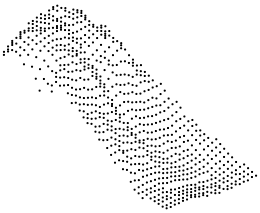

(a) A point cloud is created representing specific terrain coordinates.

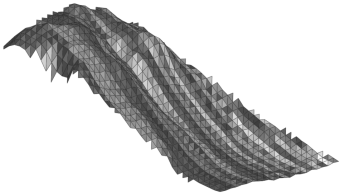

(b) The point cloud is used to create a triangulated surface approximation of the real terrain.

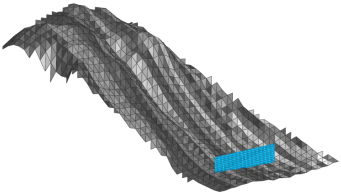

(c) The FEM model of the protection structure is included at the appropriate position in the terrain model.

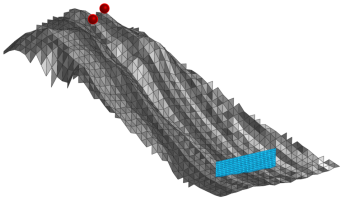

(d) Finally, the DEM model of the rocks is included. The final global model is successfully created.

Figure 6.1: Inclusion of terrain data in a coupled simulation. From point cloud to the final global model.

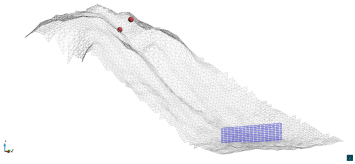

(a) $t = 1.2s$

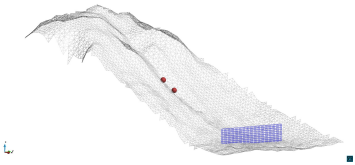

(b) $t = 4.5s$

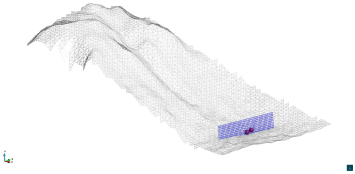

(c) $t = 6.8s$

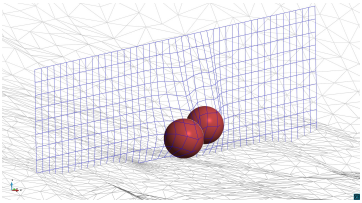

(d) Net impact, $t = 6.8s$

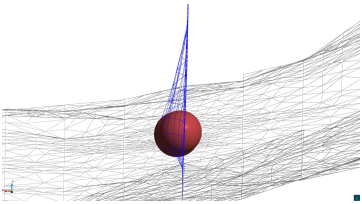

(e) Net impact - side view, $t = 6.8s$

Figure 6.2: Triangulated terrain model, showing the downward movement of the rocks, which are being slowed and stopped by the protection net [106].

6.2 Real World Terrain Data

For testing purposes, the Swiss company Geobrugg provided terrain data. These data are presented in Figure 6.3 and are used to show possible fields of application for the inclusion of terrain data.

- **Investigation of the Influence of the Rock Shape**
  Figure 6.3b shows the different trajectories for different rock shapes after detachment from the rock. The applying engineer can identify possible danger zones and plan accordingly.

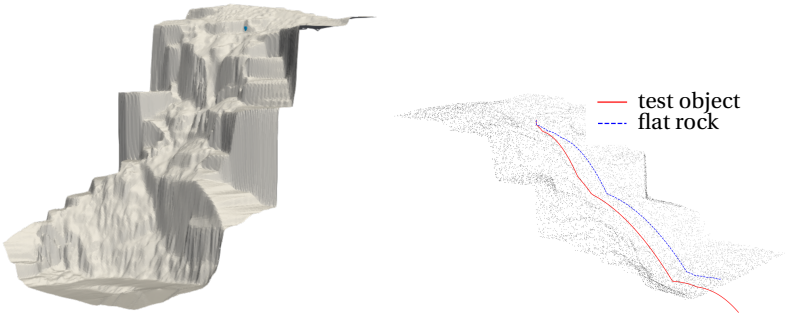

(a) Terrain Data with model of rock.

(b) Visualization the influence of the rock shape on the trajectories. The test object is used in section 5.1 and visualized in Figures 5.21a - 5.21b. The flat rock is depicted in Figure 6.4.

Figure 6.3: The terrain data in combination with different shapes of rocks can be used to investigate the influence of the worst position of dislocation as well as the influence of the shape of the rock, adapted from [101].

- **Tracing the Trajectories and Velocities**
  Figure 6.4 shows the entire path from detachment from the rock to impact the ground for a given rockfall. The simulation results provide additional information about the velocities of the rock during the fall. This allows a detailed study of the environmental influences on the rockfall.

- **Inclusion in Coupled Simulations**
  Finally, the terrain model can be included in a coupled DEM-FEM simulation workflow. For example, the attenuator from section 5.2.1 is simulated in Figure 6.5 including the surrounding terrain. This allows many different load scenarios to be run, and the protective structure no longer needs to be studied separately from the terrain.

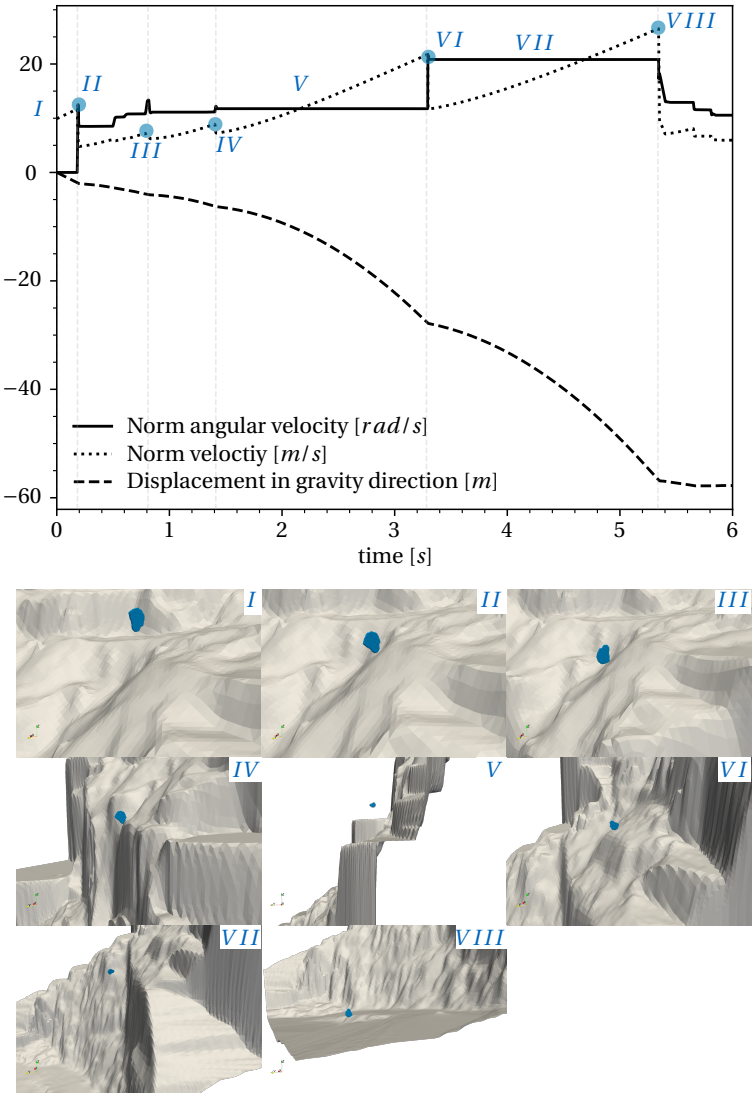

Figure 6.4: DEM simulation of an arbitrary rockfall including the terrain data. Blue dots in the graph indicate the time of contact with the rock face. A change in velocity is clearly visible at these times. A detailed study of the environmental influences on the rockfall is possible.

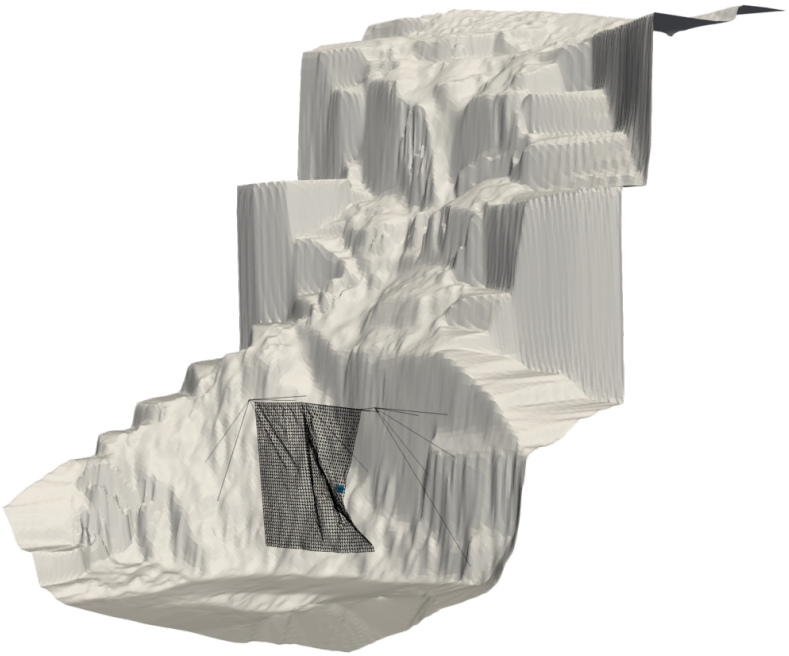

(a) Global view during the impact.

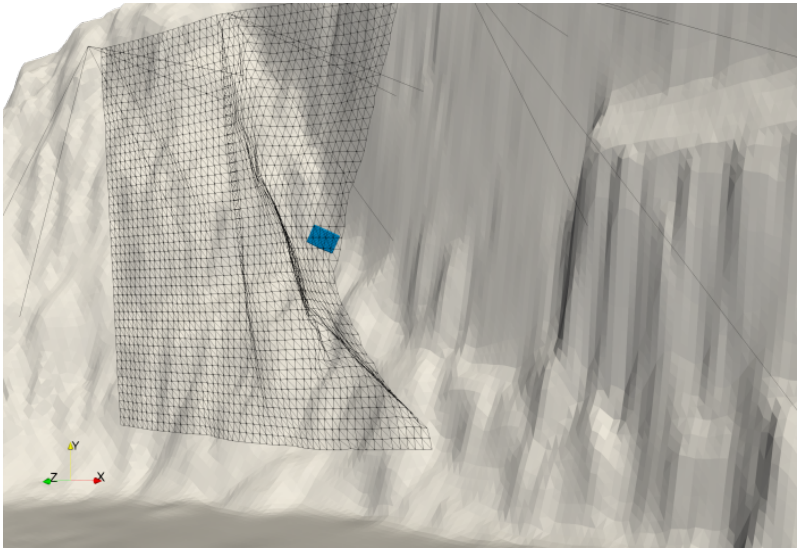

(b) Zoomed view during the impact.

Figure 6.5: Attenuator barrier from section 5.2.1 included in the terrain.

CHAPTER 7

Alternative Application Cases

In addition to rockfall and general natural, gravity driven hazardous events, the herein presented coupling procedure is suitable for a wide range of various application cases. For demonstration purposes two such scenarios are presented in the following:

- *Race track protection nets - car wheel impact in section 7.1.1*
- *Inflated cushion - head impact in section 7.1.2*

While proper values for the material parameters, such as Young's Modulus, density, and Poisson's ratio have been chosen, no comparison to experiments have been done. The purpose of the following chapters is simply to present the feasibility of the various scenarios. Data like impact velocity, location of impact and so on are chosen arbitrarily and are therefore not mentioned here.
In addition to the alternative use cases for DEM-FEM coupling, the coupling methodology of this work can be applied to other particle methods. This is illustrated by two examples:

- *Once, the Particle Finite Element Method (PFEM) is coupled with FEM to simulate a well-known benchmark Fluid-Structure Interaction (FSI) example in section 7.2.1.*
- *In addition, the Material Point Method (MPM) is coupled with the DEM to simulate the impact of a disruptive object into a continuum with large deformations, in section 7.2.2.*

Both examples have been developed during this dissertation in cooperation with collaborators or through thesis supervision.

7.1 DEM-FEM

While this work focuses on the simulation of rockfall protection systems, many other possible applications for the coupling of DEM and FEM are conceivable. In the following, two examples are presented. Since this is only a demonstration of potential applications, the modeling of exact material values and dimensions is omitted and, for this reason, not given.

7.1.1 Race Track Protection Nets - Car Wheel Impact

One conceivable application of the coupling of FEM and DEM is the simulation of protection meshes at the edge of race tracks. In the case of a collision of vehicles, individual parts, such as wheels, can detach from the vehicle and hit the safety nets with a high translational and rotational velocity. The construction of such protective nets is similar to that shown in Figure 7.1. A reinforced concrete foundation supports steel columns between which the protection net is stretched. Edge cables additionally hold the net in place.

To simulate this impact, potential contact surfaces must be defined as DEM walls. In the present case, it is the protection net but also the concrete foundation. This procedure is necessary because, after the impact, the wheel slides down into the net (Figure 7.2d) and finally finds contact with the concrete foundation (Figure 7.2f). The result is a strong braking of the wheel, as shown in Figure 7.2h.

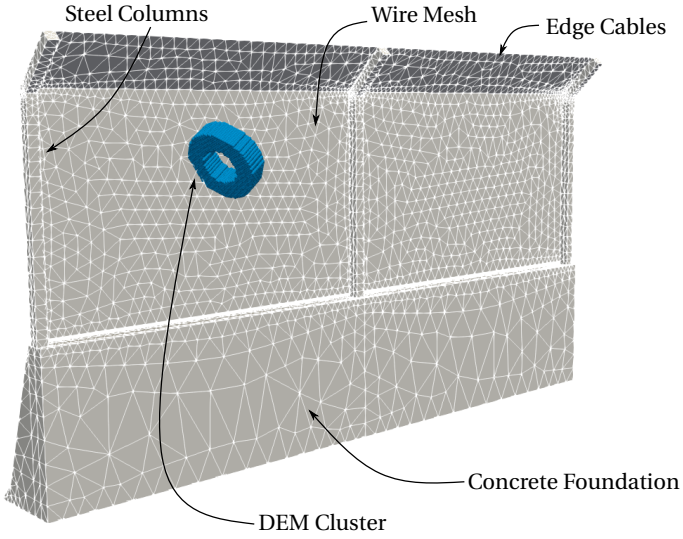

Figure 7.1: Reference setup of race track protection net and the impacting car wheel. A solid reinforced concrete foundation supports the steel columns. The wire mesh spans in between the steel columns and edge cables.

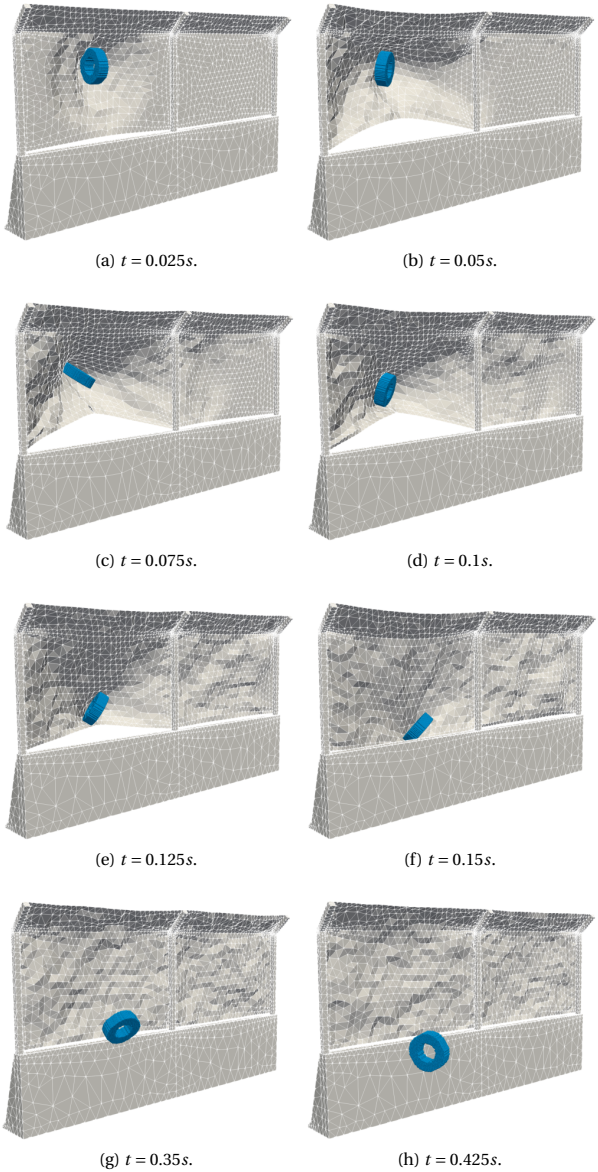

(a) $t = 0.025s$. (b) $t = 0.05s$.

(c) $t = 0.075s$. (d) $t = 0.1s$.

(e) $t = 0.125s$. (f) $t = 0.15s$.

(g) $t = 0.35s$. (h) $t = 0.425s$.

Figure 7.2: Impacting car wheel in protection net visualized over time.

7.1.2 Inflated Cushion - Head Impact

Another application of the presented coupling method is the simulation of an inflated cushion. Here, the cushion must be inflated and then withstand the impact of an object, usually a human head. The modeling and simulation of the inflation process has already been discussed in section 3.2.6.2. The resulting cushion model, presented in Figure 3.4b, is used in the following to simulate the impact of a head. This is approximated as usual by particle clusters and then guided into the cushion at a specified initial velocity. Figure 7.3 presents the reference configuration, while Figure 7.4 shows the impact sequence and the response of the cushion model. For a detailed view on the structural part, Figure 7.4d removes the cluster and applies a color scheme for the approximated displacement field.

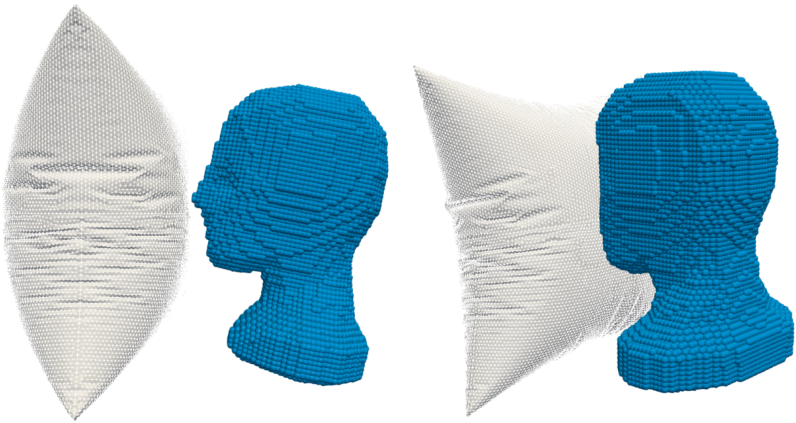

(a) (b)

Figure 7.3: Reference setup of an impacting human head on inflated cushion. The cushion has been simulated with plate in membrane action finite elements, while the head is approximated by a cluster of single spheres.

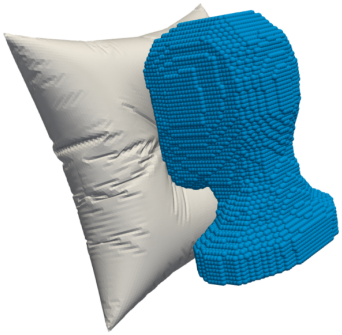

(a) $t = 0.05s$.

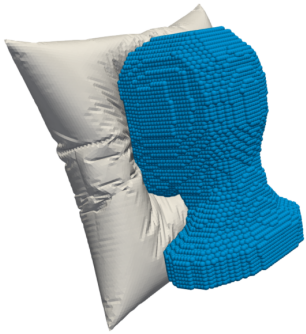

(b) $t = 0.1s$.

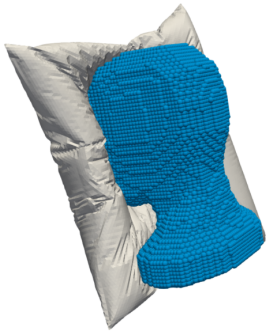

(c) $t = 0.15s$.

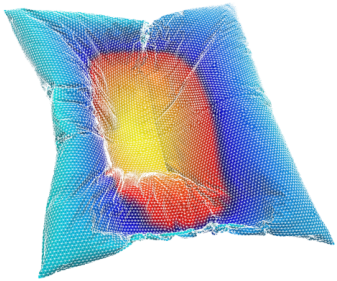

(d) $t = 0.15s$. Colored visualization of the finite element mesh deformation.

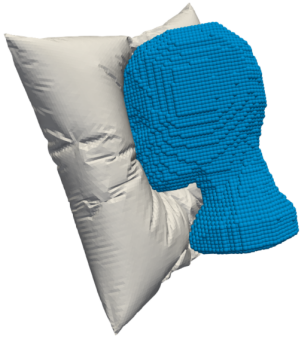

(e) $t = 0.35s$.

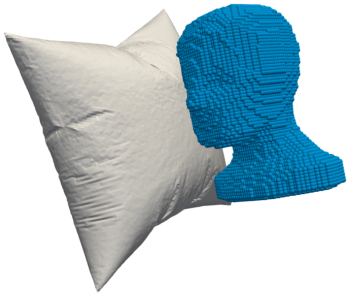

(f) $t = 0.485s$.

Figure 7.4: Impacting human head on an inflated cushion.

7.2 Other Particle Methods

The partitioned coupling method of this work can generally be extended to several other particle methods. The exchange of data and the sequential solution of the simulation participants are developed generically, so that only minor changes or additional conditions have to be introduced to exchange the DEM with other particle methods. In the following, two examples are presented that are developed in cooperation with colleagues and students. The examples are only briefly introduced, and the results and thus the possibilities are presented. References to the respective works are given and allow a detailed discussion of the content of the respective research topics.
It is explicitly stated here that the following two examples are only conducted in cooperation and not alone by the author.

7.2.1 PFEM-FEM: FSI

The PFEM was developed initially by [93]. It is a Lagrangian method and thus, unlike an Eulerian method, tracks material points in space. Unlike DEM, PFEM, like MPM, is not a mesh-free particle method and is continuum-based. The fluid volume to be modeled is triangulated, and the discrete mesh nodes subsequently represent the surrounding fluid, interpreted as particles. The fluid domain is remeshed if the mesh has deformed too much, to allow for large deformations. This is also the main drawback of the method. Especially in three-dimensional space, the repeated meshing of the fluid domain significantly lowers the performance.
In a master's thesis, the application of the coupling method to the combination PFEM-FEM was investigated. The master's thesis [48] was supervised and supported by the author of this thesis.

In the following, an example from the supervised master's thesis is presented to demonstrate the generic applicability of the coupling method to other particle methods. A FSI benchmark test is performed in which a dam break against a flexible wall is simulated in 2D. Figure 7.5 is adapted from [48] and depicts the simulation setup. The fluid is driven by gravity and impacts the flexible structural cantilever in the middle of the domain. The coupling method enables the successful simulation of this FSI problem. A comparison of the results to other publications is presented in Figure 7.6 and shows good agreement. Additionally, Figure 7.7 visualizes the time course of the simulation.

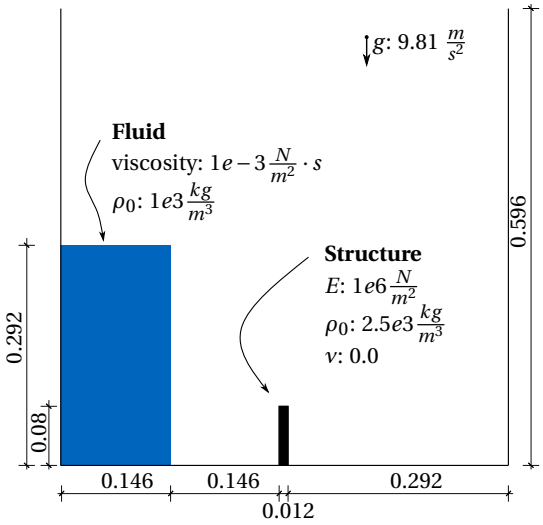

Figure 7.5: Simulation setup, adapted from [48]. Data is originally taken from [28]. Dimensions are given in meters [m].

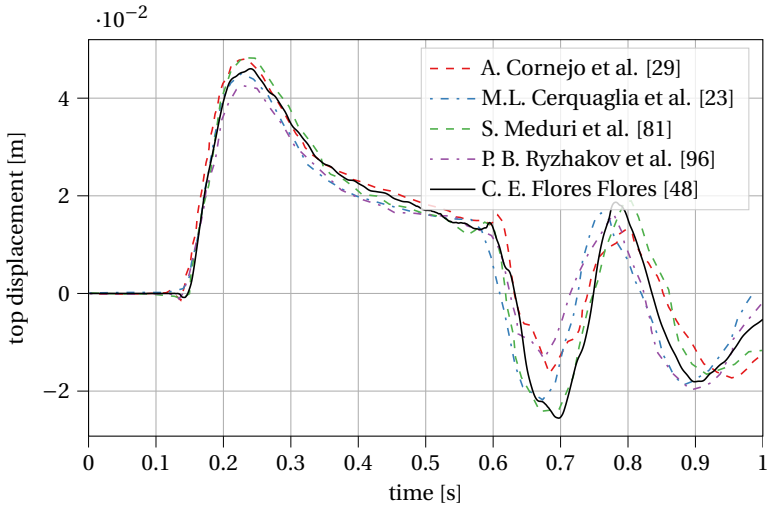

Figure 7.6: Figure adapted from [48]. The result of the horizontal tip displacement of the cantilever used for comparison with other publications.

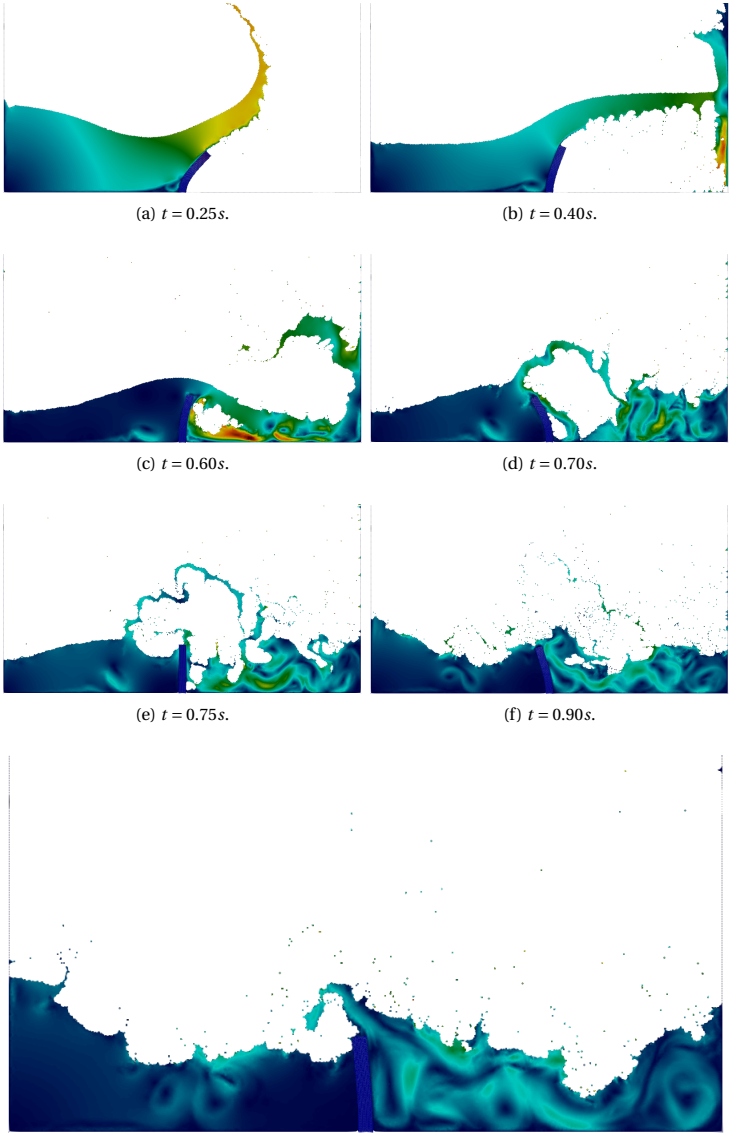

(a) $t = 0.25s$.

(b) $t = 0.40s$.

(c) $t = 0.60s$.

(d) $t = 0.70s$.

(e) $t = 0.75s$.

(f) $t = 0.90s$.

(g) $t = 1.00s$.

Figure 7.7: Time course of the PFEM-FEM FSI simulation. Simulation data are given in Figure 7.5 and results are presented in Figure 7.6. The results and figures were produced in [48] and presentation was kindly allowed by C. E. Flores Flores.

7.2.2 MPM-DEM

The cooperation with colleagues resulted in the further development of the presented coupling methodology to the application of MPM and DEM, which was mentioned in [111] for the first time. The present case is unique because two particle methods are coupled and the FEM is not part of the simulation. The MPM, as a successor of the Smoothed-Particle Hydrodynamics (SPH) [79], can represent large deformations by using a combination of the Lagrangian and the Eulerian formulation. Initially, particles are distributed in a background mesh, interpreted as material points. They serve as integration points and are updated in each step. The degrees of freedom are located on the discrete background nodes, which update the material nodes after the successful system solution and reset. Further literature is given in [46, 136].

In the following, the results of an impact simulation are shown. The DEM models the impacting object per cluster, and the MPM models the material that absorbs the impact. Detailed result data are deliberately not given here, and reference is made to [111] and further work based on it. The presentation of the results also serves to investigate potential further research topics. Figure 7.8 visualizes the simulation setup, while Figure 7.9 shows the results in chronological order.

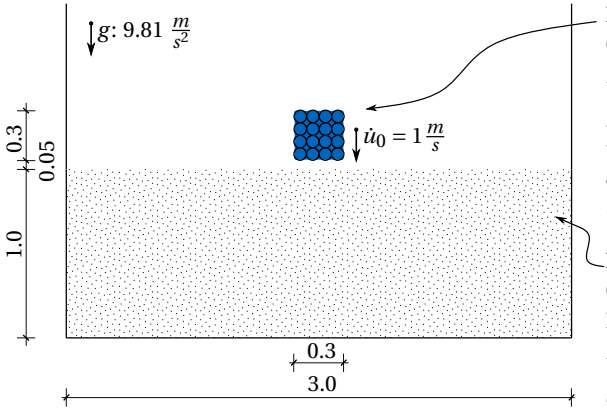

Figure 7.8: Simulation setup for impact of DEM cluster in MPM modeled material. Dimensions are given in meters $[m]$.

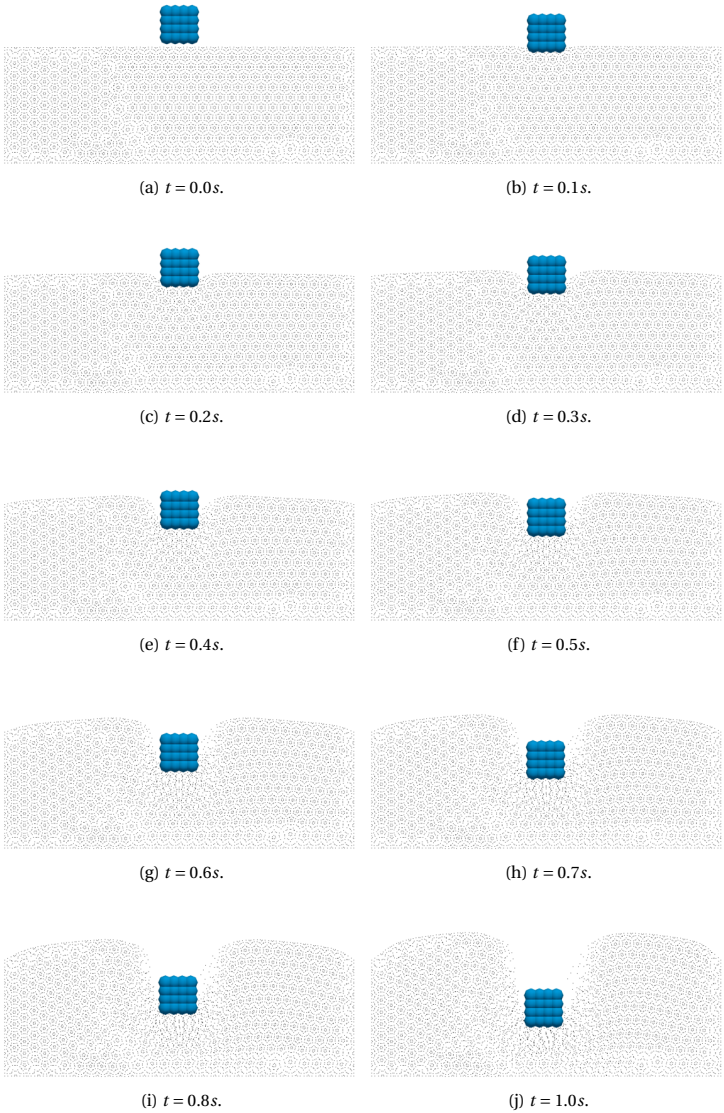

(a) $t = 0.0s$. (b) $t = 0.1s$.

(c) $t = 0.2s$. (d) $t = 0.3s$.

(e) $t = 0.4s$. (f) $t = 0.5s$.

(g) $t = 0.6s$. (h) $t = 0.7s$.

(i) $t = 0.8s$. (j) $t = 1.0s$.

Figure 7.9: Impacting DEM cluster in MPM material. Setup data is given in Figure 7.8.

CHAPTER 8

Software Implementation

The practical implementation of the presented simulation methodology is presented below. The modular simulation environment is discussed, and it is explained how the results of this dissertation can be integrated into the software environment. In addition, it is delineated which developments in the software environment have arisen as a direct result of this dissertation. Finally, this chapter shows the post and preprocessing possibilities.

The presented coupling methodology and all simulations were implemented in the open-source multi-physics software `Kratos`[*†] [33, 34, 47]. `Kratos` is structured so that a core provides the basics, such as base classes for elements, nodes, and geometries. On top of that, there is a layer of different applications that include different methods like FEM, PFEM, DEM, MPM, and many more. Due to this modular structure and the open-source character of the software, many different developers can further develop the software in different places. This is also the definite advantage of the presented coupling methodology. Furthermore, by the suitable treatment of a common interface, the different applications can be worked on separately and be coupled afterward partitioned.

[*] https://www.cimne.com/kratos/
[†] GitHub repository: https://github.com/KratosMultiphysics/Kratos

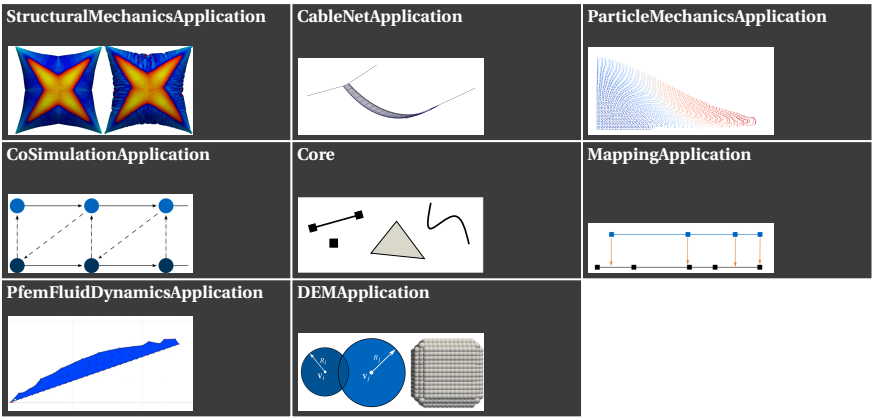

Figure 8.1: Modular overview of the most important KRATOS applications in this dissertation.

Utilizing a visualization of the most critical components for this dissertation, Figure 8.1 represents the individual modules:

- The *StructuralMechanicsApplication* includes essential structural elements, such as trusses, cables, beams, plate in membrane action, and shells. In addition, essential material laws and appropriate time integrators for the structure can be found here. In this work, the truss (section 3.2.7.1) and cable elements (section 3.2.7.2), the beam elements (section 3.2.7.5), and the plate in membrane action elements (section 3.2.7.4) were implemented. Also, plasticity laws (section 3.2.6.4) and hyper-elastic material laws (section 3.2.6.3) for one-dimensional structural elements were created. Furthermore, implementing a tension-field method (section 3.2.6.2) to account for wrinkling in membranes is also a result of this dissertation. Finally, a central-difference explicit time integration scheme (Appendix E.1) and a higher-order explicit time integration were implemented. In addition, an updated reference scheme has been implemented to allow the form-finding of structures carrying only normal forces [131].
- The *CableNetApplication* is entirely new in the context of this work. It offers space for unusual structural elements and special individual operations. For example, the sliding cable element (section 3.2.7.3) and its alternative modeling possibilities (Appendix C) can be found here. Further developments like ring elements [124] and chain-link elements [43] will find their place here in the future.
- In the *DEMApplication*, the DEM can be found. It provides different contact laws, time integrators, and particle models. At the beginning of this work, some adjustments were made to the contact search. Finally, to implement the strong coupling (section 4.5) between DEM and FEM, many changes in the code were necessary.

- The *ParticleMechanicsApplication* allowed the use of the MPM and was not further developed in the course of this work but only applied, which is presented in section 7.2.2.
- The *PfemFluidDynamicsApplication* contains the PFEM. Furthermore, as preliminary work to the already presented master's thesis [48], investigations on the possibility of a coupled simulation were carried out here, finally implemented in [48]. Section 7.2.1 presents the corresponding results.
- The *MappingApplication* allows the execution of mapping operations and thus represents an essential link in the partitioned coupling environment. It handles the data exchange at the interface of a partitioned coupled simulation, as discussed in section 4.3.
- Finally, the *CoSimulationApplication* represents the heart of a partitioned coupled environment. It handles the communication between the simulation participants and provides convergence accelerators like the Aitken method. The development of the *CoSimulationApplication* is described in [19].

The coupling of different numerical methods was initially done using custom `Python` scripts. These control the individual simulation participants via the provided `Python` interface, regulate the communication, and exchange data at the interface. After the *CoSimulationApplication* was developed and presented in [19], it was extensively used. Due to its implementation in `C++` and the thoroughly thought-out generic concept it offered a pleasant alternative to the custom `Python` scripts. However, the underlying theory is unchanged, and the coupling methodologies developed in sections 4.4 and 4.5 are applied.

The following three figures show how the modular coupling environment can be designed:

- Figure 8.2 describes how the rockfall simulations were performed in this dissertation. The DEM is coupled with the structural mechanic's application in conjunction with the *CableNetApplication* via the *CoSimulationApplication* and a suitable mapper.
- Figure 8.3 presents the modular implementation of the FSI PFEM-FEM simulation from section 7.2.1 .
- Figure 8.4 shows how the MPM and the DEM are brought together. See section 7.2.2.

Remark: Modular Representation

Even if the modular combination is shown significantly simplified at this point, it is pointed out that special operations at the interface are necessary for each coupling combination, which must be implemented in the program code first.

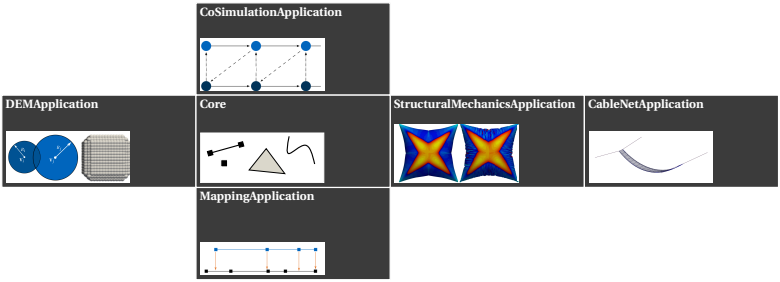

Figure 8.2: DEM-FEM coupling.

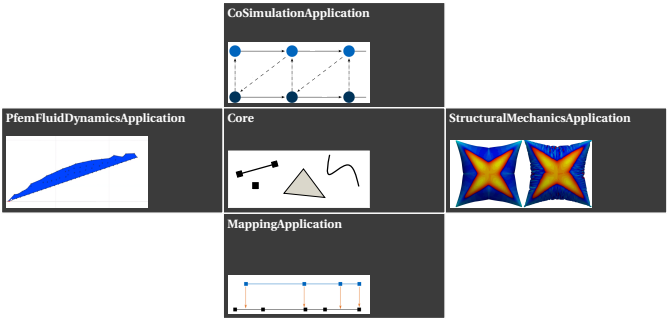

Figure 8.3: PFEM-FEM coupling. The example in section 7.2.1 uses this combination.

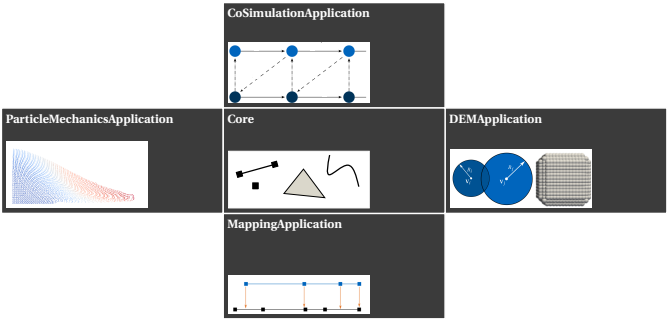

Figure 8.4: MPM-DEM coupling. The example in section 7.2.2 uses this combination.

Pre- and Postprocessing

The system input is made with the help of the pre- and postprocessing software GiD*. The GiD interface can be connected to the local Kratos code, and all features can be directly accessed. The partitioned coupling methodology in this work can be realized so that the structure is modeled as in Figure 8.5,

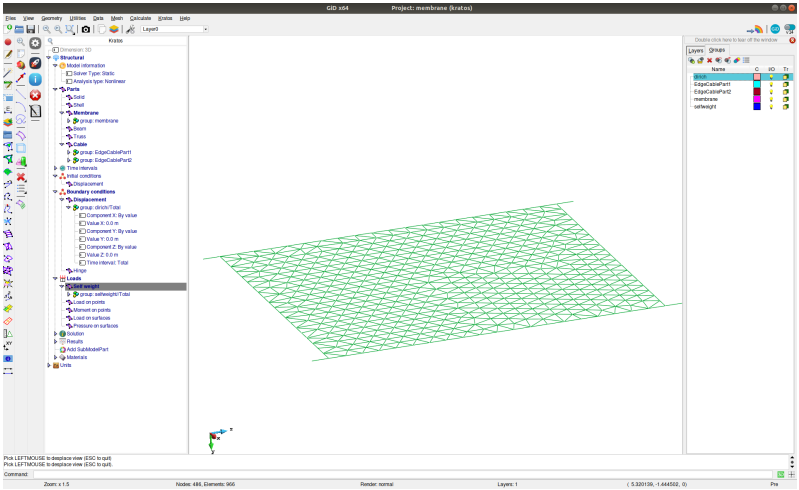

Figure 8.5: FEM preprocessing of the structural part in GiD.

and subsequently the DEM particles and wall condition as in Figure 8.6. GiD can then mesh both parts and generate the appropriate Kratos files.

Even though GiD can be used as a postprocessing tool, the postprocessing in this work is mainly done with ParaView†. ParaView stands out due to many possible settings and robust performance. Kratos allows the creation of vtk files with additional settings, which ParaView can read and visualize, as shown in Figure 8.7.

* https://www.gidhome.com/
† https://www.paraview.org/

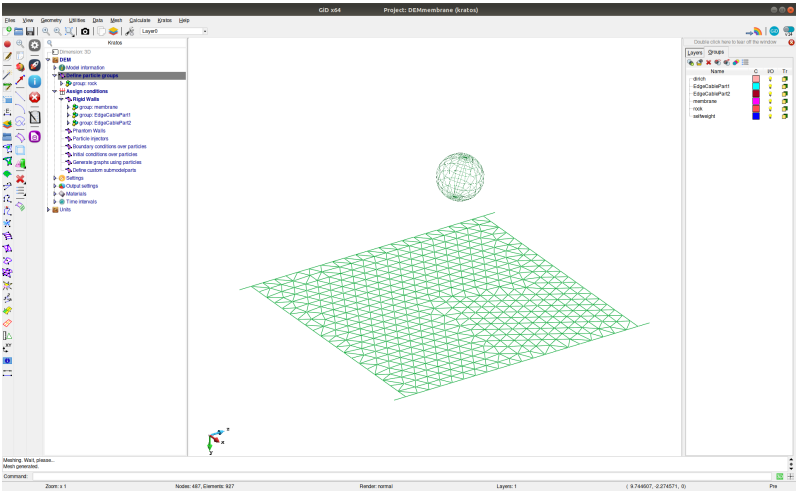

Figure 8.6: DEM preprocessing of the particles and the contact wall in GiD.

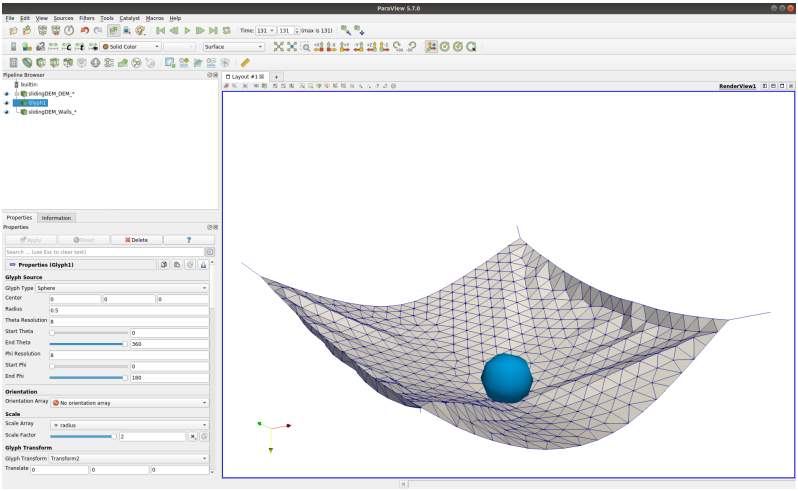

Figure 8.7: Postprocessing the simulation data in ParaView.

CHAPTER 9

Conclusions and Outlook

In this work, a partitioned simulation environment for rockfall analysis in structures was presented. Different numerical methods can be brought together within this environment to model the interaction of load and structural response. The DEM was coupled with the FEM with particular attention to rockfall. The DEM was used to calculate discrete particles' motion and contact forces, while the appropriate structural response was then calculated using the FEM.

Considering the highly complex flexible protective structures, many further developments in the FEM were necessary. Thus, unique structural elements were implemented, such as sliding cables and special material laws. Among them are hyper-elastic and plastic material laws for cables and trusses, anisotropic material laws for surface elements, and the appropriate treatment of wrinkling. All developments have been discussed in detail throughout this thesis. Further investigations were also necessary for the DEM. Appropriate contact laws and modeling of impacting rocks were investigated and are part of this dissertation.

Both methods were subsequently brought together in a partitioned coupling environment. The appropriate treatment of the common interface and the proper data exchange had to be investigated. Two coupling algorithms were then developed and closely examined. A weak coupling was further developed to a strong coupling based on a fixed point iteration with additional Aitken relaxation. Several validation examples were performed and are documented in this dissertation.

Finally, several real-scale experiments in the Swiss and Canadian mountains were analyzed in cooperation with the Swiss company Geobrugg. The data provided allowed the validation of the coupling method against actual values. The calculations are part of this dissertation and show excellent agreement between the simulations and the experiments, which gives confidence for the analysis of future projects.

Furthermore, the integration of terrain data was investigated, and the resulting potential for a global simulation solution was discussed in detail. The inclusion

of terrain data allows the consideration of the surrounding terrain and thus the analysis of possible worst-case scenarios.

The thesis concludes with a chapter on other possible use cases. There is much potential in the area of DEM-FEM coupling and the coupling of other numerical methods. In contrast to extensive rockfall simulations, the impact of a car wheel into a racetrack barrier net and the impact of a human head into an inflated cushion are presented via DEM-FEM coupling. The generic, modular application of the presented coupling method allows the combination of many different methods, finally represented by two examples. The PFEM-FEM coupling shows an FSI benchmark, and the MPM-DEM coupling presents the impact of a disruptive object into a continuum with large deformations.

This dissertation lays the foundation for an open-source solution that allows engineers to perform investigations of rockfall protection systems. Actual field tests should always accompany simulations of such large and complicated structures. The simulation does not claim to replace experiments but aims to serve as a helpful tool and an equal partner to experiments. Since field tests are costly and time-consuming, simulations help clarify detailed questions in advance. Thus, different design details can be investigated quickly and efficiently without performing a new test each time. In addition, it became apparent in this work that the simulations require careful tuning of the material parameters. This tuning can only be done by performing experiments in advance. Thus, added value is created by giving the engineer another tool to the experiments. The additional factor that the software and the developments of this work are freely available under an open-source license extends the application possibilities.

Now that this work has laid the framework for simulating the interaction of gravitational natural hazards and flexible protective structures, other interesting questions arise. Thanks to the partitioned coupling method, both the particle methods and the FEM can be processed and further developed separately and independently of each other.

Given is a list of engaging future research topics:

- Damage models for the structure and the influence of strain-rate-dependent material laws.
- Implementation of additional unique structural elements, such as the so-called chain-link elements [43].
- Structural optimization and sensitivity analysis of the protection nets.
- Optimization of the protective structure's position in the terrain.

APPENDIX **A**

Gradient of Virtual Displacement Field

Proof for,

$$\nabla \otimes \delta \mathbf{u} = \delta \mathbf{e}. \tag{A.1}$$

First the gradient of the virtual displacement field $\delta \mathbf{u}$ is calculated,

$$\nabla \otimes \delta \mathbf{u} = \frac{D(\delta \mathbf{u})}{D\mathbf{x}} = \frac{\partial (\delta \mathbf{x})}{\partial \mathbf{X}} \frac{\partial \mathbf{X}}{\partial \mathbf{x}} = \delta \left(\frac{\partial \mathbf{x}}{\partial \mathbf{X}} \right) \frac{\partial \mathbf{X}}{\partial \mathbf{x}} = \delta \boldsymbol{\mathcal{F}} \boldsymbol{\mathcal{F}}^{-1}. \tag{A.2}$$

To derive the virtual Euler-Almansi strain $\delta \mathbf{e}$ the virtual Green Lagrange strain $\delta \mathbf{E}$ is expressed,

$$\delta \mathbf{E} = \delta \left[\frac{1}{2} \left(\boldsymbol{\mathcal{F}}^T \boldsymbol{\mathcal{F}} - \mathbb{I} \right) \right] = \frac{1}{2} \left(\delta \boldsymbol{\mathcal{F}}^T \boldsymbol{\mathcal{F}} + \boldsymbol{\mathcal{F}}^T \delta \boldsymbol{\mathcal{F}} \right), \tag{A.3}$$

and finally pushed forward $\boldsymbol{\chi}(\bullet)^\flat$ with the following operation [61],

$$\begin{aligned} \delta \mathbf{e} = \boldsymbol{\chi} (\delta \mathbf{E})^\flat = \boldsymbol{\mathcal{F}}^{-T} (\delta \mathbf{E})^\flat \boldsymbol{\mathcal{F}}^{-1} = \boldsymbol{\mathcal{F}}^{-T} \frac{1}{2} \left(\delta \boldsymbol{\mathcal{F}}^T \boldsymbol{\mathcal{F}} + \boldsymbol{\mathcal{F}}^T \delta \boldsymbol{\mathcal{F}} \right) \boldsymbol{\mathcal{F}}^{-1} \\ = \frac{1}{2} \left(\boldsymbol{\mathcal{F}}^{-T} \delta \boldsymbol{\mathcal{F}}^T + \delta \boldsymbol{\mathcal{F}} \boldsymbol{\mathcal{F}}^{-1} \right) = \frac{1}{2} \left(\delta \boldsymbol{\mathcal{F}} \boldsymbol{\mathcal{F}}^{-1} + \delta \boldsymbol{\mathcal{F}} \boldsymbol{\mathcal{F}}^{-1} \right) \\ = \delta \boldsymbol{\mathcal{F}} \boldsymbol{\mathcal{F}}^{-1} = \nabla \otimes \delta \mathbf{u}. \end{aligned} \tag{A.4}$$

Remark: Lie Derivative

The concept of pull back, followed by a derivation in a constant reference frame and the subsequent push forward is called *Lie derivative* [6, 61].

APPENDIX **B**

Eigenvalue Problem: Principal Stresses

A short introduction to solve the eigenvalue problem with respect to principal stresses and its connection to the Lagrange-multiplier method is discussed in this subsection.

The principal stresses can be found by applying the Lagrange-multiplier method [61] to minimize/maximize the normal stresses*:

$$\begin{aligned} \text{Minimize the normal stress:} \quad & \mathbf{n}\cdot\mathbf{S}\mathbf{n}, \\ \text{such that:} \quad & 1-\mathbf{n}\cdot\mathbf{n}=0. \end{aligned} \tag{B.1}$$

Adding the function to be minimized and the constraint multiplied with a Lagrangian multiplier λ [123] a stationary point of the Lagrangian is derived:

$$L_\lambda = \mathbf{n}\cdot\mathbf{S}\mathbf{n} + \lambda\left(1-\mathbf{n}\cdot\mathbf{n}\right), \tag{B.2}$$

whose derivative must vanish to represent a stationary point:

$$\begin{aligned} \frac{\partial L_\lambda}{\partial \lambda} &= 1-\mathbf{n}\cdot\mathbf{n}=0, \\ \frac{\partial L_\lambda}{\partial \mathbf{n}} &= 2\left(\mathbf{S}\mathbf{n}-\lambda\mathbf{n}\right)=0. \end{aligned} \tag{B.3}$$

Equation B.3 can be rewritten to the well-known eigenvalue problem:

$$\left(\mathbf{S}-\mathbb{I}\lambda^{\#}\right)\mathbf{n}^{\#}=\mathbf{0}, \tag{B.4}$$

containing the eigenvalues $\lambda^{\#}$ - the principal stresses - and the corresponding eigenvectors $\mathbf{n}^{\#}$.

* Constraining $\mathbf{n}$ to be a unit vector.

APPENDIX C

Sliding Cable: Alternative Modeling Approaches

The sliding cable element formulation, discussed in subsection 3.2.7.3, represents an efficient way of handling the movement of sliding nodes along a given path. Other approaches are also possible and will be discussed in this section with respect to [102]. Each of the three methods was independently implemented and tested in `Kratos` [33, 34, 47]. In the end, the element formulation in subsection 3.2.7.3 proved to be the most robust and effective. Generally, however, the following two methods lend themselves to the problem at hand and can be applied to other problem setups. For this reason, they are discussed here.

C.1 Penalty Method

To realize the sliding with the help of the penalty method, additional terms are added to the internal energy which represent an energy representation of the distance l between an arbitrary node and the edge cable segment. By minimizing the total internal energy in the FEM solving process the distance l is minimized too. With respect to Figure C.1 the distance l can be calculated depending on the discrete nodal displacements $\hat{\mathbf{u}}$ of the points $\mathbf{n}_i$ as follows:

$$\begin{aligned} \mathbf{d} &= \mathbf{P}_2(\hat{\mathbf{u}}) - \mathbf{P}_1(\hat{\mathbf{u}}), \qquad \mathbf{r} = \mathbf{P}_3(\hat{\mathbf{u}}) - \mathbf{P}_1(\hat{\mathbf{u}}), \\ l(\hat{\mathbf{u}}) &= \frac{\| \mathbf{r} \times \mathbf{d} \|}{\| \mathbf{d} \|}, \qquad l^2(\hat{\mathbf{u}}) = \frac{(\mathbf{r} \times \mathbf{d}) \cdot (\mathbf{r} \times \mathbf{d})}{\mathbf{d} \cdot \mathbf{d}}. \end{aligned} \tag{C.1}$$

l^2 is now used to define a functional f which is similar to the energy description of a single spring element,

$$f(\hat{\mathbf{u}}) = \frac{1}{2} \cdot l^2(\hat{\mathbf{u}}) \cdot \alpha_{\mathrm{pf}}, \tag{C.2}$$

where α_{pf} represents the penalty factor which is highly problem dependent. By adding f to the total energy of the system, the following contributions to the internal forces $F_{\text{int},r}$ and the tangential stiffness matrix K_{rs} can be expressed, while r, s are two arbitrary degrees of freedom,

$$F_{\text{int},r} = \frac{\partial f}{\partial \hat{u}_r} = \alpha_{\text{pf}} \cdot \frac{\partial l}{\partial \hat{u}_r}, \qquad K_{rs} = \frac{\partial^2 f}{\partial \hat{u}_r \partial \hat{u}_s} = \alpha_{\text{pf}} \cdot \frac{\partial^2 l}{\partial \hat{u}_r \partial \hat{u}_s}. \tag{C.3}$$

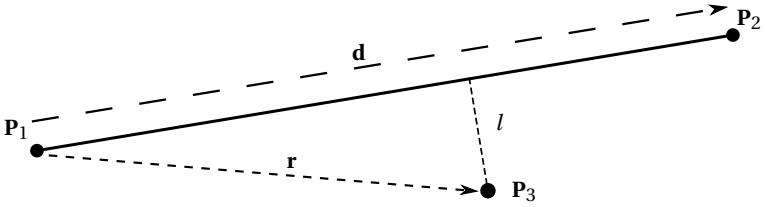

Figure C.1: Visualization of the geometric investigations to determine the distance l between an arbitrary node $\mathbf{P}_3$ and a line spanned between $\mathbf{P}_1$ and $\mathbf{P}_2$, adapted from [102].

Verification

A plane cable net, similar to Figure 3.10, is subjected to the impact of a sphere. For testing purposes the edge cables are discretized with standard cable elements and the sliding is achieved by applying the penalty method. The final results are shown in Figure C.2. It can be clearly seen, that there is a gap between the outer nodes and the edge cable. This is a result of the choice of the penalty factor α_{pf}. If it is chosen wrongly it can either lead to badly conditioned system matrices (α_{pf} is too large) or to a bad representation of the distance constraint (α_{pf} is too low). This drawback makes the penalty method inferior to the sliding cable formulation for the problem setup at hand.

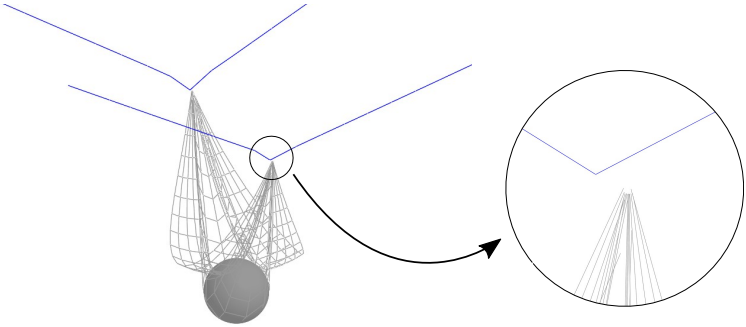

Figure C.2: Impact simulation with standard cable elements on the interior and along the edges. The sliding is realized via the penalty method. Adapted from [102].

C.2 Multi Point Constraint (MPC)

In contrast to the penalty approach, the Multi Point Constraint (MPC) approach aims to exactly reproduce the given constraint instead of approximating it. For this purpose a slave node and two master nodes are considered and their respective degrees of freedom are set in a specific relation. To obtain this relation the following Figure C.3 is used.

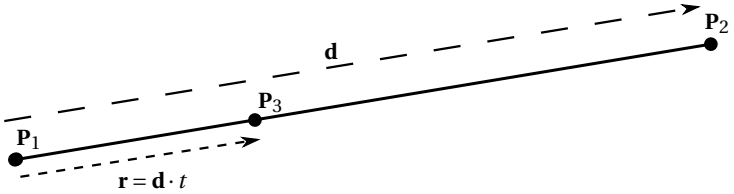

Figure C.3: Visualization of the geometric investigations to determine the movement of an arbitrary node $\mathbf{P}_3$ on a line segment spanned between the nodes $\mathbf{P}_1$ and $\mathbf{P}_2$, adapted from [102].

The slave node $\mathbf{P}_3$ is only allowed to move along the line between the master nodes $\mathbf{P}_1$ and $\mathbf{P}_2$. The three-dimensional line equation,

$$\begin{aligned} \mathbf{d}(\hat{\mathbf{u}}) &= \mathbf{P}_2(\hat{\mathbf{u}}) - \mathbf{P}_1(\hat{\mathbf{u}}), \\ \mathbf{r}(\hat{\mathbf{u}}) &= \mathbf{P}_3(\hat{\mathbf{u}}) - \mathbf{P}_1(\hat{\mathbf{u}}) = t \cdot \mathbf{d}(\hat{\mathbf{u}}), \end{aligned} \tag{C.4}$$

can be used to express the respective displacement relations with an arbitrary scalar value t,

$$t = r_x/d_x = r_y/d_y = r_z/d_z. \tag{C.5}$$

The further procedure is described below as an example for case $d_x \neq 0$ and only the discrete y-displacement $\hat{v}_3$, whereby case distinctions are necessary depending on the problem. First the relations between the displacements are expressed,

$$if \quad d_x \neq 0 \rightarrow \quad r_y = r_x \cdot \frac{d_y}{d_x} \quad \wedge \quad r_z = r_x \cdot \frac{d_z}{d_x}, \tag{C.6}$$

which allows the expression of the respective master-slave relations with the discrete x-displacement $\hat{u}$, y-displacement $\hat{v}$, and z-displacement $\hat{w}$,

$$\underbrace{\hat{v}_3}_{\text{slave}} = \hat{Y}_1 + \underbrace{\hat{v}_1}_{\text{master}} - \hat{Y}_3 + \left[\left(\hat{X}_3 + \underbrace{\hat{u}_3}_{\text{master}} - \hat{X}_1 - \underbrace{\hat{u}_1}_{\text{master}} \right) \cdot \frac{\hat{Y}_2 + \overbrace{\hat{v}_2}^{\text{master}} - \hat{Y}_1 - \overbrace{\hat{v}_1}^{\text{master}}}{\hat{X}_2 + \underbrace{\hat{u}_2}_{\text{master}} - \hat{X}_1 - \underbrace{\hat{u}_1}_{\text{master}}} \right]. \tag{C.7}$$

Obviously, equation C.7 is a non-linear constraint and in the following exemplarily linearized, while d_X, d_Y in equation C.8 are considered to be constant and given by the last time step,

$$d_X = \hat{X}_2 + \hat{u}_2 - \hat{X}_1 - \hat{u}_1, \quad d_Y = \hat{Y}_2 + \hat{v}_2 - \hat{Y}_1 - \hat{v}_1, \tag{C.8}$$

$$\begin{aligned} \underbrace{\hat{v}_3}_{\text{slave}_1} = \underbrace{\left(\hat{Y}_1 - \hat{Y}_3 + \frac{\hat{Y}_2 - \hat{Y}_1}{d_X} \cdot \left(\hat{X}_3 - \hat{X}_1 \right) \right)}_{\text{constant}} + \underbrace{\hat{v}_1}_{\text{master}_1} \cdot \underbrace{\left(1 + \frac{\hat{X}_1 - \hat{X}_3}{d_X} \right)}_{\text{weight}_1} + \underbrace{\hat{v}_2}_{\text{master}_2} \cdot \underbrace{\frac{\hat{X}_3 - \hat{X}_1}{d_X}}_{\text{weight}_2} \\ + \underbrace{\hat{u}_3}_{\text{master}_3} \cdot \underbrace{\frac{d_Y}{d_X}}_{\text{weight}_3} - \underbrace{\hat{u}_1}_{\text{master}_4} \cdot \underbrace{\frac{d_Y}{d_X}}_{\text{weight}_4}. \end{aligned} \tag{C.9}$$

Finally, after successfully declaring all proper constraints the system stiffness matrix $\mathbf{K}$ must be transformed by $\hat{\mathbf{K}} = \mathbf{\Lambda}^T \mathbf{K} \mathbf{\Lambda}$, with the help of $\mathbf{\Lambda}$ containing the constraint information. In the case of an explicit dynamic simulation, in which the accelerations are calculated as given in equation 3.33, the residual must be manipulated to $r_{master} = r_{master} + r_{slave} \cdot weight$.
The complexity of this method and the additional drawbacks shown in Table C.1 make this method again inferior to the sliding edge cable formulation for this problem.

C.3 Comparison

While all three presented methods allow the modeling of sliding nodes the sliding cable element formulation in section 3.2.7.3 proves to be the most efficient approach. No nearest neighbor search is necessary as the sliding nodes belong to the edge cable element. The following Table C.1 summarizes these findings and offers a comparison.

	Advantages +	Drawbacks -
Sliding Edge Element Formulation Section 3.2.7.3	Efficient handling of friction Easy incorporation into FE model No neighbor search Edge cable is only 1 element Constraint exactly enforced	Implementation of new element
Penalty Method Appendix C.1	No add. element implementation	Handling of friction Neighbor search Penalty factor Constraint only approximated
Multi Point Constraints Appendix C.2	No add. element implementation Constraint exactly enforced	Handling of friction Neighbor search Case-by-case analysis necessary Non-linear constraint

Table C.1: Advantages and drawbacks of three different methods to realize sliding along a given deformable cable element, adapted from [102].

APPENDIX **D**

Scalar Example: Fixed-Point Iteration with Aitken Relaxation

To demonstrate the operation of the Aitken relaxation method, a scalar equation is solved below using fixed-point iteration. The equation is chosen based on an example from the Internet[*]*.*

Figure D.1 shows that 29 iteration steps are necessary to solve the equation with an accuracy of $1e-6$ using a standard fixed-point iteration. However, if the Aitken method from equation 4.21 is used to relax the intermediate results of the fixed-point iteration, the maximum number of iteration steps is reduced to 5.

$$2 - x^2 - e^x = 0 \qquad \longmapsto x = \ln\left(2 - x^2\right). \tag{D.1}$$

The solution data for the fixed-point iteration with Aitken relaxation is given in Table D.1. One can observe the convergence of the Aitken relaxation factor α to a constant value ≈ 0.61. A small residual is reached already after 5 iterations.

Step	x	Residual	α
0	0.2		0.4
1	0.5589333185836889	4.7e-1	0.76
2	0.5337871330862051	3.6e-2	0.71
3	0.5372381242767222	5.7e-3	0.61
4	0.5372745099642543	5.9e-5	0.62
5	0.5372744491727965	9.9e-8	0.61

Table D.1: Solution data of fixed-point iteration with Aitken relaxation.

[*] https://de.wikipedia.org/wiki/Fixpunktiteration

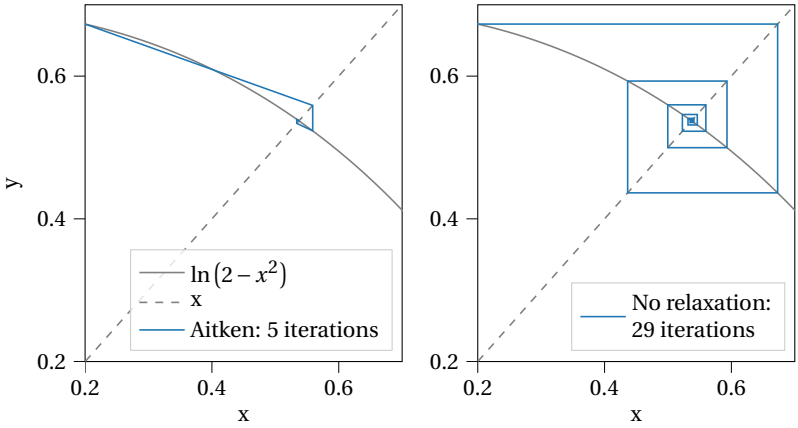

Figure D.1: Approximating the solution of equation D.1 with an accuracy of $1e-6$ to $x = 0.537274$. The standard fixed-point iteration needs 29 iterations, while only 5 are necessary if the Aitken method is used to relax the intermediate results.

APPENDIX E

Time Integration Algorithms

The two most important algorithms for time integration are briefly presented in the following sections. Finally, the update functions and references to further literature are given.

E.1 Explicit Time Integration: The Central Difference Method

An explicit time integration scheme is characterized by the fact, that every function for a given time step contains only derivatives of preceding time steps [8]. To derive the starting point for the central difference scheme, a Taylor's expansion of the displacement is set up and truncated for all terms of order larger than two. In the following equations, these terms will be called Higher Order Terms (H.O.T.).

$$\mathbf{u}^{t+\Delta t} \approx \mathbf{u}^t + \dot{\mathbf{u}}^t \Delta t + \frac{1}{2}\ddot{\mathbf{u}}^t \Delta t^2 + \cancel{H.O.T.}, \tag{E.1}$$

$$\mathbf{u}^{t-\Delta t} \approx \mathbf{u}^t - \dot{\mathbf{u}}^t \Delta t + \frac{1}{2}\ddot{\mathbf{u}}^t \Delta t^2 + \cancel{H.O.T.}. \tag{E.2}$$

$$\begin{aligned} \mathbf{u}^{t+\Delta t} + \mathbf{u}^{t-\Delta t} &= 2\mathbf{u}^t + \ddot{\mathbf{u}}^t \Delta t^2, \\ \longrightarrow \quad \ddot{\mathbf{u}}^t &= \left(\mathbf{u}^{t+\Delta t} - 2\mathbf{u}^t + \mathbf{u}^{t-\Delta t}\right)/\Delta t^2. \end{aligned} \tag{E.3}$$

[8] uses this formula to describe the central difference scheme, while [80] takes it as the starting point to derive the velocity verlet scheme.

Both describe the same procedure to update the new displacements and velocities for the next time step $t + \Delta t$:

1. $\dot{\mathbf{u}}^{t+\frac{\Delta t}{2}} = \dot{\mathbf{u}}^{t} + \frac{\Delta t}{2}\,\ddot{\mathbf{u}}^{t}$.
2. $\mathbf{u}^{t+\Delta t} = \mathbf{u}^{t} + \Delta t\,\dot{\mathbf{u}}^{t+\frac{\Delta t}{2}}$.
3. Update $\ddot{\mathbf{u}}^{t+\Delta t}$ with forces and inertias, via equation 3.33.
4. $\dot{\mathbf{u}}^{t+\Delta t} = \dot{\mathbf{u}}^{t+\frac{\Delta t}{2}} + \frac{\Delta t}{2}\,\ddot{\mathbf{u}}^{t+\Delta t}$.

E.2 Implicit Time Integration: The Generalized α-Method

The Generalized α-Method was developed by [26] and provides an efficient tool for solving structural dynamic problems. For completeness, the basic idea is described below using two update functions. More detailed information is given in [26].
Three new parameters $\alpha_m, \alpha_f, \beta_m$ are introduced that affect the way time integration works. They are used to update displacements and velocities based on current results and new acceleration values [26].

$$\mathbf{u}^{t+\Delta t} = \mathbf{u}^{t} + \Delta t\dot{\mathbf{u}}^{t} + \Delta t^{2}\left(\left(\frac{1}{2} - \beta_m\right)\ddot{\mathbf{u}}^{t} + \beta_m\ddot{\mathbf{u}}^{t+\Delta t}\right), \tag{E.4}$$

$$\dot{\mathbf{u}}^{t+\Delta t} = \dot{\mathbf{u}}^{t} + \Delta t\left(\left(\frac{1}{2} + \alpha_m - \alpha_f\right)\ddot{\mathbf{u}}^{t} + \left(\frac{1}{2} - \alpha_m + \alpha_f\right)\ddot{\mathbf{u}}^{t+\Delta t}\right). \tag{E.5}$$

The update of the displacements and velocities can be used to re-write equation 3.33 in terms of only the accelerations. The reformulation of the dynamic equilibrium is then used to solve the system of equations. With the newly obtained acceleration values the displacements and velocities can be calculated by equation 3.33.

APPENDIX **F**

DEM Contact Force Calculation

The calculation of the DEM contact forces needs several steps. First, geometric operations must be performed, and finally, the contact forces are derived from the chosen rheological model. A Hertz Mindlin Spring Dashpot Model (HM+D) model is chosen in this work and introduced in this section. Additionally, an overview of the necessary geometric operations and a discussion of the proper calculation of the damping coefficient and its history are given. The subsequent section follows closely [106], which is inspired by [98], and provides all necessary information to allow an independent implementation of the contact forces.

A detailed description of the evaluation of forces described in section 3.3.3 is provided in order to further discuss the necessary quantities in the underlying coupling scheme. As soon as contact is detected, the forces can be evaluated using various contact laws and rheological models in which the normal indentation δ_n, its time derivative $\dot{\delta_n}$, the normal vector $\mathbf{n}_c^{ij}$ at the contact point, as well as the increment of tangential displacement Δs are used [98].
The normal indentation δ_n is calculated with respect to equation F.1 and is graphically described in Figure F.1. Naturally, all tensors represent discrete values in the DEM.

$$\delta_n = R_i + R_j - \left(\mathbf{V}_j - \mathbf{V}_i\right) \cdot \mathbf{n}_c^{ij}, \qquad \text{with} \quad \mathbf{n}_c^{ij} = \frac{\mathbf{V}_j - \mathbf{V}_i}{\|\mathbf{V}_j - \mathbf{V}_i\|}. \tag{F.1}$$

In order to obtain Δs, the tangent unit vector $\mathbf{t}_c^{ij}$ must be derived by splitting the velocity at the contact point $\dot{\mathbf{u}}_c^{ij}$ into normal $\dot{\mathbf{u}}_{c,n}^{ij}$ and tangential $\dot{\mathbf{u}}_{c,t}^{ij}$ components.

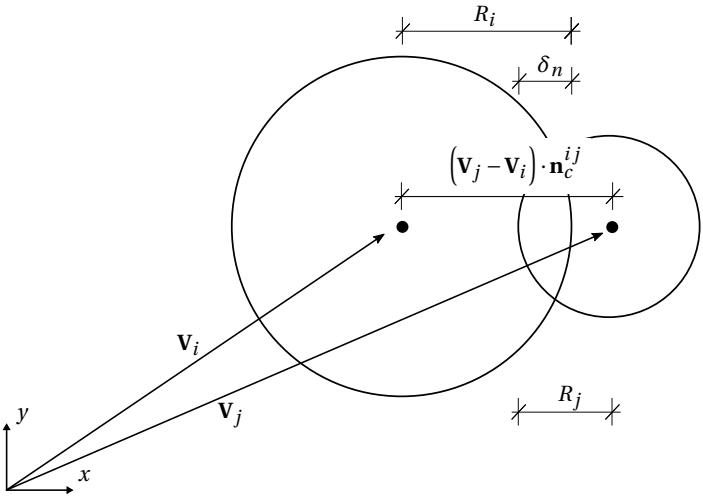

Figure F.1: Calculating the indentation $\delta_n = R_i + R_j - \left(\mathbf{V}_j - \mathbf{V}_i\right) \cdot \mathbf{n}_c^{ij}$.

First, the contact point velocity is expressed with the aid of the respective element velocity $\dot{\mathbf{u}}_i$, element angular velocity $\dot{\boldsymbol{\omega}}_i$, and the vector $\mathbf{r}_c^{ij}$ connecting the particle center and the contact point.

$$\dot{\mathbf{u}}_c^{ij} = \left(\dot{\boldsymbol{\omega}}_j \times \mathbf{r}_c^{ji} + \dot{\mathbf{u}}_j\right) - \left(\dot{\boldsymbol{\omega}}_i \times \mathbf{r}_c^{ij} + \dot{\mathbf{u}}_i\right). \tag{F.2}$$

$\dot{\mathbf{u}}_c^{ij}$ is subsequently split into the normal and the tangential direction,

$$\dot{\mathbf{u}}_{c,n}^{ij} = \left(\dot{\mathbf{u}}_c^{ij} \cdot \mathbf{n}_c^{ij}\right) \mathbf{n}_c^{ij}, \qquad \dot{\mathbf{u}}_{c,t}^{ij} = \dot{\mathbf{u}}_c^{ij} - \dot{\mathbf{u}}_{c,n}^{ij}. \tag{F.3}$$

This allows the expression of Δs using the tangent unit vector, the element displacement $\mathbf{u}_i$ and the element rotation vector $\boldsymbol{\omega}_i$, by projecting $\mathbf{u}^{ij}$ on $\mathbf{t}_c^{ij}$. Δs is an incremental value, based on the time step n.

$$\Delta s^{n+1} = \left(\mathbf{u}^{ij} \cdot \mathbf{t}_c^{ij}\right)^{n+1} - \left(\mathbf{u}^{ij} \cdot \mathbf{t}_c^{ij}\right)^{n}, \qquad \mathbf{t}_c^{ij} = \frac{\dot{\mathbf{u}}_{c,t}^{ij}}{\|\dot{\mathbf{u}}_{c,t}^{ij}\|},$$
$$\mathbf{u}^{ij} = \left(\boldsymbol{\omega}_j \times \mathbf{r}_c^{ji} + \mathbf{u}_j\right) - \left(\boldsymbol{\omega}_i \times \mathbf{r}_c^{ij} + \mathbf{u}_i\right). \tag{F.4}$$

For a Hertz-Mindlin spring dashpot contact model (denominated as HM+D in [31]), as shown in Figure F.2a and Figure F.2b, the normal forces F_n and tangential contact forces F_t are calculated for the case of two spheres colliding. Equation F.5 applies the normal and tangential stiffness k_n and k_t, respectively, and the

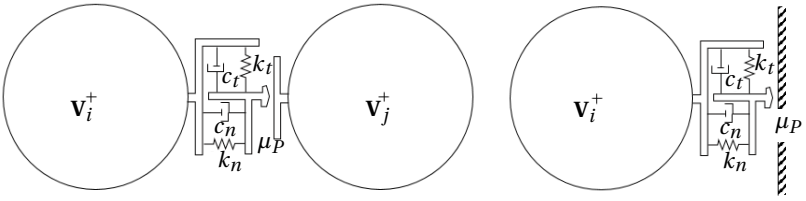

(a) DEM-DEM, adapted from [98]. (b) DEM-FEM, adapted from [98].

Figure F.2: DEM-DEM and DEM-FEM HM+D rheological models, adapted from [98, 106].

damping coefficients c_n and c_t [98], considering the maximum tangential force restricted to the Coulomb's friction* limit [31] by the coefficient of friction μ_P. The tangential forces are consequently updated from the last time step†, indicated by the superscript n.

$$\begin{aligned} F_n &= k_n \delta_n + c_n \dot{\delta_n}, \\ F_t^{n+1} &= \min\left[F_{te}^{n+1} + c_t \parallel \dot{\mathbf{u}}_{c,t}^{ij} \parallel, \quad \mu_P F_n \right], \\ F_{te}^{n+1} &= F_{te}^{n} + k_t^{n+1} \Delta s^{n+1} \quad \text{if} \quad \Delta F_n \geq 0, \\ F_{te}^{n+1} &= F_{te}^{n} \frac{k_t^{n+1}}{k_t^n} + k_t^{n+1} \Delta s^{n+1} \quad \text{if} \quad \Delta F_n < 0. \end{aligned} \tag{F.5}$$

	sphere i - sphere j	sphere i - wall j
$k_n =$	$\frac{4}{3\left(\frac{1-\nu_i^2}{E_i}+\frac{1-\nu_j^2}{E_j}\right)}\sqrt{\frac{R_i R_j}{R_i+R_j}\delta_n}$	$\frac{4}{3\left(\frac{1-\nu_i^2}{E_i}+\frac{1-\nu_j^2}{E_j}\right)}\sqrt{R_i \delta_n}$
$k_t =$	$\frac{8}{\frac{2-\nu_i}{G_i}+\frac{2-\nu_j}{G_j}}\sqrt{\frac{R_i R_j}{R_i+R_j}\delta_n}$	$\frac{8G_i}{2-\nu_i}\sqrt{R_i \delta_n}$
$c_n =$	$2\frac{\varsigma_i+\varsigma_j}{2}\sqrt{\frac{m_i m_j}{m_i+m_j}k_n}$	$2\varsigma_i\sqrt{m_i k_n}$
$c_t =$	$2\frac{\varsigma_i+\varsigma_j}{2}\sqrt{\frac{m_i m_j}{m_i+m_j}k_t}$	$2\varsigma_i\sqrt{m_i k_t}$

Table F.1: Stiffness and damping values for sphere-sphere and sphere-wall contact [98].

* Dry friction [80].
† Updated from the last iteration for strong coupling.

The material parameters in Table F.1 (Young's modulus E, particle mass m, shear modulus G, and Poisson's ratio ν) are typically obtained by calibration from experiments [27].

F.1 The Coefficient of Restitution (COR)

As a scaling factor in Table F.1 the dashpot coefficient ς is frequently expressed using the normal coefficient of restitution (COR) ε_n, as shown in equation F.6,

$$\varepsilon_n = -\dot{\delta_n}^f / \dot{\delta_n}^i. \tag{F.6}$$

ε_n relates the initial impact velocity $\dot{\delta_n}^i$ to the final velocity at the end of the contact $\dot{\delta_n}^f$. A maximum of $\varepsilon_n = 1.0$ will model a perfectly elastic impact whereas $\varepsilon_n = 0.0$ models a perfectly plastic impact. Equation F.5 demonstrates, that a smaller ε_n increases the influence of the impact velocity in the contact force calculation [31, 98] and is thus critical for the coupled simulation in this work.
While many publications discuss the derivation of the appropriate ε_n for rockfalls, they always consider the impact on a rigid ground. Many aspects influence the proper ε_n, such as the angle of impact, the material of the rock and the ground, the rock mass, and the impact velocity. [5] gives a literature review of available scaling methods, and [24] conducts experiments to analyze the correct ε_n, including rotational impact. More investigations and experiments are described in [97, 133]. Although these publications give a detailed explanation of ε_n for the impact of rocks on rigid grounds, no discussion about the impact on flexible, deformable structures is available. Thus ε_n, as a material parameter, needs to be tuned for the given problem setup. The simulations of real-world structures in section 5.1 and 5.2 demonstrate the necessity of the parameter tuning.

F.2 The Dashpot Coefficient

To derive the correct dashpot coefficient ς, a scalar equation of motion needs to be solved. For demonstration purposes a simple model with a mass m, a linear spring k, a damping coefficient c, and a linear dashpot ς (LS+D) is chosen:

$$m\ddot{\delta_n} + c\dot{\delta_n} + k\delta_n = \ddot{\delta_n} + 2\varsigma\sqrt{\frac{k}{m}}\dot{\delta_n} + \frac{k}{m}\delta_n = 0. \tag{F.7}$$

[108] originally derived ς for a LS+D model from equation F.7 by considering the contact to end as soon as the indentation is zero ($\delta_n = 0$). Equation F.8 is the result of this consideration and has been extensively used.

$$\varsigma = \frac{-\ln \varepsilon_n}{\sqrt{\pi^2 + \ln^2 \varepsilon_n}}. \tag{F.8}$$

However, it has been shown by [31, 107, 120] that this idea leads to artificial attracting forces during the contact*. [120] proposes an alternative approach by calculating $\dot{\delta_n}^f$ at the time the accelerations† reach the value zero ($\ddot{\delta_n} = 0$).
For the HM+D model, used in this work, [120]'s approach results in the following equation for ς,

$$\varsigma = \sqrt{\frac{1.0}{1.0 - (1.0 + \varepsilon_n)^2 \cdot e^H} - 1.0}, \tag{F.9}$$

$$\begin{aligned} H = \varepsilon_n \cdot (h_1 + \varepsilon_n \cdot (h_2 + \varepsilon_n \cdot (h_3 + \varepsilon_n \cdot (h_4 + \varepsilon_n \cdot (h_5 \\ + \varepsilon_n \cdot (h_6 + \varepsilon_n \cdot (h_7 + \varepsilon_n \cdot (h_8 + \varepsilon_n \cdot (h_9 + \varepsilon_n \cdot h_{10}))))))))). \end{aligned} \tag{F.10}$$

i	1	2	3	4	5
h_i	-6.918798	-16.41105	146.8049	-796.4559	2928.711

Table F.2: h_i values for equation F.10 [120].

i	6	7	8	9	10
h_i	-7206.864	11494.29	-11342.18	6276.757	-1489.915

Table F.3: h_i values for equation F.10 [120].

A comparison of both approaches is repeated in Table F.4, and Figure F.3 depicts the different functions.

Source	Condition for contact end
[108]	$\delta_n = 0$
[31, 107, 120]	$\ddot{\delta_n} = 0$

Table F.4: Conditions for contact end with respect to different sources.

* For frictional cohesionless contact, as used in this work, the normal force must be constrained always to be ≥ 0 [98], since no traction in normal direction is allowed. The contact is purely repulsive.
† And thus the forces.

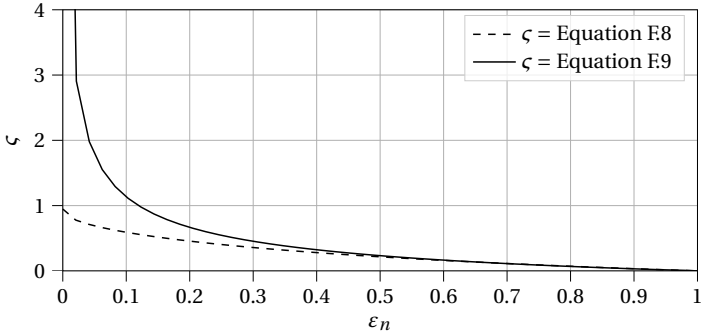

Figure F.3: Damping coefficient $\varsigma(\varepsilon_n)$, see [31, 107] for more information.

Additionally, Figure F.4 gives a graphical explanation of the two different approaches. Equation F.7 is solved with a given initial velocity, and the results are normalized. Due to the influence of the damping parameter ς, the displacement (indentation of the DEM impact) and the acceleration do not share a common zero-crossing of the abscissa. With respect to the two different declarations of contact end, given in Table F.4, two different velocity values $\dot{\delta_n}^f$ result.

Finally, the artifacts resulting from [108]'s contact end condition $\delta_n = 0$ can be observed in Figure F.4. If the contact is considered to be ended at the time of $\delta_n = 0$ the acceleration has already reached a negative value, resulting in non-physical attracting forces.

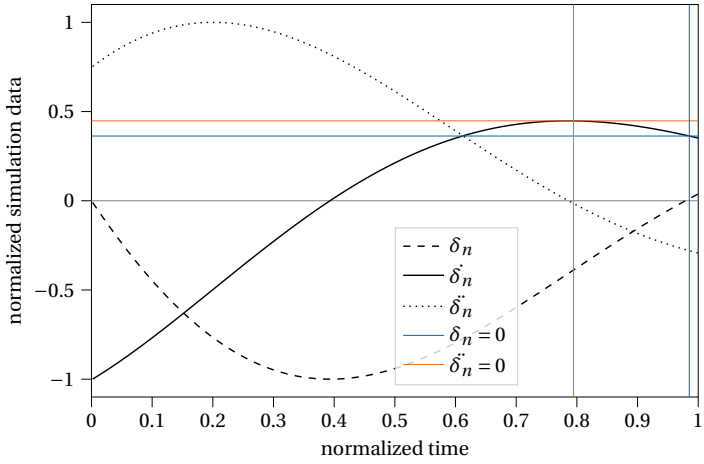

Figure F.4: Graphical explanation of the two different contact end conditions, given in Table F.4. The contents of this graph are the results of equation F.7 with a given initial velocity. Figure adapted from [31].

APPENDIX G

Energy Terms

The most important energy terms for DEM as well as for FEM are presented below. The damping energy is not conservative and must be integrated over time. All other energy terms can be re-evaluated independently at any time. The energy terms for elastic and inelastic deformations of the DEM particles depend on the contact law chosen in each case and are expressed here only by their dependencies. An explanation and discussion of the individual DEM symbols can be found in Appendix F.*

FEM

$$\Pi_{\mathrm{FEM,strain}} = \int_{\Omega_0} \int_{\mathbf{E}} \mathbf{S}(\mathbf{E})\ d\mathbf{E}\, d\Omega_0, \tag{G.1}$$

$$\Pi_{\mathrm{FEM,strain\,elastic}} = \int_{\Omega_0} \frac{1}{2}\mathbf{S}:\mathbf{E} + \mathbf{S}_0:\mathbf{E}\, d\Omega_0 = \sum^{n_{\mathrm{elements}}} \int_{\Omega_0} \left(\frac{1}{2}\tilde{\mathbf{S}} + \tilde{\mathbf{S}}_0\right)\cdot\tilde{\mathbf{E}}\, d\Omega_0, \tag{G.2}$$

$$\Pi_{\mathrm{FEM,kin}} = \frac{1}{2}\int_{\Omega_0} \rho_0 \dot{\mathbf{u}}\cdot\dot{\mathbf{u}}\, d\Omega_0 = \frac{1}{2}\sum^{n_{\mathrm{elements}}} \hat{\dot{\mathbf{u}}}\cdot\mathbf{M}\hat{\dot{\mathbf{u}}}, \tag{G.3}$$

$$\Pi_{\mathrm{FEM,damp}}(t) = \int_0^t \sum^{n_{\mathrm{elements}}} \hat{\dot{\mathbf{u}}}\cdot\mathbf{D}\hat{\dot{\mathbf{u}}}\, dt, \tag{G.4}$$

$$\Pi_{\mathrm{FEM,ext}} = \sum^{n_{\mathrm{elements}}} \left(\hat{\mathbf{B}} + \hat{\mathbf{F}}_{\mathrm{ext}}\right)\cdot\hat{\mathbf{u}}, \tag{G.5}$$

$$\Pi_{\mathrm{FEM,ext,c}} = \sum^{n_{\mathrm{elements}}} \hat{\mathbf{F}}_C\cdot\hat{\mathbf{u}}, \tag{G.6}$$

$$\begin{aligned}\Pi_{\mathrm{FEM,total}} &= \Pi_{\mathrm{FEM,strain}} + \Pi_{\mathrm{FEM,kin}} + \Pi_{\mathrm{FEM,damp}} \\ &\quad - \left(\Pi_{\mathrm{FEM,ext}} + \Pi_{\mathrm{FEM,ext,c}}\right).\end{aligned} \tag{G.7}$$

* Neglecting rotational kinetic energy.

DEM

$$\Pi_{\text{DEM,pot}} = \sum^{n_{\text{particles}}} m\mathbf{g} \cdot \left(\hat{\mathbf{X}}_{\text{ref}} - \hat{\mathbf{x}}\right), \tag{G.8}$$

$$\Pi_{\text{DEM,kin}} = \frac{1}{2} \sum^{n_{\text{particles}}} m\hat{\dot{\mathbf{u}}} \cdot \hat{\dot{\mathbf{u}}}, \tag{G.9}$$

$$\Pi_{\text{DEM,ela}} = \Pi_{\text{DEM,ela}}\left(F_n, F_t, \delta_n, \Delta s\right), \tag{G.10}$$

$$\Pi_{\text{DEM,damp}}(t) = \Pi_{\text{DEM,damp}}\left(t, c_n, c_t, \dot{\delta_n}, \| \dot{\mathbf{u}}_{c,t}^{ij} \|\right), \tag{G.11}$$

$$\Pi_{\text{DEM,total}} = \Pi_{\text{DEM,pot}} + \Pi_{\text{DEM,kin}} + \Pi_{\text{DEM,ela}} + \Pi_{\text{DEM,damp}}. \tag{G.12}$$

For the calculation of the DEM gravitational potential energy a reference point $\hat{\mathbf{X}}_{\text{ref}}$ needs to be chosen. It is advisable to place $\hat{\mathbf{X}}_{\text{ref}}$ on position of the undeformed geometry of the structure.

Total System

$$\begin{aligned}\Pi_{\text{total}} =& \Pi_{\text{FEM,strain}} + \Pi_{\text{FEM,kin}} + \Pi_{\text{FEM,damp}} \\ &+ \Pi_{\text{DEM,pot}} + \Pi_{\text{DEM,kin}} + \Pi_{\text{DEM,ela}} + \Pi_{\text{DEM,damp}} - \Pi_{\text{FEM,ext}}.\end{aligned} \tag{G.13}$$

APPENDIX **H**

Pre-Stress Application

Repeatedly pre-stresses are mentioned and taken into account in FEM simulations. However, the correct consideration of pre-stressing is not straightforward and usually depends on the practical implementation in the construction process. Therefore, the topic will be discussed based on an one-dimensional example, where the pre-stressing of a cable between 2 points without dead weight sag is analyzed.

Two questions, in particular, are worth discussing.

1. **To which initial length does the applied pre-stress refer?**

   Two methods are available for applying pre-stresses.

   - In Figure H.1a, the cable is placed between the two supports. While the cable is not yet fixed to the right support, the pre-stress is applied, and finally, the cable is attached to the right support.

     In this case, the reference length is the planned length between the supports L.
   - In Figure H.1b, the cable is too short and then lengthened before being attached to the right support. The initial shortening must be calculated so that the elastic deformation Δx causes the planned pre-stressing.

     In this case, the reference length is the length of the short cable l.

   The decision, therefore, results in the appropriate choice of the reference length. In the present work, the case shown in Figure H.1a is chosen. Thus, the pre-stress can be added to the stress from deformations integrated over the reference length, i.e., the planned distance of the supports L^*.

* See equation 3.25.

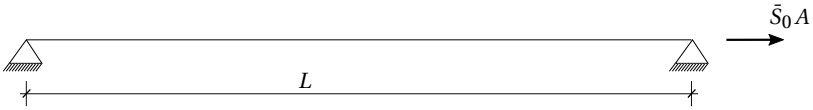

(a) Reference length: L.

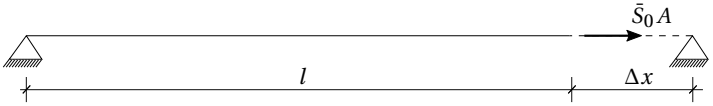

(b) Reference length: l.

Figure H.1: Considerations on the application of pre-stress and its numerical implementation.

2. Which stress measure is used?

While the Second Piola-Kirchhoff stress refers to the reference geometry, the Cauchy stress considers the actual geometry. In practice, the appropriate pre-stress value is obtained by continuous stressing. Thus, the final stress state is related to the actual geometry. Although this would justify the choice of the Cauchy stress tensor, this dissertation works with the Second Piola-Kirchhoff stress measure for the following reasons:

- No consideration of the change of the cross-section due to longitudinal stresses.
- As discussed in **1.**, the planned length between the nodes is used as the reference length for integrating the stress.

Bibliography

[1] A. C. Aitken. XXV.—On Bernoulli's Numerical Solution of Algebraic Equations. In *Proceedings of the Royal Society of Edinburgh*, 1927. DOI: https://doi.org/10.1017/S0370164600022070.

[2] A. Alipour and F. Zareian. Study Rayleigh Damping In Structures: Uncertainties And Treatments [sic]. In *The 14th World Conference on Earthquake Engineering, Beijing, China*, 2008.

[3] B. Arndt, T. Ortiz, and K. Turner. Colorado's Full-Scale Field Testing of Rockfall Attenuator Systems. *Transportation Research Circular E-C141, Transportation Research Board*, 2009. ISSN: 0097-8515.

[4] A. Ashtekar and F. Sadeghi. A New Approach for Including Cage Flexibility in Dynamic Bearing Models by Using Combined Explicit Finite and Discrete Element Methods. *Journal of Tribology*, 2012. DOI: https://doi.org/10.1115/1.4007348.

[5] P. Asteriou, H. Saroglou, and G. Tsiambaos. Scaling Factors for the Coefficient of Restitution. In *ISRM International Symposium - EUROCK 2013*, 2013. ISBN: 978-1-138-00080-3.

[6] Y. Başar and D. Weichert. *Nonlinear Continuum Mechanics of Solids - Fundamental Mathematical and Physical Concepts*. Springer Nature Switzerland AG, 2000. ISBN: 978-3-662-04299-1.

[7] J.-M. Battini. *Co-Rotational Beam Elements In Instability Problems*. PhD thesis, Royal Institute of Technology - Department of Mechanics, Stockholm, Sweden, 2002.

[8] T. Belytschko, W. K. Liu, B. Moran, and K. Elkhodary. *Nonlinear Finite Elements for Continua and Structures*. John Wiley & Sons, Inc., 2nd edition, 2014. ISBN: 978-1-118-63270-3.

[9] D. Bertrand, F. Nicot, P. Gotteland, and S. Lambert. Discrete Element Method (DEM) Numerical Modeling of Double-Twisted Hexagonal Mesh. *Canadian Geotechnical Journal*, 2008. DOI: https://doi.org/10.1139/T08-036.

[10] D. Bertrand, A. Trad, A. Limam, and C. Silvani. Full-Scale Dynamic Analysis of an Innovative Rockfall Fence Under Impact Using the Discrete Element Method: From the Local Scale to the Structure Scale. *Rock Mechanics and Rock Engineering*, 2012. DOI: https://doi.org/10.1007/s00603-012-0222-5.

[11] B. Bhuvaraghan, S. M. Srinivasan, B. Maffeo, R. D. McCLain, Y. Potdar, and O. Prakash. Shot Peening Simulation Using Discrete and Finite Element Methods. *Advances in Engineering Software*, 2010. DOI: https://doi.org/10.1016/j.advengsoft.2010.09.003.

[12] W. Blum. *Eine kurze Geschichte der Mathematik. (German)*. wbg Theiss, 2019. ISBN: 978-3-8062-3877-8.

[13] R. Boulaud and C. Douth. A Sliding Cable Model for Rockfall Barrier Simulations Using Dynamic Relaxation. In *IASS Annual Symposium*, 2017. ISSN 2518-6582 (Online).

[14] F. Bourrier, F. Kneib, B. Chareyre, and T. Fourcaud. Discrete Modeling of Granular Soils Reinforcement by Plant Roots. *Ecological Engineering*, 2013. DOI: http://dx.doi.org/10.1016/j.ecoleng.2013.05.002.

[15] C. Bovet and L. Zamponi. An Approach for Predicting the Internal Behaviour of Ball Bearings Under High Moment Load. *Mechanism and Machine Theory*, 2016. URL: https://hal.archives-ouvertes.fr/hal-01154703/document.

[16] G. Bradshaw. Sphere-Tree Construction Toolkit. http://isg.cs.tcd.ie/spheretree/, 2021.

[17] G. Bradshaw and C. O'Sullivan. Adaptive Medial-Axis Approximation for Sphere-Tree Construction. *ACM Transactions on Graphics*, 2004. DOI: https://doi.org/10.1145/966131.966132.

[18] G. Bradshaw and C. O'Sullivan. Sphere-Tree Construction using Dynamic Medial Axis Approximation. In *Proceedings of the 2002 ACM SIGGRAPH/Eurographics symposium on Computer animation*, 2002. DOI: https://doi.org/10.1145/545261.545267.

[19] P. Bucher, A. Ghantasala, P. Dadvand, R. Wüchner, and K. Bletzinger. Realizing CoSimulation in and With a Multiphysics Framework. In *9th edition of the International Conference on Computational Methods for Coupled Problems in Science and Engineering (COUPLED PROBLEMS 2021)*, 2021. URL: https://www.scipedia.com/public/Bucher_et_al_2021a.

[20] O. Buzzi, E. Leonarduzzi, B. Krummenacher, A. Volkwein, and A. Giacomini. Performance of High Strength Rock Fall Meshes: Effect of Block Size and Mesh Geometry. *Rock Mechanics and Rock Engineering*, 2015. DOI: https://doi.org/10.1007/s00603-014-0640-7.

[21] L. Cao, F. Sadeghi, and L.-E. Stacke. A Combined EFEM–Discrete Element Method Dynamic Model of Rotor–Bearing–Housing System. *Journal of Tribology*, 2017. DOI: https://doi.org/10.1115/1.4036378.

[22] G. Casas, D. Mukherjee, M. Á. Celigueta, T. I. Zohdi, and E. Oñate. A Modular, Partitioned, Discrete Element Framework for Industrial Grain Distribution Systems With Rotating Machinery. *Computational Particle Mechanics*, 2017. DOI: https://doi.org/10.1007/s40571-015-0089-9.

[23] M.L. Cerquaglia, D. Thomas, R. Boman, V. Terrapon, and J.-P. Ponthot. A Fully Partitioned Lagrangian Framework for FSI Problems Characterized by Free Surfaces, Large Solid Deformations and Displacements, and Strong Added-Mass Effects. *Computer Methods in Applied Mechanics and Engineering*, 2019. DOI: https://doi.org/10.1016/j.cma.2019.01.021.

[24] K.T. Chau, R.H.C. Wong, and J.J. Wu. Coefficient of Restitution and Rotational Motions of Rockfall Impacts. *International Journal of Rock Mechanics and Mining Sciences*, 2002. DOI: https://doi.org/10.1016/S1365-1609(02)00016-3.

[25] A. K. Chopra. *Dynamics of Structures*. Pearson, 2000. ISBN: 978-0-130-86973-9.

[26] J. Chung and G. M. Hulbert. A Time Integration Algorithm for Structural Dynamics With Improved Numerical Dissipation: The Generalized-α Method. *Journal of Applied Mechanics*, 1993. DOI: https://doi.org/10.1115/1.2900803.

[27] C. J. Coetzee and D. N. J. Els. Calibration of Granular Material Parameters for DEM Modelling and Numerical Verification by Blade–Granular Material Interaction. *Journal of Terramechanics*, 2009. DOI: https://doi.org/10.1016/j.jterra.2008.12.004.

[28] A. Cornejo. *A Fully Lagrangian Formulation for Fluid-Structure Interaction Between Free- Surface Flows and Multi-Fracturing Solids*. PhD thesis, UPC, Departament d'Enginyeria Civil i Ambiental, Barcelona, Spain, 2020.

[29] A. Cornejo, A. Franci, F. Zárate, and E. Oñate. A Fully Lagrangian Formulation for Fluid-Structure Interaction Problems With Free-Surface Flows and Fracturing Solids. *Computers & Structures*, 2021. DOI: https://doi.org/10.1016/j.compstruc.2021.106532.

[30] J. B. Coulibaly, M.-A. Chanut, S. Lambert, and F. Nicot. Toward a Generic Computational Approach for Flexible Rockfall Barrier Modeling. *Rock Mechanics and Rock Engineering*, 2019. DOI: https://doi.org/10.1007/s00603-019-01878-6.

[31] S. Cummins, C. Thornton, and P. Cleary. Contact Force Models in Inelastic Collisions. In *Ninth International Conference on CFD in the Minerals and Process Industries*, 2012. ISBN: 978-1-922173-01-0.

[32] P. A. Cundall and O.D.L. Strack. A Discrete Numerical Model for Granular Assemblies. *Geotechnique*, 1979. DOI: https://doi.org/10.1680/geot.1979.29.1.47.

[33] P. Dadvand, R. Rossi, M. Gil, X. Martorell, J. Cotela, E. Juanpere, S. Idelsohn, and E. Oñate. Migration of a Generic Multi-Physics Framework to HPC Environments. *Computers & Fluids*:301–309, 2013. DOI: https://doi.org/10.1016/j.compfluid.2012.02.004.

[34] P. Dadvand, R. Rossi, and E. Oñate. An Object-oriented Environment for Developing Finite Element Codes for Multi-disciplinary Applications. *Archives of Computational Methods in Engineering*:253–297, 2010. DOI: https://doi.org/10.1007/s11831-010-9045-2.

[35] J. Denape. Third Body Concept and Wear Particle Behavior in Dry Friction Sliding Conditions. *Key Engineering Materials*, 2015. DOI: https://doi.org/10.4028/www.scientific.net/KEM.640.1.

[36] E. A. de Souza Neto, D. Perić, and D. R. J. Owen. *Computational Methods for Plasticity: Theory and Applications*. John Wiley & Sons, Inc., 2008. ISBN: 978-0-470-69452-7.

[37] S. Dhakal, N. P. Bhandary, R. Yatabe, and N. Kinoshita. Experimental, Numerical And Analytical Modelling Of A Newly Developed Rockfall Protective Cable-net Structure. *Natural Hazards and Earth System Sciences*, 2011. DOI: https://doi.org/10.5194/nhess-11-3197-2011.

[38] T. Drieseberg. *Ein Beitrag zur Formfindung von Tensegrity-Systemen mit der Kraftdichtemethode. (German)*. PhD thesis, University of Kassel, 2007. ISBN: 978-3-89958-305-2.

[39] L. Dugelas, F. Bourrier, I. Olmedo, P. Robit, and F. Nicot. DEM Modelling of the ELITE Rockfall Flexible Barrier: A New Net Model Introducing Sliding. In *Symposium Rock Slope Stability*, 2021. URL: https://rss2021.sciencesconf.org/data/pages/RSS2021_proceedings.pdf.

[40] L. Dugelas, J. B. Coulibaly, F. Bourrier, S. Lambert, M.-A. Chanut, I. Olmedo, and F. Nicot. Assessment of the Predictive Capabilities of Discrete Element Models for Flexible Rockfall Barriers. *International Journal of Impact Engineering*, 2019. DOI: https://doi.org/10.1016/j.ijimpeng.2019.103365.

[41] A. P. Dykes. Landslide Investigations During Pandemic Restrictions: Initial Assessment of Recent Peat Landslides in Ireland. *Landslides*, 2022. DOI: https://doi.org/10.1007/s10346-021-01797-0.

[42] A. Effeindzourou, K. Thoeni, and A. Giacomini C. Wendeler. Efficient Discrete Modelling of Composite Structures for Rockfall Protection. *Computers and Geotechnics*, 2017. DOI: http://dx.doi.org/10.1016/j.compgeo.2017.02.005.

[43] J.P. Escallón, A. von Boetticher, C. Wendeler, E. Chatzi, and P. Bartelt. Mechanics of Chain-Link Wire Nets With Loose Connections. *Engineering Structures*, 2015. DOI: https://doi.org/10.1016/j.engstruct.2015.07.005.

[44] C. Farhat, K. G. van der Zee, and P. Geuzaine. Provably Second-Order Time-Accurate Loosely-Coupled Solution Algorithms for Transient Nonlinear Computational Aeroelasticity. *Computer Methods in Applied Mechanics and Engineering*, 2006. DOI: https://doi.org/10.1016/j.cma.2004.11.031.

[45] C. A. Felippa, K.-C. Park, and C. Farhat. Partitioned Analysis of Coupled Mechanical Systems. *Computer Methods in Applied Mechanics and Engineering*, 2001. DOI: https://doi.org/10.1016/S0045-7825(00)00391-1.

[46] J. Fern, A. Rohe, K. Soga, and E. Alonso. *The Material Point Method for Geotechnical Engineering. A Practical Guide*. CRC Press, 1st edition, 2019. ISBN: 978-0-367-73194-6.

[47] V. Mataix Ferrándiz, P. Bucher, R. Rossi, J. Cotela, J.M. Carbonell, R. Zorrilla, and R. Tosi. KratosMultiphysics (Version 8.0). *Zenodo*, 2020. DOI: https://doi.org/10.5281/zenodo.3234644.

[48] C. E. Flores Flores. *Fluid-Structure-Interaction by Coupling FEM and PFEM in an Open-Source Multi-Physics Code*. Master's thesis, Technical University of Munich, 2021. (Unpublished).

[49] Geobrugg. DELTAX®. https://www.geobrugg.com/de/DELTAX-7806,7859.html, 2021.

[50] Geobrugg. SPIDER®. https://www.geobrugg.com/de/SPIDER-System-8140,7859.html, 2020.

[51] 8590 Romanshorn Geobrugg AG. System manual, Att-80, Attenuator System, 2019.

[52] J. Glover and W. Ammann. Geobrugg Internal Testing Report No. 1-A, Rockfall Attenuator Testing Nicolum Quarry, Hope BC. In *Global Risk Forum Davos, GRF, Switzerland*, 2016.

[53] J. M. González, F. Salazar, and E. Oñate. Evaluation of the Performance of Ballasted Railway Structures Subjected to High-Speed Train Loads by the Discrete Element Method. In *Conference: VI International Conference on Particle based Methods. Fundamentals and Applications (Particles 2019)*, 2019.

[54] J. M. González, F. Salazar, and E. Oñate. Full-Scale Numerical Calculation of Ballasted Tracks With the Discrete Element Method. In *Conference: DEM8 – 8th International Conference on Discrete Element Methods*, 2019.

[55] F. Gracia, P. Villard, and V. Richefeu. Comparison of Two Numerical Approaches (DEM and MPM) Applied to Unsteady Flow. *Computational Particle Mechanics*, 2019. DOI: https://doi.org/10.1007/s40571-019-00236-1.

[56] H. G. Grassl. *Experimentelle und numerische Modellierung des dynamischen Trag- und Verformungsverhaltens von hochflexiblen Schutzsystemen gegen Steinschlag. (German)*. PhD thesis, Swiss Federal Institute of Technology in Zurich, 2002. DOI: https://doi.org/10.3929/ethz-a-004446317.

[57] H. Haddad, M. Guessasma, and J. Fortin. A DEM–FEM Coupling Based Approach Simulating Thermomechanical Behaviour of Frictional Bodies With Interface Layer. *International Journal of Solids and Structures*, 2016. DOI: https://doi.org/10.1016/j.ijsolstr.2015.11.026.

[58] J. P. Hambleton, O. Buzzi, A. Giacomini, M. Spadari, and S. W. Sloan. Perforation of Flexible Rockfall Barriers by Normal Block Impact. *Rock Mechanics and Rock Engineering*, 2013. DOI: https://doi.org/10.1007/s00603-012-0343-x.

[59] W. R. Hamilton. On Quaternions, or on a New System of Imaginaries in Algebra. *The London Edinburgh and Dublin Philosophical Magazine*, 1844. Edited by D. R. Wilkins in 2000. https://www.emis.de/classics/Hamilton/OnQuat.pdf.

[60] H. Hofmann, J. Glover, and D. Wyllie. Development of a Dimensioning Concept for the Flexible Rockfall Protection Solution Attenuator. In *International Congress on Rock Mechanics and Rock Engineering, Foz do Iguassu, Brazil*, 2019. ISBN: 978-0-367422-85-1.

[61] G. A. Holzapfel. *Nonlinear Solid Mechanics - A Continuum Approach for Engineering*. John Wiley & Sons Ltd, 2000. ISBN: 978-0-471-82319-3.

[62] T. J. R. Hughes. *The Finite Element Method - Linear Static and Dynamic Finite Element Analysis*. Courier Corporation, 2nd edition, 2012. ISBN: 978-0-486-13502-1.

[63] J. Irazábal, F. Salazar, M. Santasusana, and E. Oñate. Effect of the Integration Scheme on the Rotation of Non-Spherical Particles With the Discrete Element Method. *Computational Particle Mechanics*, 2019. DOI: https://doi.org/10.1007/s40571-019-00232-5.

[64] S. Jain, R. Khosa, and A. K. Gosain. Impact of Landslide Size and Settings on Landslide Scaling Relationship: A Study From the Himalayan Regions of India. *Landslides*, 2022. DOI: https://doi.org/10.1007/s10346-021-01794-3.

[65] A. S. Ramos Jr. and G. H. Paulino. Convex Topology Optimization For Hyperelastic Trusses Based On The Ground-Structure Approach. *Structural and Multidisciplinary Optimization*, 2014. DOI: https://doi.org/10.1007/s00158-014-1147-2.

[66] J. Kiendl. *Isogeometric Analysis and Shape Optimal Design of Shell Structures*. PhD thesis, Technical University of Munich, 2011. ISBN: 978-3-8440-0104-4.

[67] W. Kim. An Accurate Two-stage Explicit Time Integration Scheme For Structural Dynamics And Various Dynamic Problems. *International Journal for Numerical Methods in Engineering*, 2019. DOI: https://doi.org/10.1002/nme.6098.

[68] M. Kodam, R. Bharadwaj, J. Curtis, B. Hancock, and C. Wassgren. Force Model Considerations For Glued-Sphere Discrete Element Method Simulations. *Chemical Engineering Science*, 2009. DOI: https://doi.org/10.1016/j.ces.2009.04.025.

[69] K. A. Kounoudji, M. Renouf, G. Mollon, and Y. Berthier. Role of Third Body on Bolted Joints' Self-Loosening. *Tribology Letters*, 2016. DOI: https://doi.org/10.1007/s11249-016-0640-8.

[70] J. Kozicki and F. V. Donzé. YADE-OPEN DEM: An Open-Source Software Using a Discrete Element Method to Simulate Granular Material. *Engineering Computations*, 2009. DOI: http://dx.doi.org/10.1108/02644400910985170.

[71] S. Krenk. *Non-linear Modeling and Analysis of Solids and Structures*. Cambridge University Press, 2012. ISBN: 978-0-511-81216-3.

[72] D. Kuhlman. *A Python Book: Beginning Python, Advanced Python, and Python Exercises*. Platypus Global Media, 2011. ISBN: 978-0-9842-2123-3. URL: https://books.google.de/books?id=1FL-ygAACAAJ.

[73] U. Küttler. *Effiziente Lösungsverfahren für Fluid-Struktur-Interaktions-Probleme. (German)*. PhD thesis, Technical University of Munich, 2009.

[74] U. Küttler and W. Wall. Fixed-Point Fluid-Structure Interaction Solvers With Dynamic Relaxation. *Computational Mechanics*, 2008. DOI: https://doi.org/10.1007/s00466-008-0255-5.

[75] F. Leonhardt and J. Schlaich. Weitgespannte Flächentragwerke. (German). *Sonderforschungsbericht 64, Universität Stuttgart*, 1973.

[76] X. Li, B. Sovilla, C. Jiang, and J. Gaume. The Mechanical Origin of Snow Avalanche Dynamics and Flow Regime Transition. *The Cryosphere*, 2020. DOI: https://doi.org/10.5194/tc-14-3381-2020.

[77] X. Li, B. Sovilla, C. Jiang, and J. Gaume. Three-Dimensional and Real-Scale Modeling of Flow Regimes in Dense Snow Avalanches. *Landslides*, 2021. DOI: https://doi.org/10.1007/s10346-021-01692-8.

[78] S. Liu, H. Li, S. Shen, and S. Wu. Simulation of Particle Rebounding From the Slider Air Bearing Surface. *Microsystem Technologies*, 2016. DOI: https://doi.org/10.1007/s00542-016-2847-x.

[79] L. B. Lucy. A Numerical Approach to the Testing of the Fission Hypothesis. *The Astronomical Journal*, 1977.

[80] H.-G. Matuttis and J. Chen. *Understanding the Discrete Element Method: Simulation of Non-Spherical Particles for Granular and Multi-Body Systems*. John Wiley & Sons, Inc., 2014. ISBN: 978-1-118-56720-3.

[81] S. Meduri, M. Cremonesi, U. Perego, O. Bettinotti, A. Kurkchubasche, and V. Oancea. A Partitioned Fully Explicit Lagrangian Finite Element Method for Highly Nonlinear Fluid-Structure Interaction Problems. *International Journal for Numerical Methods in Engineering*, 2018. DOI: https://doi.org/10.1002/nme.5602.

[82] J. Meijaard. Lateral Impacts on Flexible Beams in Multibody Dynamics Simulations. In *IUTAM Symposium on Multiscale Problems in Multibody System Contacts*, 2006. ISBN: 978-1-4020-5981-0.

[83] A. Mentani, L. Govoni, A. Giacomini, G. Gottardi, and O. Buzzi. An Equivalent Continuum Approach to Efficiently Model the Response of Steel Wire Meshes to Rockfall Impacts. *Rock Mechanics and Rock Engineering*, 2018. DOI: https://doi.org/10.1007/s00603-018-1490-5.

[84] A. Munjiza, J. P. Latham, and N. W. M. John. 3D Dynamics of Discrete Element Systems Comprising Irregular Discrete Elements — Integration Solution for Finite Rotations in 3D. *International Journal for Numerical Methods in Engineering*, 2002. DOI: https://doi.org/10.1002/nme.552.

[85] K. Murugaratnam, S. Utili, and N. Petrinic. A Combined DEM–FEM Numerical Method for Shot Peening Parameter Optimisation. *Advances in Engineering Software*, 2015. DOI: https://doi.org/10.1016/j.advengsoft.2014.09.001.

[86] K. Nakashino and M. C. Natori. Efficient Modification Scheme of Stress-Strain Tensor for Wrinkled Membranes. *American Institute of Aeronautics and Astronautics Journal*, 2012. DOI: https://doi.org/10.2514/1.7143.

[87] K. Nakashino, A. Nordmark, and A. Eriksson. Geometrically Nonlinear Isogeometric Analysis of a Partly Wrinkled Membrane Structure. *Computers & Structures*, 2020. DOI: https://doi.org/10.1016/j.compstruc.2020.106302.

[88] A. G. Neto and P. Wriggers. Discrete Element Model for General Polyhedra. *Computational Particle Mechanics*, 2021. DOI: https://doi.org/10.1007/s40571-021-00415-z.

[89] N. T. Ngo, B. Indraratna, and C. Rujikiatkamjorn. Coupled DEM-FEM Analysis for Simulating Ballasted Rail Tracks. *Faculty of Engineering and Information Sciences - Papers: Part B*, 2017. URL: https://ro.uow.edu.au/eispapers1/1515.

[90] F. Nicot, B. Cambou, and G. Mazzoleni. Design of Rockfall Restraining Nets from a Discrete Element Modelling. *Rock Mechanics and Rock Engineering*, 2001. DOI: https://doi.org/10.1007/s006030170017.

[91] F. Nicot, B. Cambou, and G. Mazzoleni. From a Constitutive Modelling of Metallic Rings to the Design of Rockfall Restraining Nets. *Numerical and Analytical Methods in Geomechanics*, 2000. DOI: https://doi.org/10.1002/1096-9853(200101)25:1%3C49::AID-NAG117%3E3.0.CO;2-N.

[92] R. W. Ogden. Non-Linear Elastic Deformations. *Journal of Applied Mathematics and Mechanics*, 1985. DOI: https://doi.org/10.1002/zamm.19850650903.

[93] E. Oñate, S. R. Idelsohn, F. Del Pin, and R. Aubry. The Particle Finite Element Method. An Overview. *International Journal of Computational Methods*, 1(02):267–307, 2004. DOI: https://doi.org/10.1142/S0219876204000204.

[94] E. Oñate, F. Zárate, M. A. Celigueta, J. M. González, J. Miquel, J. M. Carbonell, F. Arrufat, and S. Latorre and M. Santasusana. *Advances in the DEM and Coupled DEM and FEM Techniques in Non Linear Solid Mechanics*. In *Advances in Computational Plasticity: A Book in Honour of D. Roger J. Owen*. Springer International Publishing, Cham, 2018, pages 309–335. ISBN: 978-3-319-60885-3.

[95] A. Rafiee, P. Plotto, and M. Khatib. Numerical Modelling of Full-Scale Rockfall Protection Structures Under Dynamic Impact Using Discrete Element Method. In *Symposium Rock Slope Stability*, 2021. URL: https://rss2021.sciencesconf.org/data/pages/RSS2021_proceedings.pdf.

[96] P. B. Ryzhakov, R. Rossi, S. R. Idelsohn, and E. Oñate. A Monolithic Lagrangian Approach for Fluid–Structure Interaction Problems. *Computational Mechanics*, 2010. DOI: https://doi.org/10.1007/s00466-010-0522-0.

[97] N. Sabatakakis, N. Depountis, and N. Vagenas. Evaluation of Rockfall Restitution Coefficients, 2015. DOI: https://doi.org/10.1007/978-3-319-09057-3_359.

[98] M. Santasusana. *Numerical Techniques for Non-Linear Analysis of Structures Combining Discrete Element and Finite Element Methods*. PhD thesis, Centre for Numerical Methods in Engineering, Barcelona, Spain, 2016. https://www.cimne.com/cvdata/cntr2/dtos/pgs/Research/Theses/Miquel-Santasusana.pdf.

[99] M. Santasusana, J. Irazábal, E. Oñate, and J. M. Carbonell. The Double Hierarchy Method. a Parallel 3D Contact Method for the Interaction of Spherical Particles With Rigid FE Boundaries Using the DEM. *Computational Particle Mechanics*, 2016. DOI: https://doi.org/10.1007/s40571-016-0109-4.

[100] N. Sasiharan, B. Muhunthan, T.C. Badger, S. Shu, and D.M.Carradine. Numerical Analysis Of The Performance Of Wire Mesh And Cable Net Rockfall Protection Systems. *Engineering Geology*, 2006. DOI: https://doi.org/10.1016/j.enggeo.2006.09.005.

[101] K. B. Sautter, H. Hofmann, C. Wendeler, M.Á. Celigueta, P. Bucher, K.-U. Bletzinger, and R. Wüchner. Coupling the Discrete Element Method With the Finite Element Method to Simulate Rockfall Impact Experiments. In *International Conference on Computational Methods for Coupled Problems in Science and Engineering*, 2021. DOI: http://dx.doi.org/10.23967/coupled.2021.016.

[102] K. B. Sautter, H. Hofmann, C. Wendeler, M.Á. Celigueta, P. Bucher, K.-U. Bletzinger, and R. Wüchner. Finite Element Models to Simulate Lightweight Rockfall Protection Structures. In *International Conference on Textile Composites and Inflatable Structures*, 2021. DOI: https://doi.org/http://dx.doi.org/10.23967/membranes.2021.001.

[103] K. B. Sautter, H. Hofmann, C. Wendeler, P. Wilson, P. Bucher, K.-U. Bletzinger, and R. Wüchner. Advanced Modeling and Simulation of Rockfall Attenuator Barriers Via Partitioned DEM-FEM Coupling. *Frontiers in Built Environment - Computational Methods in Structural Engineering*, 2021. DOI: https://doi.org/10.3389/fbuil.2021.659382.

[104] K. B. Sautter, H. Hofmann, C. Wendeler, R. Wüchner, and K.-U. Bletzinger. Influence of DE-Cluster Refinement on Numerical Analysis of Rockfall Experiments. *Computational Particle Mechanics*, 2021. DOI: https://doi.org/10.1007/s40571-020-00382-x.

[105] K. B. Sautter, M. Meßmer, T. Teschemacher, and K.-U. Bletzinger. Limitations of the St. Venant–Kirchhoff Material Model in Large Strain Regimes. *International Journal of Non-Linear Mechanics*, 2022. DOI: https://doi.org/10.1016/j.ijnonlinmec.2022.104207.

[106] K. B. Sautter, T. Teschemacher, M.Á. Celigueta, P. Bucher, K.-U. Bletzinger, and R. Wüchner. Partitioned Strong Coupling of Discrete Elements with Large Deformation Structural Finite Elements to Model Impact on Highly Flexible Tension Structures. *Advances in Civil Engineering - Advancements in the Analysis and Design of Protective Structures against Extreme Loadings 2020*, 2020. DOI: https://doi.org/10.1155/2020/5135194.

[107] T. Schwager and T. Pöschel. Coefficient of Restitution and Linear-Dashpot Model Revisited. *Granular Matter*, 2007. DOI: https://doi.org/10.1007/s10035-007-0065-z.

[108] J. Shäfer, S. Dippel, and D. Wolf. Force Schemes in Simulations of Granular Materials. *Journal de Physique*, 1996. DOI: https://doi.org/10.1051/jp1:1996129.

[109] W. Shen, M. Berti, T. Li, A. Benini, and Z. Qiao. The Influence of Slope Gradient and Gully Channel on the Run-Out Behavior of Rockslide-Debris Flow: An Analysis on the Verghereto Landslide in Italy. *Landslides*, 2022. DOI: https://doi.org/10.1007/s10346-022-01848-0.

[110] S. A. Sicklinger. *Stabilized Co-Simulation of Coupled Problems Including Fields and Signals*. PhD thesis, Technical University of Munich, 2014. ISBN: 978-3-943683-28-8.

[111] V. Singer, K. B. Sautter, A. Larese, R. Wüchner, and K.-U. Bletzinger. A Partitioned Material Point Method and Discrete Element Method Coupling Scheme. *Advanced Modeling and Simulation in Engineering Sciences*, 2022. DOI: https://doi.org/10.1186/s40323-022-00229-5.

[112] B. Smeets, T. Odenthal, S. Vanmaercke, and H. Ramon. Polygon-Based Contact Description for Modeling Arbitrary Polyhedra in the Discrete Element Method. *Computer Methods in Applied Mechanics and Engineering*, 290:277–289, 2015. DOI: https://doi.org/10.1016/j.cma.2015.03.004.

[113] V. Šmilauer, B. Chareyre, J. Duriez, A. Eulitz, A. Gladky, N. Guo, C. Jakob, J. Kozicki, F. Kneib, C. Modenese, J. Stransky, and K. Thoeni. Using and Programming, in: Yade Documentation 2nd Edition. *The Yade Project*, 2015. DOI: https://doi.org/10.5281/zenodo.34043.

[114] R. Steinbuch. *Finite Elemente — Ein Einstieg. (German)*. Springer Berlin, 1998. ISBN: 978-3-540-63128-6.

[115] B. Stroustrup. *A History of C++: 1979–1991*. In *History of Programming Languages—II*. Association for Computing Machinery, New York, NY, USA, 1996, pages 699–769. ISBN: 0201895021. URL: https://doi.org/10.1145/234286.1057836.

[116] S. Tahmasbi, A. Giacomini, C.Wendeler, and O.Buzzi. Towards a Novel and Efficient Method to Determine the Failure Energy of Rockfall Chain-Link Meshes. *Computers and Geotechnics*, 2020. DOI: https://doi.org/10.1016/j.compgeo.2019.103299.

[117] S. Tahmasbi, A. Giacomini, C. Wendeler, and O. Buzzi. On the Computational Efficiency of the Hybrid Approach in Numerical Simulation of Rockall Flexible Chain-Link Mesh. *Rock Mechanics and Rock Engineering*, 2019. DOI: https://doi.org/10.1007/s00603-019-01795-8.

[118] J. Takabi and M. M. Khonsari. On the Dynamic Performance of Roller Bearings Operating Under Low Rotational Speeds With Consideration of Surface Roughness. *Tribology International*, 2015. DOI: https://doi.org/10.1016/j.triboint.2015.01.011.

[119] K. Thoeni, A. Giacomini, C. Lambert, S. W. Sloan, and J. P. Carter. A 3D Discrete Element Modelling Approach for Rockfall Analysis With Drapery Systems. *International Journal of Rock Mechanics and Mining Sciences*, 2014. DOI: https://doi.org/10.1016/j.ijrmms.2014.02.008.

[120] C. Thornton, S. J. Cummins, and P. W. Cleary. An Investigation of the Comparative Behaviour of Alternative Contact Force Models During Inelastic Collisions. *Powder Technology*, 2013. DOI: https://doi.org/10.1016/j.powtec.2012.08.012.

[121] W. Tianyang. *Development of Co-Simulation Environment and Mapping Algorithms*. PhD thesis, Technical University of Munich, 2016. ISBN: 978-3-943683-38-7.

[122] M. J. Turner, R. W. Clough, H. C. Martin, and L. J. Topp. Stiffness and Deflection Analysis of Complex Structures. *Journal of the Aeronautical Sciences*, 1956. DOI: https://doi.org/10.2514/8.3664.

[123] G. N. Vanderplaats. *Multidiscipline Design Optimization*. Vanderplaats Research & Development, Inc., 2007. ISBN: 0-944956-04-1.

[124] A. Volkwein. *Numerische Simulation von flexiblen Steinschlagschutzsystemen. (German)*. PhD thesis, Swiss Federal Institute of Technology in Zurich, 2004. DOI: https://doi.org/10.3929/ethz-a-004879843.

[125] A. von Bötticher. *Flexible Hangmurenbarrieren: Eine numerische Modellierung des Tragwerks, der Hangmure und der Fluid-Struktur-Interaktion. (German)*. PhD thesis, Technical University of Munich, 2012. ISBN: 978-3-8440-1616-1.

[126] F. Wang, Y.-H. Wu, H. Yang, Y. Tanida, and A. Kamei. Preliminary Investigation of the 20 August 2014 Debris Flows Triggered by a Severe Rainstorm in Hiroshima City, Japan. *Geoenvironmental Disasters*, 2015. DOI: https://doi.org/10.1186/s40677-015-0025-6.

[127] C. Wendeler. *Murgangrückhalt in Wildbächen - Grundlagen zu Planung und Berechnung von flexiblen Barrieren. (German)*. PhD thesis, Swiss Federal Institute of Technology in Zurich, 2008.

[128] C. Wendeler, K. B. Sautter, P. Bucher, K.-U. Bletzinger, and R. Wüchner. Modellierungsaspekte und gekoppelte DEM-FEM Simulationen zur Untersuchung hochflexibler Steinschlagschutznetze. (German). *Berichte der Fachtagung Baustatik - Baupraxis*, 14, 2020. DOI: http://dx.doi.org/10.18419/opus-10762.

[129] A. Winterstein. *Modeling and Simulation of Wind-Structure Interaction of Slender Civil Engineering Structures Including Vibration Mitigation Systems*. PhD thesis, Technical University of Munich, 2020. ISBN: 978-3-943683-61-5.

[130] A. Winterstein, C. Lerch, K.-U. Bletzinger, and R. Wüchner. Partitioned Simulation Strategies for Fluid–Structure–Control Interaction Problems by Gauss–Seidel Formulations. *Advanced Modeling and Simulation in Engineering Sciences*, 2018. DOI: https://doi.org/10.1186/s40323-018-0123-6.

[131] R. Wüchner. *Mechanik und Numerik der Formfindung und Fluid-Struktur-Interaktion von Membrantragwerken. (German)*. PhD thesis, Technical University of Munich, 2006. ISBN: 978-3-8322-6391-1.

[132] D. Wyllie, T. Shevlin, J. Glover, and A. Buechi. Attenuators for Controlling Rockfall: First Results of a State-of-the-Art Full-Scale Testing Program. In *69th Canadian Geotechnical Conference*, 2016.

[133] X. Yang, G. Zhang, Y. Yu, and Q. Yu. Factors Influencing the Coefficient of Restitution in Rockfall Impacts. *Natural Hazards Review*, 2020. DOI: https://doi.org/10.1061/(ASCE)NH.1527-6996.0000454.

[134] Z. X. Yu, Y. K. Qiao, L. Zhao, H. Xu, S. C. Zhao, and Y. P. Liu. A Simple Analytical Method for Evaluation of Flexible Rockfall Barrier Part 1: Working Mechanism and Analytical Solution. *Advanced Steel Construction*, 2018. DOI: http://dx.doi.org/10.18057/IJASC.2018.14.2.1.

[135] S. Zhang, F. Wang, and R. Li. First Insight Into the Catastrophic Atami Debris Flow Induced by a Rain Gush on 3 July 2021 in Shizuoka, Japan. *Landslides*, 2022. DOI: https://doi.org/10.1007/s10346-021-01788-1.

[136] X. Zhang, Z. Chen, and Y. Liu. *The Material Point Method: A Continuum-Based Particle Method for Extreme Loading Cases*. Academic Press, 1st edition, 2016. ISBN: 978-0-124-07855-0.

Bisherige Titel der Schriftenreihe

Band	Titel
1	Frank Koschnick, *Geometrische Lockingeffekte bei Finiten Elementen und ein allgemeines Konzept zu ihrer Vermeidung*, 2004.
2	Natalia Camprubi, *Design and Analysis in Shape Optimization of Shells*, 2004.
3	Bernhard Thomee, *Physikalisch nichtlineare Berechnung von Stahlfaserbetonkonstruktionen*, 2005.
4	Fernaß Daoud, *Formoptimierung von Freiformschalen - Mathematische Algorithmen und Filtertechniken*, 2005.
5	Manfred Bischoff, *Models and Finite Elements for Thin-walled Structures*, 2005.
6	Alexander Hörmann, *Ermittlung optimierter Stabwerkmodelle auf Basis des Kraftflusses als Anwendung plattformunabhängiger Prozesskopplung*, 2006.
7	Roland Wüchner, *Mechanik und Numerik der Formfindung und Fluid-Struktur-Interaktion von Membrantragwerken*, 2006.
8	Florian Jurecka, *Robust Design Optimization Based on Metamodeling Techniques*, 2007.
9	Johannes Linhard, *Numerisch-mechanische Betrachtung des Entwurfsprozesses von Membrantragwerken*, 2009.
10	Alexander Kupzok, *Modeling the Interaction of Wind and Membrane Structures by Numerical Simulation*, 2009.
11	Bin Yang, *Modified Particle Swarm Optimizers and their Application to Robust Design and Structural Optimization*, 2009.
12	Michael Fleischer, *Absicherung der virtuellen Prozesskette für Folgeoperationen in der Umformtechnik*, 2009.
13	Amphon Jrusjrungkiat, *Nonlinear Analysis of Pneumatic Membranes - From Subgrid to Interface*, 2009.
14	Alexander Michalski, *Simulation leichter Flächentragwerke in einer numerisch generierten atmosphärischen Grenzschicht*, 2010.
15	Matthias Firl, *Optimal Shape Design of Shell Structures*, 2010.
16	Thomas Gallinger, *Effiziente Algorithmen zur partitionierten Lösung stark gekoppelter Probleme der Fluid-Struktur-Wechselwirkung*, 2011.
17	Josef Kiendl, *Isogeometric Analysis and Shape Optimal Design of Shell Structures*, 2011.
18	Joseph Jordan, *Effiziente Simulation großer Mauerwerksstrukturen mit diskreten Rissmodellen*, 2011.

Band	Titel
19	Albrecht von Boetticher, *Flexible Hangmurenbarrieren: Eine numerische Modellierung des Tragwerks, der Hangmure und der Fluid-Struktur-Interaktion*, 2012.
20	Robert Schmidt, *Trimming, Mapping, and Optimization in Isogeometric Analysis of Shell Structures*, 2013.
21	Michael Fischer, *Finite Element Based Simulation, Design and Control of Piezoelectric and Lightweight Smart Structures*, 2013.
22	Falko Hartmut Dieringer, *Numerical Methods for the Design and Analysis for Tensile Structures*, 2014.
23	Rupert Fisch, *Code Verification of Partitioned FSI Environments for Lightweight Structures*, 2014.
24	Stefan Sicklinger, *Stabilized Co-Simulation of Coupled Problems Including Fields and Signals*, 2014.
25	Madjid Hojjat, *Node-based parametrization for shape optimal design*, 2015.
26	Ute Israel, *Optimierung in der Fluid-Struktur-Interaktion - Sensitivitätsanalyse für die Formoptimierung auf Grundlage des partitionierten Verfahrens*, 2015.
27	Electra Stavropoulou, *Sensitivity analysis and regularization for shape optimization of coupled problems*, 2015.
28	Daniel Markus, *Numerical and Experimental Modeling for Shape Optimization of Offshore Structures*, 2015.
29	Pablo Suárez, *Design Process for the Shape Optimization of Pressurized Bulkheads as Components of Aircraft Structures*, 2015.
30	Armin Widhammer, *Variation of Reference Strategy - Generation of Optimized Cutting Patterns for Textile Fabrics*, 2015.
31	Helmut Masching, *Parameter Free Optimization of Shape Adaptive Shell Structures*, 2016.
32	Hao Zhang, *A General Approach for Solving Inverse Problems in Geophysical Systems by Applying Finite Element Method and Metamodel Techniques*, 2016.
33	Tianyang Wang, *Development of Co-Simulation Environment and Mapping Algorithms*, 2016.
34	Michael Breitenberger, *CAD-integrated Design and Analysis of Shell Structures*, 2016.
35	Önay Can, *Functional Adaptation with Hyperkinematics using Natural Element Method: Application for Articular Cartilage*, 2016.
36	Benedikt Philipp, *Methodological Treatment of Non-linear Structural Behavior in the Design, Analysis and Verification of Lightweight Structures*, 2017.
37	Michael Sean Andre, *Aeroelastic Modeling and Simulation for the Assessment of Wind Effects on a Parabolic Trough Solar Collector*, 2018.

Band	Titel
38	Andreas Apostolatos, *Isogeometric Analysis of Thin-Walled Structures on Multipatch Surfaces in Fluid-Structure Interaction*, 2018.
39	Altuğ Emiroğlu, *Multiphysics Simulation and CAD Integrated Shape Optimization in Fluid-Structure Interaction*, 2019.
40	Mehran Saeedi, *Multi-Fidelity Aeroelastic Analysis of Flexible Membrane Wind Turbine Blades*, 2017.
41	Reza Najian Asl, *Shape optimization and sensitivity analysis of fluids, structures, and their interaction using Vertex Morphing parametrization*, 2019.
42	Ahmed Abodonya, *Verification Methodology for Computational Wind Engineering Prediction of Wind Loads on Structures*, 2020.
43	Anna Maria Bauer, *CAD-integrated Isogeometric Analysis and Design of Lightweight Structures*, 2020.
44	Andreas Winterstein, *Modeling and Simulation of Wind-Structure Interaction of Slender Civil Engineering Structures Including Vibration Mitigation Systems*, 2020.
45	Franz-Josef Ertl, *Vertex Morphing for Constrained Shape Optimization of Three-dimensional Solid Structures*, 2020.
46	Daniel Baumgärtner, *On the Grid-based Shape Optimization of Structures with Internal Flow and the Feedback of Shape Changes into a CAD Model*, 2020.
47	Mohamed Khalil, *Combining Physics-based models and machine learning for an Enhanced Structural Health Monitoring*, 2021.
48	Long Chen, *Gradient Descent Akin Method*, 2021.
49	Aditya Ghantasala, *Coupling Procedures for Fluid-Fluid and Fluid-Structure Interaction Problems Based on Domain Decomposition Methods*, 2021.
50	Ann-Kathrin Goldbach, *The CAD-Integrated Design Cycle for Structural Membranes*, 2021.
51	Iñigo Pablo López Canalejo, *A Finite-Element Transonic Potential Flow Solver with an Embedded Wake Approach for Aircraft Conceptual Design*, 2022.
52	Mayu Sakuma, *An Application of Multi-Fidelity Uncertainty Quantification for Computational Wind Engineering*, 2022.
53	Suneth Warnakulasuriya, *Development of Methods for Finite Element-Based Sensitivity Analysis and Goal-Directed Mesh Refinement Using the Adjoint Approach for Steady and Transient Flows*, 2022.